ONE-STEP RESIDUAL SHIFTING DIFFUSION FOR IMAGE SUPER-RESOLUTION VIA DISTILLATION

Daniil Selikhanovych*
Kandinsky Lab
Moscow, Russia

David Li*
Mohamed bin Zayed University of Artificial Intelligence, Abu Dhabi, United Arab Emirates

Aleksei Leonov*
Moscow Independent Research Institute of Artificial Intelligence;
AI Foundation and Algorithm Lab, Moscow, Russia

Nikita Gushchin*
Applied AI Institute; AXXX
Moscow, Russia

Sergei Kushneriuk
AI Foundation and Algorithm Lab
Moscow, Russia

Alexander Filippov & Iaroslav Koshelev
AI Foundation and Algorithm Lab
Moscow, Russia

Evgeny Burnaev & Alexander Korotin
Applied AI Institute; AXXX
Moscow, Russia

ABSTRACT

Diffusion-based super-resolution (SR) models have a high visual quality but suffer from high computational cost. Existing acceleration methods for diffusion SR either miss realistic perceptual details (e.g., SinSR) or hallucinate non-existent structures (e.g., OSEDiff). To overcome these issues, we present **RSD**, a new distillation method for ResShift. RSD trains a student model to produce images such that a new fake ResShift model trained on them matches the teacher model. RSD achieves single-step restoration and noticeably outperforms the teacher in various perceptual metrics, such as LPIPS, CLIPIQA, and MUSIQ. RSD outperforms SinSR, another ResShift distillation method, and matches the state-of-the-art diffusion SR distillation methods with limited computational costs in terms of perceptual quality. Compared to SR methods based on pre-trained text-to-image models, RSD produces competitive perceptual results and requires fewer parameters, GPU memory, and training cost. We provide results on various real-world and synthetic datasets, including RealSR, RealSet65, DRealSR, and DIV2K.

1 INTRODUCTION

Single image super-resolution (SR) (Irani & Peleg, 1991; Glasner et al., 2009; Dong et al., 2016) is an inverse imaging problem that reconstructs a high-resolution (HR) image from a degraded low-resolution (LR) observation. In real-world settings (e.g., digital single-lens reflex cameras (Ignatov et al., 2017; Cai et al., 2019; Wei et al., 2020)), degradations are usually *complex and unknown*, which defines the blind real-world image SR (Real-ISR) problem. The SR problem is highly ill-posed and many methods have been proposed in the literature to address it.

Recently, diffusion models (DMs) have emerged as a strong alternative to GAN-based SR methods (Wang et al., 2021; Zhang et al., 2021) due to their ability to model complex data distributions (Dhariwal & Nichol, 2021). However, early DMs for SR (Rombach et al., 2022) were computationally expensive and required dozens or hundreds for the number of function evaluations (NFE) of the denoiser, which limits their real-time deployment on consumer devices. Subsequent work focused on methods to accelerate these models while maintaining perceptual quality. Among them, ResShift (Yue et al., 2023) achieves perceptually better results compared to state-of-the-art (SOTA) models of other classes, including GANs and transformers (Liang et al., 2021) while using only 15 NFE.

*Equal contribution. Correspondence to selikhanovychdaniil@gmail.com.

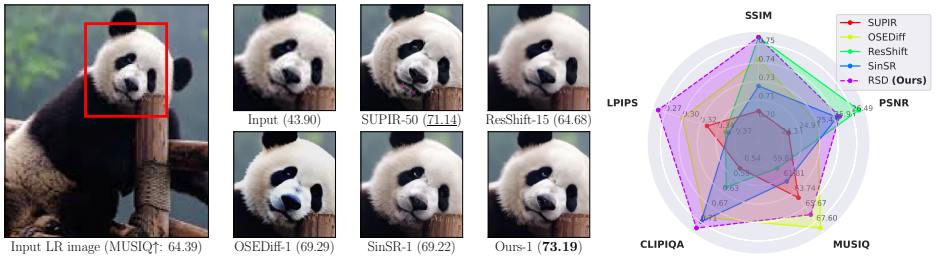

Figure 1: **Left.** Comparison of diffusion Real-ISR methods (ResShift, SinSR, OSEDiff, SUPIR) with the proposed RSD method. RSD has the following advantages: **(1)** It outperforms SinSR in perceptual quality; **(2)** It is more computationally efficient than OSEDiff; see Table 3. ("-N" behind the method name is NFE; brackets show full-image MUSIQ↑ , zoom $\times 5$ for details). **Right.** Comparison of diffusion SR methods on RealSR. RSD (**Ours**) achieves top scores on most metrics while remaining computationally efficient compared to T2I methods.

However, ResShift remains $10\times$ slower than GANs (Yue et al., 2023, Table 2), highlighting the challenge of accelerating Real-ISR DMs while preserving perceptual quality. SinSR (Wang et al., 2024b) showed that reducing ResShift's NFE further degrades performance and proposed a 1-step **knowledge distillation** using deterministic sampling. Unfortunately, SinSR tends to produce blurred results (second row of Figure 3), as reported in recent studies (Chen et al., 2025; Dong et al., 2025).

Another acceleration strategy is to distill pre-trained *text-to-image* (T2I) models with **variational score distillation** (VSD) (Wang et al., 2023c; Yin et al., 2024b), as proposed in OSEDiff (Wu et al., 2024a). Although this reduces NFE to one and improves perceptual quality compared to ResShift and SinSR, distilled T2I-based SR models have limitations: 1) they have $\times 10$ more parameters than SinSR and a higher training and inference cost (Table 3); 2) they have lower full-reference fidelity metrics (PSNR and SSIM (Wang et al., 2004), Table 2). These limitations motivate two questions.

1. Are knowledge and variational score distillations the best methods for 1-step Real-ISR DMs?
2. Can we unite the best of two worlds for SinSR and OSEDiff to achieve 1-step diffusion SR with *T2I-level perceptual quality*, like OSEDiff, and *fast training and inference cost*, like SinSR?

Contributions. Our main contributions are the following:

(I) Theory. Inspired by SinSR and recent image-to-image DM distillation methods (He et al., 2024; Gushchin et al., 2025), we propose a novel objective for 1-step distillation of SR DMs in **discrete time** and derive its tractable version. We show the difference between the proposed objective and the VSD objective. Motivated by ResShift's good perception-distortion trade-off and its justified diffusion process, we build our method on top of it and name it **RSD**: **R**esidual **S**hifting **D**istillation.

(II) Practice. We show that RSD, trained with the proposed objective, outperforms the teacher for the Real-ISR problem in multiple perceptual metrics, including LPIPS (Zhang et al., 2018), CLIPIQA (Wang et al., 2023a), and MUSIQ (Ke et al., 2021). Our discrete-time RSD objective substantially outperforms the related continuous-time IBMD objective (Gushchin et al., 2025) for the Real-ISR problem in perceptual metrics and computational training and inference costs (Appendix A.3). Our method improves the trade-off between fidelity, perceptual quality, and computational efficiency for Real-ISR with DMs in several aspects, as shown in Figure 1 and Table 3:

1. **Perceptual quality**. Compared to SinSR, the other 1-step ResShift distillation method, RSD achieves better perceptual results on synthetic and Real-ISR benchmarks and has faster training.
2. **Performance-efficiency trade-off**. Compared to the T2I-based 1-step diffusion SR model of OSEDiff, our method achieves competitive perceptual quality while requiring substantially lower computational cost and budget, bringing diffusion SR closer to real-time consumer applications.

2 Related Work

GAN-based SR models. With the rise of GANs (Goodfellow et al., 2014), GAN-based SR methods (Ledig et al., 2017) achieved much better perceptual quality than previous regression-based approaches (Kim et al., 2016). Real-ESRGAN (Wang et al., 2021) and BSRGAN (Zhang et al., 2021) introduced complex degradation pipelines to synthesize LR–HR pairs that better model real-world data, overcoming earlier fixed degradations (e.g., bicubic) that limited generalization. These degradations were later widely adopted by diffusion SR models (Yue et al., 2023; Wu et al., 2024a).

Diffusion SR models. SR methods, which are based on DMs (Sohl-Dickstein et al., 2015; Song & Ermon, 2019; Ho et al., 2020), can be categorized by how they utilize the LR image. The first

category uses the LR image as a condition for the denoiser (Rombach et al., 2022; Saharia et al., 2023; Luo et al., 2023). Another category argues that a Gaussian prior is suboptimal for SR because the LR input already provides the structure; accordingly, the second category initializes denoising from a noised LR image (Yue et al., 2023; Liu et al., 2023b). Its representative method, ResShift (Yue et al., 2023), has two advantages: **(1)** strong perceptual performance for blind Real-ISR with only 15 NFE in latent-space of autoencoder (Esser et al., 2021), while I2SB (Liu et al., 2023b) considers simple degradations and requires hundreds of NFEs in pixel space; **(2)** compared to LDM (Rombach et al., 2022), it has $\times$2-4 faster inference with 15 NFE only and a better perception-distortion trade-off.

Acceleration of diffusion SR models. Despite superior generative performance (Dhariwal & Nichol, 2021), DMs have a slow inference. To mitigate this issue, various acceleration techniques have been proposed, with distillation among the most effective. These methods have also been extended to diffusion SR models. SinSR (Wang et al., 2024b) applied knowledge distillation to ResShift, achieving performance comparable to the teacher with only 1 NFE with consistency-preserving supervised loss. We draw inspiration from distillation methods that involve training an auxiliary "fake" model (Yin et al., 2024a; Huang et al., 2024; Zhou et al., 2024; Gushchin et al., 2025). We discuss the relation of our method to these approaches in Appendix A. CTMSR (You et al., 2025) proposed a 1-step distillation-free method, which is based on recent advances in consistency training (Song et al., 2023; Song & Dhariwal, 2024) and used the architecture, which is similar to ResShift.

T2I-based SR models. Recent studies (Wu et al., 2024a;b; Dong et al., 2025) show that ResShift and SinSR underperform in perceptual metrics compared to SR models, which apply pre-trained T2I models. This may reflect a limited generalization due to the absence of large-scale SR training data. In contrast, T2I models trained on billions of image–text pairs are natural candidates for the Real-ISR problem. Adapting T2I models to SR typically involves two components: **(1)** LR conditioning with controllers such as LoRA layers (OSEDiff, PiSA-SR (Sun et al., 2025)), ControlNet (Zhang et al., 2023) (SUPIR (Yu et al., 2024)) or other modules (StableSR (Wang et al., 2024a)); **(2)** prompts for LR images are used as predefined (StableSR, TSD-SR (Dong et al., 2025)) or extracted with additional models (SUPIR). The most notable challenge in T2I-based Real-ISR models is the high computational cost, as many of them require tens or hundreds of NFE (StableSR, SUPIR). Recent one-step diffusion distillation methods utilize variational score distillation (VSD) (Wang et al., 2023c) (OSEDiff) or target score distillation (TSD-SR (Dong et al., 2025)). These methods greatly accelerate inference, but do not address billion-parameter T2I architectures. To reduce the model, AdcSR (Chen et al., 2025) applies knowledge distillation to OSEDiff with adversarial training of a compressed student obtained by pruning teacher modules. The second challenge is noise-dependent prediction instability, which can lead to poor fidelity (Sun et al., 2024). PiSA-SR (Sun et al., 2025) enables adjusting the perception-distortion trade-off (Blau & Michaeli, 2018) during inference without re-training.

3 METHOD

Our presentation of the proposed RSD method is split as follows: ResShift formulation in §3.1; formulation and derivation of our method in §3.2; multistep RSD training in §3.3; introduction of additional supervised losses in §3.4; formulation of the final objective of the RSD method in §3.5; discussion of the novelty of RSD relative to existing diffusion distillation Real-ISR methods in §3.6.

Remark. While we derive our distillation method for ResShift, we note that ResShift is essentially a conditional DDPM (Ho et al., 2020), where the forward process ends in a Gaussian centered at the LR image. RSD can be generalized for any DMs built on DDPM, as we discuss in Appendix A.4.

3.1 BACKGROUND

As a diffusion model, ResShift can be described by specifying the forward (noising) process, the parameterization of the reverse (denoising) process, and the objective for training the reverse process.

Forward process. Consider a pair of (LR, HR) images $(y_0, x_0) \sim p_{\text{data}}(y_0, x_0)$. For a residual $e_0 = y_0 - x_0$, ResShift uses the forward process with the Gaussian kernel:

$$q(x_t|x_{t-1}, y_0) = \mathcal{N}(x_t|x_{t-1} + \alpha_t\, e_0, \kappa^2\alpha_t\mathbf{I}), \tag{1}$$

where $\alpha_t = \eta_t - \eta_{t-1}$, $\alpha_1 = \eta_1$ and $\{\eta\}_{t=1}^T$ is a schedule, while κ is a hyper-parameter controlling the noise variance. The corresponding posterior distribution is given as follows:

$$q(x_{t-1}|x_t,x_0,y_0) = \mathcal{N}\left(x_{t-1}\,\middle|\,\frac{\eta_{t-1}}{\eta_t}x_t + \frac{\alpha_t}{\eta_t}x_0, \frac{\kappa^2\eta_{t-1}}{\eta_t}\alpha_t\mathbf{I}\right) \tag{2}$$

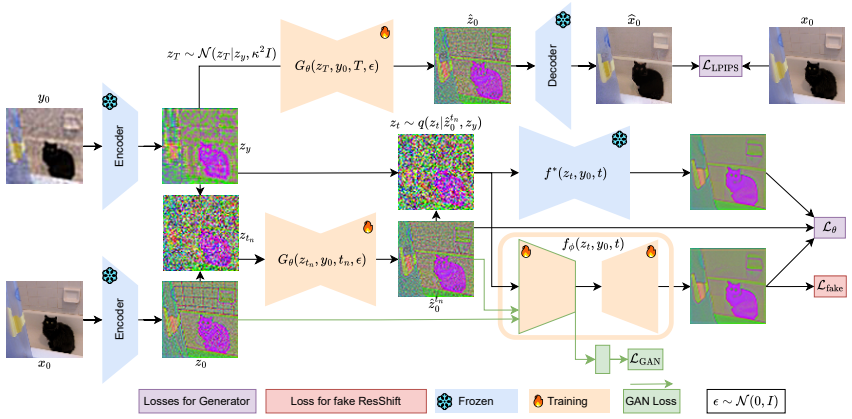

Figure 2: **The training framework of RSD.** After we encode the (LR, HR) pair (y_0, x_0) into latents (z_y, z_0), we obtain z_{t_n} via the forward process (1), generate $\widehat{z}_0^{t_n}$ and sample z_t using posterior sampling (2). We process z_t using both fake and teacher ResShift models and compute the distillation losses $\mathcal{L}_\theta$ and $\mathcal{L}_{\text{fake}}$ (8). For $\mathcal{L}_{\text{LPIPS}}$, we sample z_T from z_y, generate $\widehat{z}_0$ from timestep T and decode it to obtain $\widehat{x}_0$. For $\mathcal{L}_{\text{GAN}}$, we use an additional discriminator head on top of encoder of f_ϕ.

Reverse process. ResShift defines the reverse process as follows:

$$p_\theta(x_0|y_0) = \int p(x_T|y_0) \prod_{t=1}^{T} p_\theta(x_{t-1}|x_t, y_0) dx_{1:T} \tag{3}$$

Here $p(x_T|y_0) = \mathcal{N}(x_T|y_0, \kappa^2 I)$, and $p_\theta(x_{t-1}|x_t, y_0)$ is a Gaussian reverse transition kernel with parameters μ_θ, Σ_θ.

Objective. ResShift sets $\Sigma_\theta(t)$ to be independent of x_t and y_0 and reparameterizes $\mu_\theta(x_t, y_0, t)$ as:

$$\mu_\theta(x_t, y_0, t) = \frac{\eta_{t-1}}{\eta_t} x_t + \frac{\alpha_t}{\eta_t} f_\theta(x_t, y_0, t), \tag{4}$$

where f_θ is a neural network that predicts x_0. The training objective of ResShift is given as follows:

$$\min_\theta \sum_{t=1}^{T} \mathbb{E}_{p(x_0, y_0, x_t)} w_t \| f_\theta(x_t, y_0, t) - x_0 \|^2, \tag{5}$$

where $w_t > 0$ and $p(x_0, y_0, x_t)$ are given by the ResShift forward process, as detailed in Appendix I.

3.2 Residual Shifting Distillation (RSD)

We distill the ResShift *teacher* $f^*(x_t, y_0, t)$ into a stochastic one-step *student* generator G_θ to map y_0 to x_0, which is parameterized as $\widehat{x}_0 = G_\theta(x_T, y_0, \epsilon)$ with $x_T \sim q(x_T|y_0), \epsilon \sim \mathcal{N}(0, I)$. We parametrize the generator $G_\theta(x_T, y_0, \epsilon)$ to have three inputs: the LR image y_0, its noisy version $x_T \sim q(x_T|y_0)$, and additional noise $\epsilon \sim \mathcal{N}(0, I)$. We denote by $p_\theta(\widehat{x}_0|x_T, y_0)$ the distribution of G_θ produced for random ϵ. We train G_θ so that a **ResShift model f_{G_θ} trained on its outputs matches the teacher**, assuming $f_{G_\theta} \approx f^*$ leads to the same generated and real (LR, HR) distributions:

$$f_{G_\theta} \approx f^* \Rightarrow p_\theta(y_0, x_0) \approx p_{\text{data}}(y_0, x_0) \tag{6}$$

Based on this assumption, we align student G_θ by producing the data from the same distribution of the (LR, HR) pairs as were in the train datasets for the teacher network f^*:

$$\min_\theta \mathcal{L}_\theta, \quad \mathcal{L}_\theta \stackrel{\text{def}}{=} \sum_{t=1}^{T} w_t \mathbb{E}_{p_\theta(\widehat{x}_0, y_0, x_t)} \| f_{G_\theta}(x_t, y_0, t) - f^*(x_t, y_0, t) \|_2^2, \tag{7}$$

where $p_\theta(\widehat{x}_0, y_0, x_t)$ is induced by $\widehat{x}_0$ and $q(x_t|\widehat{x}_0, y_0)$ (2). In turn, $f_{G_\theta}(x_t, y_0, t)$ is the ResShift trained on the generator data $p_\theta(\widehat{x}_0|y_0)$. $\nabla_\theta \mathcal{L}_\theta$ includes $\nabla_\theta f_{G_\theta}(x_t, y_0, t)$, which is not tractable since backpropagation through the whole training of the ResShift $f_{G_\theta}(x_t, y_0, t)$ is computationally infeasible (Appendix K). We propose an equivalent tractable form of $\mathcal{L}_\theta$.

Proposition 3.1. *Given a teacher model f^*, the loss in Equation* (7) *can be given in a tractable form:*

$$\mathcal{L}_\theta = -\min_\phi \Big\{ \sum_t w_t \mathbb{E}_{p_\theta(\widehat{x}_0, y_0, x_t)} \Big(-\|f^*(x_t, y_0, t)\|_2^2 + \underbrace{\|f_\phi(x_t, y_0, t)\|_2^2 - 2\langle f_\phi(x_t, y_0, t) - f^*(x_t, y_0, t), \widehat{x}_0 \rangle}_{\text{This objective } \mathcal{L}_{fake} \text{ is equivalent to training a fake model } f_\phi \text{ with objective (5)}} \Big) \Big\} \tag{8}$$

Here, f_ϕ is an auxiliary ResShift trained via $\mathcal{L}_{fake}$ in Equation (8) to estimate $\mathcal{L}_\theta$. Minimizing loss in Equation (8) over ϕ is equivalent to training a "fake" ResShift using data generated by G_θ.

Thus, we avoid backpropagation through training by incorporating fake model training into $\mathcal{L}_\theta$. The proof is in Appendix K. In Appendix A.1, we compare RSD with the VSD objective and show that

$$\mathcal{L}_\theta = \mathbb{E}_{p(y_0)} \mathcal{D}_{\mathrm{KL}} \left(p(x_{0:T}|y_0) \,\|\, p^*(x_{0:T}|y_0) \right) \tag{9}$$

3.3 Multistep RSD training

To improve RSD, we use multistep generator training (Yin et al., 2024a; Zhou et al., 2024). We select N timesteps $1 < t_1 < \ldots < t_N = T$ and add timestep conditioning to $G_\theta(x_t, t, y_0, \epsilon)$. Let $\widehat{x}_0^{t_n}$ denote the output at timestep $t = t_n$. Then G_θ approximates $p_\theta(\widehat{x}_0|x_{t_n}, y_0) \approx q(x_0|x_{t_n}, y_0)$ for all selected t_n. We sample x_{t_n} from ground-truth pairs $p_{\text{data}}(x_0, y_0)$ via the posterior (2) and train G_θ jointly over all t_n using Proposition 3.1. Inference remains a single-step; multistep training improves robustness and performance (Table 4). For consistency, we denote the single-step output at T by $\widehat{x}_0$.

3.4 Supervised losses

Since the teacher may be biased by approximation errors in estimating x_0, we add supervised losses.

LPIPS loss. Following OSEDiff, we use LPIPS ($\mathcal{L}_{\mathrm{LPIPS}}$ (Zhang et al., 2018)) to match outputs to HR in perceptual feature space, improving textures and structural details beyond teacher guidance. Although OSEDiff also used MSE fidelity, it did not help in our setup.

GAN loss. Inspired by DMD2 (Yin et al., 2024a), we add a GAN loss to better match the HR distribution, using a small discriminator head on features from the fake ResShift bottleneck (Figure 2). Unlike DMD2, which compares marginals of noised data and generator outputs, we find it more effective to compare $p_{\text{data}}(x_0|y_0)$ with $p_\theta(\widehat{x}_0^{t_n}|y_0)$ at each t_n:

$$\mathcal{L}_{\mathrm{GAN}} = \mathbb{E}_{p_{\mathrm{data}}(x_0|y_0)} \big[\log D\big(x_0|y_0\big)\big] - \mathbb{E}_{p_\theta(\widehat{x}_0^{t_n}|y_0)} \big[\log D\big(\widehat{x}_0^{t_n}|y_0\big)\big] \tag{10}$$

3.5 Putting everything together

Translation into a latent space. Although described in the image space (x), ResShift was trained in the latent space (z). We therefore compute $\mathcal{L}_\theta$ and $\mathcal{L}_{\mathrm{GAN}}$ in the latent space to avoid extra encode/decode, while keeping $\mathcal{L}_{\mathrm{LPIPS}}$ in the image space since the LPIPS network was trained there.

Final algorithm. The final loss function for each t_n is:

$$\mathcal{L}_\theta + \lambda_1 \mathcal{L}_{\mathrm{LPIPS}} + \lambda_2 \mathcal{L}_{\mathrm{GAN}} \tag{11}$$

RSD algorithm with the respective notation is given in Appendix B, with an illustration in Figure 2.

3.6 Difference between RSD, VSD, and ADD

We argue that RSD (7) differs from VSD. We detail conceptual and computational differences and relate RSD to VSD (Eq. 5 in (Wang et al., 2023c)) in Appendix A.1. The key difference is that VSD (Eq. (16)) aligns the teacher and the fake marginals at each t, while RSD (9) matches the joint distribution for all t. In Section 4.2, we discuss the results of RSD and VSD for SR. In Appendix H, we discuss the difference between ADD (Sauer et al., 2025), AddSR (Xie et al., 2024), and RSD.

4 Experiments

In this section, we pursue two goals: **(1)** to show that our *distillation* method outperforms existing *distillation* methods under the same experimental setup. We chose the ResShift setup to be consistent with our teacher model and SinSR. We compare RSD with the SOTA ResShift distillation baseline, SinSR, and with a VSD-based ResShift variant, **ResShift-VSD** (Appendix A.1); **(2)** to show that RSD is perceptually competitive with recent T2I-based SR (e.g., OSEDiff, SUPIR) while requiring much less training and inference computational costs. These goals are supported by evaluations using the SinSR and OSEDiff setups. We report RSD (**Ours**, distill only) trained with distillation loss only and RSD (**Ours**) trained with additional losses (§3.4). Appendix C provides all relevant experimental details. We also compare RSD with very recent models of CTMSR, AdcSR, PiSA-SR, and TSD-SR.

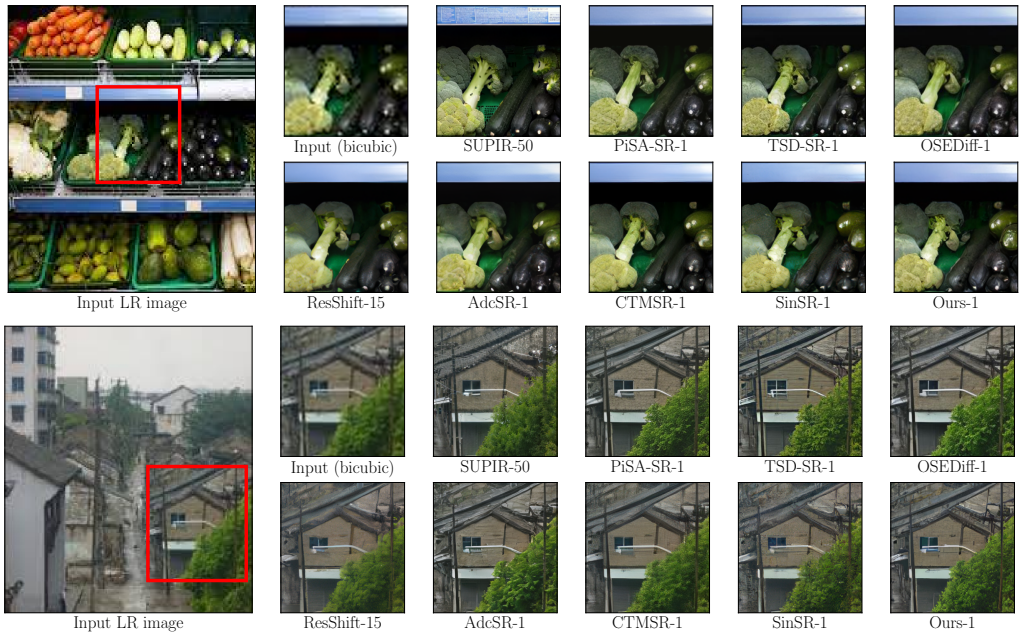

Figure 3: Comparison on RealSet65 (Yue et al., 2023) for diffusion SR models. Bottom images: ResShift, AdcSR, CTMSR, SinSR, and the proposed RSD. Top images: bicubic LR, SUPIR, PiSA-SR, TSD-SR, and OSEDiff. Please zoom in $\times 5$ times for a better view.

4.1 Experimental setup

Training and evaluation details. For a fair comparison, we follow the *training setup* of ResShift and SinSR: 256×256 HR ImageNet crops (Deng et al., 2009) with LR generated by Real-ESRGAN degradations (Wang et al., 2021) with $\times 4$ SR factor. We distill the ResShift teacher used in SinSR. We follow two *evaluation setups* from SinSR and OSEDiff ($\times 4$ SR factor). (1) Following SinSR, we use the full-size RealSR (Cai et al., 2019) and RealSet65 (Yue et al., 2023). (2) Following OSEDiff, we use test 512×512 HR crops from StableSR (Wang et al., 2024a) with synthetic DIV2K-Val (Agustsson & Timofte, 2017), and real-world pairs from RealSR and DRealSR (Wei et al., 2020).

Compared methods. We consider two different experimental setups with different baseline comparisons of SinSR (Wang et al., 2024b, Tables 1 and 2) and OSEDiff (Wu et al., 2024a, Table 1). We compare RSD against **diffusion SR models** in the main text: models with relatively small architectures (ResShift, SinSR, CTMSR), and recent T2I-based SR models - one-step OSEDiff and multistep SUPIR. We highlight that closely related models to RSD, such as ResShift, SinSR, and CTMSR, were only compared with **early T2I-based SR models**, namely LDM (Rombach et al., 2022) and StableSR. In addition to OSEDiff and SUPIR, we extend the comparison of diffusion SR methods without T2I prior to the very recent SOTA one-step T2I-based SR methods (AdcSR, PiSA-SR, and TSD-SR) on SinSR evaluation datasets. In Appendix D, we provide quantitative results of other baselines, including GANs, multistep T2I-based SR models, and other one-step SR models.

Metrics. Each setup employs different evaluation metrics, which we adopt from SinSR and OSEDiff. For the SinSR protocol, we report no-reference metrics of CLIPIQA and MUSIQ. For the OSEDiff protocol, we report fidelity (PSNR, SSIM), full-reference perceptual metrics (LPIPS, DISTS (Ding et al., 2020)) and no-reference metrics (NIQE (Zhang et al., 2015), MANIQA-PIPAL (Yang et al., 2022), MUSIQ, CLIPIQA). PSNR and SSIM are computed on the Y channel in the YCbCr space following SinSR and OSEDiff. We also report the distribution alignment metric (FID (Heusel et al., 2017)) in Table 2, since DIV2K-Val have 3k image pairs, while other datasets have ≤ 100 pairs.

4.2 Experimental results

Quantitative comparisons. The key quantitative results are summarized in Table 1 and Table 2. We group methods into two classes: 1) diffusion SR models with compact architectures (ResShift, SinSR, CTMSR, RSD), which are mostly related to our work; 2) T2I-based SR models with heavy architectures (SUPIR, OSEDiff, AdcSR, PiSA-SR, TSD-SR). We analyze the results as follows.

Table 1: Results on real-world datasets. The best and second best results are highlighted in **bold** and underline.

Methods	T2I prior	NFE	Datasets						
			RealSR					*RealSet65*	
			PSNR↑	SSIM↑	LPIPS↓	CLIPIQA↑	MUSIQ↑	CLIPIQA↑	MUSIQ↑
SUPIR	yes, > 450M params	50	24.38	0.698	0.331	0.5449	63.676	0.6133	66.460
OSEDiff		1	25.25	0.737	0.299	0.6772	67.602	0.6836	68.853
AdcSR		1	25.63	0.735	0.300	0.7033	67.550	0.7044	69.185
PiSA-SR		1	25.59	0.750	**0.271**	0.6678	67.993	0.7062	70.208
TSD-SR		1	24.88	0.723	0.281	0.7336	**69.871**	0.7263	**70.958**
ResShift	no, < 180M params	15	**26.49**	0.754	0.360	0.5958	59.873	0.6537	61.330
CTMSR		1	26.18	**0.765**	0.294	0.6449	64.796	0.6893	67.173
SinSR (distill only)		1	26.14	0.732	0.357	0.6119	57.118	0.6822	61.267
SinSR		1	25.83	0.717	0.365	0.6887	61.582	0.7150	62.169
ResShift-VSD (Appendix A.1)		1	23.96	0.616	0.466	0.7479	63.298	**0.7606**	66.701
RSD (**Ours**, distill only)		1	24.92	0.696	0.355	**0.7518**	66.430	0.7534	68.383
RSD (**Ours**)		1	25.91	0.754	0.273	0.7060	65.860	0.7267	69.172

Table 2: Results on crops 512×512. The best and second best results are highlighted in **bold** and underline.

Datasets	Methods	T2I prior	NFE	PSNR↑	SSIM↑	LPIPS↓	DISTS↓	NIQE↓	MUSIQ↑	MANIQA↑	CLIPIQA↑	FID↓
DIV2K-Val	SUPIR	yes, > 1.7B params	50	22.13	0.5280	0.3923	0.2314	5.6758	63.82	0.5933	**0.7147**	31.46
	OSEDiff		1	23.72	0.6108	0.2941	0.1976	**4.7097**	67.97	**0.6148**	0.6683	**26.32**
	ResShift	no, < 180M params	15	24.65	0.6181	0.3349	0.2213	6.8212	61.09	0.5454	0.6071	36.11
	SinSR		1	24.41	0.6018	0.3240	0.2066	6.0159	62.82	0.5386	0.6471	35.57
	CTMSR		1	**24.88**	**0.6265**	0.3026	0.2040	5.1146	65.62	0.5165	0.6601	34.15
	RSD (**Ours**)		1	23.91	0.6042	**0.2857**	**0.1940**	5.1987	**68.05**	0.5937	0.6967	34.84
DrealSR	SUPIR	yes, > 1.7B params	50	24.93	0.6360	0.4263	0.2823	7.4336	59.39	0.5537	0.6799	164.86
	OSEDiff		1	27.92	**0.7835**	**0.2968**	**0.2165**	6.4902	**64.65**	**0.5899**	0.6963	**135.30**
	ResShift	no, < 180M params	15	28.46	0.7673	0.4006	0.2656	8.1249	50.60	0.4586	0.5342	172.26
	SinSR		1	28.36	0.7515	0.3665	0.2485	6.9907	55.33	0.4884	0.6383	170.57
	CTMSR		1	**28.65**	0.7834	0.3238	0.2358	**6.1828**	59.78	0.4861	0.6497	163.63
	RSD (**Ours**)		1	27.40	0.7559	0.3042	0.2343	6.2577	62.03	0.5625	**0.7019**	167.47
RealSR	SUPIR	yes, > 1.7B params	50	23.61	0.6606	0.3589	0.2492	5.8877	63.21	0.5895	0.6709	128.35
	OSEDiff		1	25.15	0.7341	0.2921	**0.2128**	5.6476	**69.09**	**0.6326**	0.6693	**123.49**
	ResShift	no, < 180M params	15	**26.31**	0.7421	0.3421	0.2498	7.2365	58.43	0.5285	0.5442	141.71
	SinSR		1	26.28	0.7347	0.3188	0.2353	6.2872	60.80	0.5385	0.6122	135.93
	CTMSR		1	25.98	**0.7546**	0.2897	0.2208	**5.5546**	64.26	0.5270	0.6318	135.35
	RSD (**Ours**)		1	25.61	0.7420	**0.2675**	0.2205	5.7500	66.02	0.5930	**0.6793**	138.23

(1) With identical training data, RSD outperforms the teacher model of ResShift and our closest competitor, SinSR, by a large margin for **all perceptual** metrics (LPIPS, CLIPIQA, MUSIQ) and **all test datasets**. RSD also shows comparable or better results than ResShift-VSD (Appendix A.1). CTMSR is the recent one-step diffusion SR method, which also used ImageNet for training and can be fairly comparable to RSD. RSD achieves better results in **all real-world** datasets in most perceptual metrics (LPIPS, CLIPIQA, MUSIQ) with a noticeable improvement in MANIQA in Table 2 .

(2) For Real-ISR data, RSD achieves the best CLIPIQA and top-1 or top-2 MUSIQ relative to T2I-based OSEDiff and SUPIR. RSD has a worse CLIPIQA than SUPIR for synthetic DIV2K but better than OSEDiff. However, SUPIR also produce excessive details, which leads to poor consistency with the HR image, as seen by PSNR, SSIM, and LPIPS. We note that RSD, even with slightly worse MUSIQ, achieves PSNR and SSIM that are much better than SUPIR and comparable to or better than OSEDiff for most setups while using a much smaller number of parameters and GPU memory, as shown in Table 3. Compared to SOTA 1-step diffusion T2I-based SR methods (AdcSR, PiSA-SR, TSD-SR), RSD has competitive perceptual (LPIPS, CLIPIQA) and fidelity quality in Table 1 .

(3) In Table 2 , we show that RSD achieves top-2 or top-1 perceptual metrics compared to OSEDiff and all diffusion models, which were trained on ImageNet. We highlight the different training HR resolutions of RSD and OSEDiff - we used HR crops of the size 256×256 as in the teacher model of ResShift, while OSEDiff used HR crops of the size 512×512 for training on LSDIR (Li et al., 2023), which aligns with the crop size in Table 2 . Due to space limitation, we provide quantitative results for the recent SOTA models of AdcSR, PiSA-SR, and TSD-SR and other diffusion and GAN models for Table 2 and for other datasets, including full-size images from RealLR200 (Wu et al., 2024b), RealLQ250 (Ai et al., 2024), DRealSR (Wei et al., 2020) and ImageNet-Test (Yue et al., 2023) in Appendix D. We also discuss the RSD results trained on 512×512 HR images in Appendix G.

Table 3: Inference (NVIDIA A100, SR factor $\times 4$) and training budget. The best values are highlighted in **bold**.

T2I prior	Yes					No			
Methods	SUPIR	OSEDiff	AdcSR	PiSA-SR	TSD-SR	ResShift	SinSR	CTMSR	RSD (**Ours**)
Inference Step (NFE)	50	**1**	**1**	**1**	**1**	15	**1**	**1**	**1**
Inference Time (s)	17.704	0.075	**0.024**	0.089	0.074	0.643	0.060	0.059	0.059
# Total Param (M)	4801	1775	456	1290	2207	174	174	**172**	174
Maximum GPU memory (MB)	52535	3651	3940	4771	4611	1167	570	904	**539**
Training time (hours / # GPU)	240 / 64 A6000	24 / 4 A100	124 / 8 A100	5.5 / 4 A100	96 / 8 A100	110 / 1 A100	60 / 1 A100	58 / 4 A100	**5 / 4 A100**

Table 4: Impact of multistep training of our RSD on RealSR. The best and second best results are highlighted in **bold** and underline.

N	PSNR↑	LPIPS↓	CLIPIQA↑	MUSIQ↑
1	24.82	0.4052	0.7444	64.290
2	24.77	0.3772	**0.7523**	65.760
4	24.92	0.3552	0.7518	66.430
8	25.63	0.3199	0.7286	**66.445**
15	**25.91**	**0.2940**	0.6857	65.689

Table 5: Effect of incorporating supervised losses on RealSR. The best and second best results are highlighted in **bold** and underline.

Method	PSNR↑	LPIPS↓	CLIPIQA↑	MUSIQ↑
$\lambda_{1,2} = 0$	24.92	0.3552	**0.7518**	66.430
$\lambda_1 \neq 0$	**26.01**	**0.2708**	0.7089	65.178
$\lambda_2 \neq 0$	24.98	0.3064	0.6970	**67.615**
Ours	25.91	0.2726	0.7060	65.860

Qualitative comparisons. We visually compare RSD with baselines on test images from RealSet65 in Figure 3. As illustrated in the top image, SUPIR tends to produce rich details that semantically do not correspond to the LR image (e.g., excessive broccoli). ResShift, SinSR, and CTMSR produce conservative images, which may struggle from severely blurred details like the house's roof on the bottom image. OSEDiff may hallucinate excessive details, as can be seen for the panda's nose in Figure 1. RSD compromises between the good details of OSEDiff and SUPIR and the high fidelity of ResShift and SinSR. AdcSR, PiSA-SR, and TSD-SR typically produce more realistic, texture-rich outputs than OSEDiff. However, they can still hallucinate and fail (Appendix E). Additional visual results for RSD and other methods are given in Appendices E and L.

Complexity comparisons. We compare the complexity of competing diffusion SR models in Table 3, including NFE, inference time, parameters, and the maximum required GPU memory during inference, report training time and GPU training usage. For inference, all methods are tested on an NVIDIA A100 GPU with 256×256 HR inputs following SinSR (Wang et al., 2024b, Table 3) and CTMSR (You et al., 2025, Table 3). RSD and SinSR use at least $\times 5$ less GPU memory and $\times 10$ fewer parameters than T2I-based models. We also note the training efficiency of RSD compared to SinSR: RSD is a **simulation-free method**. SinSR runs the ResShift teacher for training all 15 steps, while RSD avoids it (Algorithm 1, Appendix B). In Appendix C, we discuss that SinSR empirically converges roughly 3 times slower than RSD. Although CTMSR is a distillation-free method, we show in Appendix E that it's total training time is bigger than the total training time of ResShift teacher and its distillation with RSD. Despite strong perceptual quality, recent one-step T2I-based SR methods (AdcSR, PiSA-SR, TSD-SR) require substantially larger compute budgets than RSD. For example, compared to TSD-SR, RSD training is $\times 19$ faster using $\times 2$ fewer GPUs, while TSD-SR uses $\times 13$ more parameters and $\times 8$ more GPU memory for the inference. More discussion of performance-efficiency trade-off for RSD and other SOTA methods is given in Appendix E.

4.3 Ablation study

Multistep training. We ablate multistep training (§3.3) across timestep configurations. In Table 4 we compare numbers of evenly spaced timesteps $N \in 1, \ldots, 15$ with the maximum N matching that of ResShift. We choose $N = 4$ for the best perception–distortion trade-off (Blau & Michaeli, 2018).

Supervised losses. Table 5 examines the impact of incorporating supervised losses, as discussed in §3.4. These losses substantially improve PSNR and LPIPS while leading to acceptable shifts in no-reference metrics (CLIPIQA, MUSIQ). In all evaluations, we use full-size images from RealSR.

We provide additional ablation studies on the number of updates for the fake model per student update, training stability of RSD, and visual results for Table 5 in Appendix F.

5 Conclusion and future work

In this work, we propose RSD, a novel approach to distill the ResShift model into a student network with a single inference step. Our model is computationally efficient thanks to its ResShift framework, but remains constrained by its teacher capacity issue, as validated in Appendix G. A more advanced teacher, such as a T2I-based model, could improve performance and enable the application of our method at higher resolutions. We discuss the limitations of RSD and failure cases in Appendix J.

REFERENCES

Eirikur Agustsson and Radu Timofte. Ntire 2017 challenge on single image super-resolution: Dataset and study. In *Proceedings of the IEEE conference on computer vision and pattern recognition workshops*, pp. 126–135, 2017.

Yuang Ai, Xiaoqiang Zhou, Huaibo Huang, Xiaotian Han, Zhengyu Chen, Quanzeng You, and Hongxia Yang. Dreamclear: High-capacity real-world image restoration with privacy-safe dataset curation. In A. Globerson, L. Mackey, D. Belgrave, A. Fan, U. Paquet, J. Tomczak, and C. Zhang (eds.), *Advances in Neural Information Processing Systems*, volume 37, pp. 55443–55469. Curran Associates, Inc., 2024. doi: 10.52202/079017-1761.

Yochai Blau and Tomer Michaeli. The perception-distortion tradeoff. In *2018 IEEE/CVF Conference on Computer Vision and Pattern Recognition*, pp. 6228–6237, 2018. doi: 10.1109/CVPR.2018.00652.

Jianrui Cai, Hui Zeng, Hongwei Yong, Zisheng Cao, and Lei Zhang. Toward real-world single image super-resolution: A new benchmark and a new model. In *2019 IEEE/CVF International Conference on Computer Vision (ICCV)*, pp. 3086–3095, 2019. doi: 10.1109/ICCV.2019.00318.

Bin Chen, Gehui Li, Rongyuan Wu, Xindong Zhang, Jie Chen, Jian Zhang, and Lei Zhang. Adversarial diffusion compression for real-world image super-resolution. In *Proceedings of the Computer Vision and Pattern Recognition Conference (CVPR)*, pp. 28208–28220, June 2025.

Chaofeng Chen and Jiadi Mo. IQA-PyTorch: Pytorch toolbox for image quality assessment. [Online]. Available: `https://github.com/chaofengc/IQA-PyTorch`, 2022.

Chaofeng Chen, Xinyu Shi, Yipeng Qin, Xiaoming Li, Xiaoguang Han, Tao Yang, and Shihui Guo. Real-world blind super-resolution via feature matching with implicit high-resolution priors. 2022.

Hamadi Chihaoui, Abdelhak Lemkhenter, and Paolo Favaro. Blind image restoration via fast diffusion inversion. In A. Globerson, L. Mackey, D. Belgrave, A. Fan, U. Paquet, J. Tomczak, and C. Zhang (eds.), *Advances in Neural Information Processing Systems*, volume 37, pp. 34513–34532. Curran Associates, Inc., 2024. doi: 10.52202/079017-1088.

Jia Deng, Wei Dong, Richard Socher, Li-Jia Li, Kai Li, and Li Fei-Fei. Imagenet: A large-scale hierarchical image database. In *2009 IEEE Conference on Computer Vision and Pattern Recognition*, pp. 248–255, 2009. doi: 10.1109/CVPR.2009.5206848.

Prafulla Dhariwal and Alexander Nichol. Diffusion models beat gans on image synthesis. In M. Ranzato, A. Beygelzimer, Y. Dauphin, P.S. Liang, and J. Wortman Vaughan (eds.), *Advances in Neural Information Processing Systems*, volume 34, pp. 8780–8794. Curran Associates, Inc., 2021.

Keyan Ding, Kede Ma, Shiqi Wang, and Eero P Simoncelli. Image quality assessment: Unifying structure and texture similarity. *IEEE transactions on pattern analysis and machine intelligence*, 44(5):2567–2581, 2020.

Chao Dong, Chen Change Loy, Kaiming He, and Xiaoou Tang. Image super-resolution using deep convolutional networks. *IEEE Transactions on Pattern Analysis and Machine Intelligence*, 38(2): 295–307, 2016. doi: 10.1109/TPAMI.2015.2439281.

Linwei Dong, Qingnan Fan, Yihong Guo, Zhonghao Wang, Qi Zhang, Jinwei Chen, Yawei Luo, and Changqing Zou. Tsd-sr: One-step diffusion with target score distillation for real-world image super-resolution. In *Proceedings of the Computer Vision and Pattern Recognition Conference (CVPR)*, pp. 23174–23184, June 2025.

Patrick Esser, Robin Rombach, and Björn Ommer. Taming transformers for high-resolution image synthesis. In *2021 IEEE/CVF Conference on Computer Vision and Pattern Recognition (CVPR)*, pp. 12868–12878, 2021. doi: 10.1109/CVPR46437.2021.01268.

Patrick Esser, Sumith Kulal, Andreas Blattmann, Rahim Entezari, Jonas Müller, Harry Saini, Yam Levi, Dominik Lorenz, Axel Sauer, Frederic Boesel, Dustin Podell, Tim Dockhorn, Zion English, and Robin Rombach. Scaling rectified flow transformers for high-resolution image synthesis. In

Ruslan Salakhutdinov, Zico Kolter, Katherine Heller, Adrian Weller, Nuria Oliver, Jonathan Scarlett, and Felix Berkenkamp (eds.), *Proceedings of the 41st International Conference on Machine Learning*, volume 235 of *Proceedings of Machine Learning Research*, pp. 12606–12633. PMLR, 21–27 Jul 2024. URL https://proceedings.mlr.press/v235/esser24a.html.

Daniel Glasner, Shai Bagon, and Michal Irani. Super-resolution from a single image. In *2009 IEEE 12th International Conference on Computer Vision*, pp. 349–356, 2009. doi: 10.1109/ICCV.2009.5459271.

Ian Goodfellow, Jean Pouget-Abadie, Mehdi Mirza, Bing Xu, David Warde-Farley, Sherjil Ozair, Aaron Courville, and Yoshua Bengio. Generative adversarial nets. In Z. Ghahramani, M. Welling, C. Cortes, N. Lawrence, and K.Q. Weinberger (eds.), *Advances in Neural Information Processing Systems*, volume 27. Curran Associates, Inc., 2014.

Nikita Gushchin, David Li, Daniil Selikhanovych, Evgeny Burnaev, Dmitry Baranchuk, and Alexander Korotin. Inverse bridge matching distillation. *arXiv preprint arXiv:2502.01362*, 2025.

Guande He, Kaiwen Zheng, Jianfei Chen, Fan Bao, and Jun Zhu. Consistency diffusion bridge models. In A. Globerson, L. Mackey, D. Belgrave, A. Fan, U. Paquet, J. Tomczak, and C. Zhang (eds.), *Advances in Neural Information Processing Systems*, volume 37, pp. 23516–23548. Curran Associates, Inc., 2024.

Martin Heusel, Hubert Ramsauer, Thomas Unterthiner, Bernhard Nessler, and Sepp Hochreiter. Gans trained by a two time-scale update rule converge to a local nash equilibrium. In I. Guyon, U. Von Luxburg, S. Bengio, H. Wallach, R. Fergus, S. Vishwanathan, and R. Garnett (eds.), *Advances in Neural Information Processing Systems*, volume 30. Curran Associates, Inc., 2017.

Jonathan Ho and Tim Salimans. Classifier-free diffusion guidance. In *NeurIPS 2021 Workshop on Deep Generative Models and Downstream Applications*, 2021. URL https://openreview.net/forum?id=qw8AKxfYbI.

Jonathan Ho, Ajay Jain, and Pieter Abbeel. Denoising diffusion probabilistic models. In H. Larochelle, M. Ranzato, R. Hadsell, M.F. Balcan, and H. Lin (eds.), *Advances in Neural Information Processing Systems*, volume 33, pp. 6840–6851. Curran Associates, Inc., 2020.

Edward J Hu, yelong shen, Phillip Wallis, Zeyuan Allen-Zhu, Yuanzhi Li, Shean Wang, Lu Wang, and Weizhu Chen. LoRA: Low-rank adaptation of large language models. In *International Conference on Learning Representations*, 2022. URL https://openreview.net/forum?id=nZeVKeeFYf9.

Zemin Huang, Zhengyang Geng, Weijian Luo, and Guo-jun Qi. Flow generator matching. *arXiv preprint arXiv:2410.19310*, 2024.

Andrey Ignatov, Nikolay Kobyshev, Radu Timofte, and Kenneth Vanhoey. Dslr-quality photos on mobile devices with deep convolutional networks. In *2017 IEEE International Conference on Computer Vision (ICCV)*, pp. 3297–3305, 2017. doi: 10.1109/ICCV.2017.355.

Michal Irani and Shmuel Peleg. Improving resolution by image registration. *Graphical Models and Image Processing*, 53:231–239, 1991.

Xiaozhong Ji, Yun Cao, Ying Tai, Chengjie Wang, Jilin Li, and Feiyue Huang. Real-world super-resolution via kernel estimation and noise injection. In *2020 IEEE/CVF Conference on Computer Vision and Pattern Recognition Workshops (CVPRW)*, pp. 1914–1923, 2020. doi: 10.1109/CVPRW50498.2020.00241.

Junjie Ke, Qifei Wang, Yilin Wang, Peyman Milanfar, and Feng Yang. Musiq: Multi-scale image quality transformer. In *2021 IEEE/CVF International Conference on Computer Vision (ICCV)*, pp. 5128–5137, 2021. doi: 10.1109/ICCV48922.2021.00510.

Jiwon Kim, Jung Kwon Lee, and Kyoung Mu Lee. Accurate image super-resolution using very deep convolutional networks. In *2016 IEEE Conference on Computer Vision and Pattern Recognition (CVPR)*, pp. 1646–1654, 2016. doi: 10.1109/CVPR.2016.182.

Christian Ledig, Lucas Theis, Ferenc Huszár, Jose Caballero, Andrew Cunningham, Alejandro Acosta, Andrew Aitken, Alykhan Tejani, Johannes Totz, Zehan Wang, and Wenzhe Shi. Photo-realistic single image super-resolution using a generative adversarial network. In *2017 IEEE Conference on Computer Vision and Pattern Recognition (CVPR)*, pp. 105–114, 2017. doi: 10.1109/CVPR.2017.19.

Yawei Li, Kai Zhang, Jingyun Liang, Jiezhang Cao, Ce Liu, Rui Gong, Yulun Zhang, Hao Tang, Yun Liu, Denis Demandolx, Rakesh Ranjan, Radu Timofte, and Luc Van Gool. Lsdir: A large scale dataset for image restoration. In *2023 IEEE/CVF Conference on Computer Vision and Pattern Recognition Workshops (CVPRW)*, pp. 1775–1787, 2023. doi: 10.1109/CVPRW59228.2023.00178.

Jie Liang, Hui Zeng, and Lei Zhang. Details or artifacts: A locally discriminative learning approach to realistic image super-resolution. In *2022 IEEE/CVF Conference on Computer Vision and Pattern Recognition (CVPR)*, pp. 5647–5656, 2022a. doi: 10.1109/CVPR52688.2022.00557.

Jie Liang, Hui Zeng, and Lei Zhang. Efficient and degradation-adaptive network for real-world image super-resolution. In Shai Avidan, Gabriel Brostow, Moustapha Cissé, Giovanni Maria Farinella, and Tal Hassner (eds.), *Computer Vision – ECCV 2022*, pp. 574–591, Cham, 2022b. Springer Nature Switzerland. ISBN 978-3-031-19797-0.

Jingyun Liang, Jiezhang Cao, Guolei Sun, Kai Zhang, Luc Van Gool, and Radu Timofte. Swinir: Image restoration using swin transformer. In *2021 IEEE/CVF International Conference on Computer Vision Workshops (ICCVW)*, pp. 1833–1844, 2021. doi: 10.1109/ICCVW54120.2021.00210.

Xinqi Lin, Jingwen He, Ziyan Chen, Zhaoyang Lyu, Bo Dai, Fanghua Yu, Yu Qiao, Wanli Ouyang, and Chao Dong. Diffbir: Toward blind image restoration with generative diffusion prior. In Aleš Leonardis, Elisa Ricci, Stefan Roth, Olga Russakovsky, Torsten Sattler, and Gül Varol (eds.), *Computer Vision – ECCV 2024*, pp. 430–448, Cham, 2025. Springer Nature Switzerland. ISBN 978-3-031-73202-7.

Guan-Horng Liu, Arash Vahdat, De-An Huang, Evangelos Theodorou, Weili Nie, and Anima Anandkumar. I^2SB: Image-to-image schrödinger bridge. In Andreas Krause, Emma Brunskill, Kyunghyun Cho, Barbara Engelhardt, Sivan Sabato, and Jonathan Scarlett (eds.), *Proceedings of the 40th International Conference on Machine Learning*, volume 202 of *Proceedings of Machine Learning Research*, pp. 22042–22062. PMLR, 23–29 Jul 2023a. URL https://proceedings.mlr.press/v202/liu23ai.html.

Guan-Horng Liu, Arash Vahdat, De-An Huang, Evangelos Theodorou, Weili Nie, and Anima Anandkumar. I^2SB: Image-to-image schrödinger bridge. In Andreas Krause, Emma Brunskill, Kyunghyun Cho, Barbara Engelhardt, Sivan Sabato, and Jonathan Scarlett (eds.), *Proceedings of the 40th International Conference on Machine Learning*, volume 202 of *Proceedings of Machine Learning Research*, pp. 22042–22062. PMLR, 23–29 Jul 2023b. URL https://proceedings.mlr.press/v202/liu23ai.html.

Ze Liu, Yutong Lin, Yue Cao, Han Hu, Yixuan Wei, Zheng Zhang, Stephen Lin, and Baining Guo. Swin transformer: Hierarchical vision transformer using shifted windows. In *2021 IEEE/CVF International Conference on Computer Vision (ICCV)*, pp. 9992–10002, 2021. doi: 10.1109/ICCV48922.2021.00986.

Ilya Loshchilov and Frank Hutter. Decoupled weight decay regularization. In *International Conference on Learning Representations*, 2019. URL https://openreview.net/forum?id=Bkg6RiCqY7.

Ziwei Luo, Fredrik K. Gustafsson, Zheng Zhao, Jens Sjölund, and Thomas B. Schön. Image restoration with mean-reverting stochastic differential equations. In Andreas Krause, Emma Brunskill, Kyunghyun Cho, Barbara Engelhardt, Sivan Sabato, and Jonathan Scarlett (eds.), *Proceedings of the 40th International Conference on Machine Learning*, volume 202 of *Proceedings of Machine Learning Research*, pp. 23045–23066. PMLR, 23–29 Jul 2023. URL https://proceedings.mlr.press/v202/luo23b.html.

Zhiyuan Ma, Yuxiang Wei, Yabin Zhang, Xiangyu Zhu, Zhen Lei, and Lei Zhang. Scaledreamer: Scalable text-to-3d synthesis with asynchronous score distillation. In Aleš Leonardis, Elisa Ricci, Stefan Roth, Olga Russakovsky, Torsten Sattler, and Gül Varol (eds.), *Computer Vision – ECCV 2024*, pp. 1–19, Cham, 2025. Springer Nature Switzerland. ISBN 978-3-031-72667-5.

Anish Mittal, Rajiv Soundararajan, and Alan C. Bovik. Making a "completely blind" image quality analyzer. *IEEE Signal Processing Letters*, 20(3):209–212, 2013. doi: 10.1109/LSP.2012.2227726.

Ben Poole, Ajay Jain, Jonathan T. Barron, and Ben Mildenhall. Dreamfusion: Text-to-3d using 2d diffusion. In *The Eleventh International Conference on Learning Representations*, 2023. URL https://openreview.net/forum?id=FjNys5c7VyY.

Robin Rombach, Andreas Blattmann, Dominik Lorenz, Patrick Esser, and Björn Ommer. High-resolution image synthesis with latent diffusion models. In *2022 IEEE/CVF Conference on Computer Vision and Pattern Recognition (CVPR)*, pp. 10674–10685, 2022. doi: 10.1109/CVPR52688.2022.01042.

Olaf Ronneberger, Philipp Fischer, and Thomas Brox. U-net: Convolutional networks for biomedical image segmentation. In *International Conference on Medical image computing and computer-assisted intervention*, pp. 234–241. Springer, 2015.

Chitwan Saharia, Jonathan Ho, William Chan, Tim Salimans, David J. Fleet, and Mohammad Norouzi. Image super-resolution via iterative refinement. *IEEE Transactions on Pattern Analysis and Machine Intelligence*, 45(4):4713–4726, 2023. doi: 10.1109/TPAMI.2022.3204461.

Axel Sauer, Dominik Lorenz, Andreas Blattmann, and Robin Rombach. Adversarial diffusion distillation. In Aleš Leonardis, Elisa Ricci, Stefan Roth, Olga Russakovsky, Torsten Sattler, and Gül Varol (eds.), *Computer Vision – ECCV 2024*, pp. 87–103, Cham, 2025. Springer Nature Switzerland. ISBN 978-3-031-73016-0.

Jascha Sohl-Dickstein, Eric Weiss, Niru Maheswaranathan, and Surya Ganguli. Deep unsupervised learning using nonequilibrium thermodynamics. In Francis Bach and David Blei (eds.), *Proceedings of the 32nd International Conference on Machine Learning*, volume 37 of *Proceedings of Machine Learning Research*, pp. 2256–2265, Lille, France, 07–09 Jul 2015. PMLR. URL https://proceedings.mlr.press/v37/sohl-dickstein15.html.

Yang Song and Prafulla Dhariwal. Improved techniques for training consistency models. In *The Twelfth International Conference on Learning Representations*, 2024. URL https://openreview.net/forum?id=WNzy9bRDvG.

Yang Song and Stefano Ermon. Generative modeling by estimating gradients of the data distribution. In H. Wallach, H. Larochelle, A. Beygelzimer, F. d'Alché-Buc, E. Fox, and R. Garnett (eds.), *Advances in Neural Information Processing Systems*, volume 32. Curran Associates, Inc., 2019.

Yang Song, Jascha Sohl-Dickstein, Diederik P Kingma, Abhishek Kumar, Stefano Ermon, and Ben Poole. Score-based generative modeling through stochastic differential equations. In *International Conference on Learning Representations*, 2021. URL https://openreview.net/forum?id=PxTIG12RRHS.

Yang Song, Prafulla Dhariwal, Mark Chen, and Ilya Sutskever. Consistency models. In Andreas Krause, Emma Brunskill, Kyunghyun Cho, Barbara Engelhardt, Sivan Sabato, and Jonathan Scarlett (eds.), *Proceedings of the 40th International Conference on Machine Learning*, volume 202 of *Proceedings of Machine Learning Research*, pp. 32211–32252. PMLR, 23–29 Jul 2023. URL https://proceedings.mlr.press/v202/song23a.html.

Lingchen Sun, Rongyuan Wu, Zhengqiang Zhang, Hongwei Yong, and Lei Zhang. Improving the stability of diffusion models for content consistent super-resolution. *arXiv preprint arXiv:2401.00877*, 2024.

Lingchen Sun, Rongyuan Wu, Zhiyuan Ma, Shuaizheng Liu, Qiaosi Yi, and Lei Zhang. Pixel-level and semantic-level adjustable super-resolution: A dual-lora approach. 2025.

Jianyi Wang, Kelvin C.K. Chan, and Chen Change Loy. Exploring clip for assessing the look and feel of images. *Proceedings of the AAAI Conference on Artificial Intelligence*, 37(2):2555–2563, Jun. 2023a. doi: 10.1609/aaai.v37i2.25353. URL https://ojs.aaai.org/index.php/AAAI/article/view/25353.

Jianyi Wang, Kelvin CK Chan, and Chen Change Loy. Exploring clip for assessing the look and feel of images. In *Proceedings of the AAAI conference on artificial intelligence*, volume 37, pp. 2555–2563, 2023b.

Jianyi Wang, Zongsheng Yue, Shangchen Zhou, Kelvin C.K. Chan, and Chen Change Loy. Exploiting diffusion prior for real-world image super-resolution. *International Journal of Computer Vision*, 2024a.

Xintao Wang, Ke Yu, Shixiang Wu, Jinjin Gu, Yihao Liu, Chao Dong, Yu Qiao, and Chen Change Loy. Esrgan: Enhanced super-resolution generative adversarial networks. In Laura Leal-Taixé and Stefan Roth (eds.), *Computer Vision – ECCV 2018 Workshops*, pp. 63–79, Cham, 2019. Springer International Publishing. ISBN 978-3-030-11021-5.

Xintao Wang, Liangbin Xie, Chao Dong, and Ying Shan. Real-esrgan: Training real-world blind super-resolution with pure synthetic data. In *2021 IEEE/CVF International Conference on Computer Vision Workshops (ICCVW)*, pp. 1905–1914, 2021. doi: 10.1109/ICCVW54120.2021.00217.

Yufei Wang, Wenhan Yang, Xinyuan Chen, Yaohui Wang, Lanqing Guo, Lap-Pui Chau, Ziwei Liu, Yu Qiao, Alex C. Kot, and Bihan Wen. Sinsr: Diffusion-based image super-resolution in a single step. In *2024 IEEE/CVF Conference on Computer Vision and Pattern Recognition (CVPR)*, pp. 25796–25805, 2024b. doi: 10.1109/CVPR52733.2024.02437.

Zhengyi Wang, Cheng Lu, Yikai Wang, Fan Bao, Chongxuan LI, Hang Su, and Jun Zhu. Prolificdreamer: High-fidelity and diverse text-to-3d generation with variational score distillation. In A. Oh, T. Naumann, A. Globerson, K. Saenko, M. Hardt, and S. Levine (eds.), *Advances in Neural Information Processing Systems*, volume 36, pp. 8406–8441. Curran Associates, Inc., 2023c.

Zhou Wang, A.C. Bovik, H.R. Sheikh, and E.P. Simoncelli. Image quality assessment: from error visibility to structural similarity. *IEEE Transactions on Image Processing*, 13(4):600–612, 2004. doi: 10.1109/TIP.2003.819861.

Pengxu Wei, Ziwei Xie, Hannan Lu, Zongyuan Zhan, Qixiang Ye, Wangmeng Zuo, and Liang Lin. Component divide-and-conquer for real-world image super-resolution. In Andrea Vedaldi, Horst Bischof, Thomas Brox, and Jan-Michael Frahm (eds.), *Computer Vision – ECCV 2020*, pp. 101–117, Cham, 2020. Springer International Publishing. ISBN 978-3-030-58598-3.

Rongyuan Wu, Lingchen Sun, Zhiyuan Ma, and Lei Zhang. One-step effective diffusion network for real-world image super-resolution. In A. Globerson, L. Mackey, D. Belgrave, A. Fan, U. Paquet, J. Tomczak, and C. Zhang (eds.), *Advances in Neural Information Processing Systems*, volume 37, pp. 92529–92553. Curran Associates, Inc., 2024a.

Rongyuan Wu, Tao Yang, Lingchen Sun, Zhengqiang Zhang, Shuai Li, and Lei Zhang. Seesr: Towards semantics-aware real-world image super-resolution. In *2024 IEEE/CVF Conference on Computer Vision and Pattern Recognition (CVPR)*, pp. 25456–25467, 2024b. doi: 10.1109/CVPR52733.2024.02405.

Rui Xie, Ying Tai, Kai Zhang, Zhenyu Zhang, Jun Zhou, and Jian Yang. Addsr: Accelerating diffusion-based blind super-resolution with adversarial diffusion distillation, 2024.

Sidi Yang, Tianhe Wu, Shuwei Shi, Shanshan Lao, Yuan Gong, Mingdeng Cao, Jiahao Wang, and Yujiu Yang. Maniqa: Multi-dimension attention network for no-reference image quality assessment. In *2022 IEEE/CVF Conference on Computer Vision and Pattern Recognition Workshops (CVPRW)*, pp. 1190–1199, 2022. doi: 10.1109/CVPRW56347.2022.00126.

Tao Yang, Rongyuan Wu, Peiran Ren, Xuansong Xie, and Lei Zhang. Pixel-aware stable diffusion for realistic image super-resolution and personalized stylization. In Aleš Leonardis, Elisa Ricci, Stefan Roth, Olga Russakovsky, Torsten Sattler, and Gül Varol (eds.), *Computer Vision – ECCV 2024*, pp. 74–91, Cham, 2025. Springer Nature Switzerland. ISBN 978-3-031-73247-8.

Tianwei Yin, Michaël Gharbi, Taesung Park, Richard Zhang, Eli Shechtman, Fredo Durand, and Bill Freeman. Improved distribution matching distillation for fast image synthesis. In A. Globerson, L. Mackey, D. Belgrave, A. Fan, U. Paquet, J. Tomczak, and C. Zhang (eds.), *Advances in Neural Information Processing Systems*, volume 37, pp. 47455–47487. Curran Associates, Inc., 2024a.

Tianwei Yin, Michaël Gharbi, Richard Zhang, Eli Shechtman, Frédo Durand, William T. Freeman, and Taesung Park. One-step diffusion with distribution matching distillation. In *2024 IEEE/CVF Conference on Computer Vision and Pattern Recognition (CVPR)*, pp. 6613–6623, 2024b. doi: 10.1109/CVPR52733.2024.00632.

Weiyi You, Mingyang Zhang, Leheng Zhang, Xingyu Zhou, Kexuan Shi, and Shuhang Gu. Consistency trajectory matching for one-step generative super-resolution. In *Proceedings of the IEEE/CVF International Conference on Computer Vision (ICCV)*, pp. 12747–12756, October 2025.

Fanghua Yu, Jinjin Gu, Zheyuan Li, Jinfan Hu, Xiangtao Kong, Xintao Wang, Jingwen He, Yu Qiao, and Chao Dong. Scaling up to excellence: Practicing model scaling for photo-realistic image restoration in the wild. In *2024 IEEE/CVF Conference on Computer Vision and Pattern Recognition (CVPR)*, pp. 25669–25680, 2024. doi: 10.1109/CVPR52733.2024.02425.

Zongsheng Yue, Jianyi Wang, and Chen Change Loy. Resshift: Efficient diffusion model for image super-resolution by residual shifting. In A. Oh, T. Naumann, A. Globerson, K. Saenko, M. Hardt, and S. Levine (eds.), *Advances in Neural Information Processing Systems*, volume 36, pp. 13294–13307. Curran Associates, Inc., 2023.

Zongsheng Yue, Kang Liao, and Chen Change Loy. Arbitrary-steps image super-resolution via diffusion inversion. In *Proceedings of the Computer Vision and Pattern Recognition Conference (CVPR)*, pp. 23153–23163, June 2025.

Kai Zhang, Jingyun Liang, Luc Van Gool, and Radu Timofte. Designing a practical degradation model for deep blind image super-resolution. In *2021 IEEE/CVF International Conference on Computer Vision (ICCV)*, pp. 4771–4780, 2021. doi: 10.1109/ICCV48922.2021.00475.

Lin Zhang, Lei Zhang, and Alan C Bovik. A feature-enriched completely blind image quality evaluator. *IEEE Transactions on Image Processing*, 24(8):2579–2591, 2015.

Lvmin Zhang, Anyi Rao, and Maneesh Agrawala. Adding conditional control to text-to-image diffusion models. In *2023 IEEE/CVF International Conference on Computer Vision (ICCV)*, pp. 3813–3824, 2023. doi: 10.1109/ICCV51070.2023.00355.

Richard Zhang, Phillip Isola, Alexei A. Efros, Eli Shechtman, and Oliver Wang. The unreasonable effectiveness of deep features as a perceptual metric. In *2018 IEEE/CVF Conference on Computer Vision and Pattern Recognition*, pp. 586–595, 2018. doi: 10.1109/CVPR.2018.00068.

Kaiwen Zheng, Guande He, Jianfei Chen, Fan Bao, and Jun Zhu. Diffusion bridge implicit models. *arXiv preprint arXiv:2405.15885*, 2024.

Mingyuan Zhou, Huangjie Zheng, Zhendong Wang, Mingzhang Yin, and Hai Huang. Score identity distillation: Exponentially fast distillation of pretrained diffusion models for one-step generation. In Ruslan Salakhutdinov, Zico Kolter, Katherine Heller, Adrian Weller, Nuria Oliver, Jonathan Scarlett, and Felix Berkenkamp (eds.), *Proceedings of the 41st International Conference on Machine Learning*, volume 235 of *Proceedings of Machine Learning Research*, pp. 62307–62331. PMLR, 21–27 Jul 2024. URL https://proceedings.mlr.press/v235/zhou24x.html.

A Appendix

We organize the structure of the appendix as follows:

1. Appendix A discusses the relation of RSD to relevant methods that involve training an aulixiary "fake" model - variational score distillation (VSD (Yin et al., 2024b; Wu et al., 2024a; Wang et al., 2023c)), score identity distillation (SiD (Zhou et al., 2024)), Flow Generator Matching (FGM (Huang et al., 2024)), and inverse bridge matching distillation (IBMD (Gushchin et al.,

2025)). Appendix A.1 includes the derivation of the variational score distillation for ResShift and its comparison with our RSD loss $\mathcal{L}_\theta$. Appendix A.2 discusses the relation of RSD to SiD and FGM. Appendix A.3 discusses the relation of RSD to IBMD and their quantitative comparison. In Appendix A.4, we also discuss the generalization of the RSD method for other diffusion models.

2. Appendix B details the implementation with the pseudocode of RSD and the notation used in the paper. We also present the pseudocode for ResShift-VSD, introduced in Appendix A

3. Appendix C consists of experimental details for the implementation of RSD and baselines.

4. Appendix D consists of full quantitative results including additional baselines and results on full-size DRealSR (Wei et al., 2020), RealLR200 (Wu et al., 2024b), RealLQ250 (Ai et al., 2024), and ImageNet-Test (Yue et al., 2023), which have not been shown in the main text due to space limitations.

5. Appendix E provides a comparison in performance and efficiency of RSD and state-of-the-art diffusion SR models: PiSA-SR (Sun et al., 2025), TSD-SR (Dong et al., 2025), AdcSR (Chen et al., 2025), CTMSR (You et al., 2025), InvSR (Yue et al., 2025) and CCSR (Sun et al., 2024).

6. Appendix F provides an additional discussion of ablation studies on hyperparameter K, training stability of RSD, and supervised losses.

7. Appendix G provides the quantitative comparison between RSD, SinSR and ResShift when all these models are trained on HR cropped images with resolution 512×512 from the LSDIR dataset (Li et al., 2023), which follows the training setup of OSEDiff (Wu et al., 2024a).

8. Appendix H discusses the qualitative and quantitative comparison between RSD and AddSR (Xie et al., 2024).

9. Appendix I includes additional details of ResShift theory, which have not been shown in the main text due to space limitations.

10. Appendix J discusses the limitations of RSD and failure cases.

11. Appendix K presents the proof of Proposition 3.1 and discusses the computational issues of the original problem in Equation (7).

12. Appendix L contains additional visual results for the comparison between RSD and baselines.

13. Appendix M describes the details of LLM usage in the paper and impact statement.

A Relation of RSD to VSD, SiD, FGM and IBMD

A.1 Derivation of VSD objective for ResShift (ResShift-VSD) and comparative analysis with our objective

In this section, our objective is to:

1. Derive the VSD loss in the ResShift framework to compare it with our distillation loss under the same experimental conditions (see Table 1 and Table 14);
2. Explain the main differences between our approach and the VSD loss.

To achieve this, we consider a generator G_θ with parameters θ and seek an update rule for them. We use a fake ResShift model to solve the following problem:

$$\arg\min_{f} \sum_{t=1}^{T} w_t \mathbb{E}_{p_\theta(\widehat{x}_0, y_0, x_t)} \big[\| f(x_t, y_0, t) - \widehat{x}_0 \|_2^2 \big], \tag{12}$$

Since it is the optimization with MSE function, the solution is given by the conditional expectation:

$$f_{G_\theta}(x_t, y_0, t) = \mathbb{E}_{p_\theta(\widehat{x}_0 | y_0, x_t)} [\widehat{x}_0] \tag{13}$$

Notation. Further we will use the following notation:

- f^* – teacher ResShift.

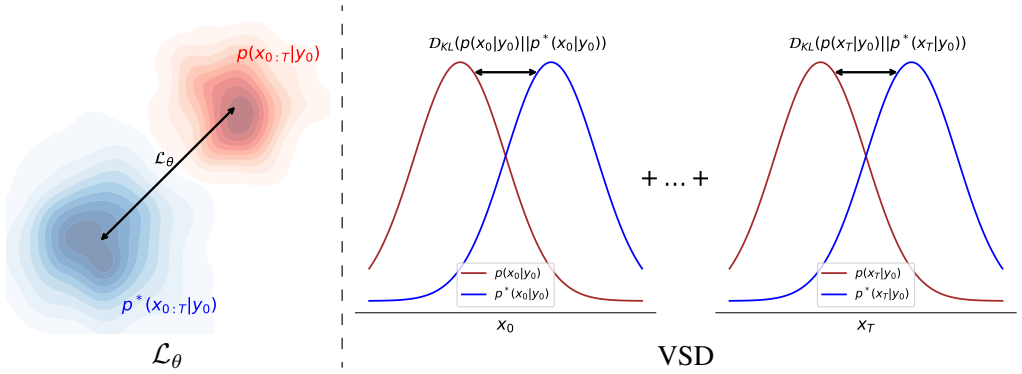

Figure 4: Illustration of the distinct distribution alignment strategies employed by the RSD $\mathcal{L}_\theta$ (**Ours**) and VSD loss functions. We denote by $p^*(x_{0:T}|y_0)$ reverse process of teacher ResShift model and by $p(x_{0:T}|y_0)$ reverse process of ResShift trained on generator G_θ data. The $\mathcal{L}_\theta$ loss enforces alignment of the joint distributions $p^*(x_{0:T}|y_0)$ and $p(x_{0:T}|y_0)$ across **all timesteps**, whereas the VSD loss aligns the marginal distributions at **each timestep** t **simultaneously** between distributions of teacher ResShift and ResShift trained on generator G_θ data. For formal derivations, see Equations (22) and (16).

- $x_{t_1:t_2} \stackrel{\text{def}}{=} (x_{t_1}, x_{t_1+1}, \ldots, x_{t_2})$ and $dx_{t_1:t_2} \stackrel{\text{def}}{=} \prod_{t=t_1}^{t_2} dx_t$ for any integer $t_1 < t_2$.
- The joint distribution across all timesteps is defined as follows:

$$p(x_{0:T}|y_0) \stackrel{\text{def}}{=} p(x_T|y_0) \prod_{t=1}^{T} p(x_{t-1}|x_t, y_0). \tag{14}$$

  The transition probabilities are determined using Equation (2) and Equation (4):

$$p(x_{t-1}|x_t, y_0) = \mathcal{N}\left(x_{t-1}|\frac{\eta_{t-1}}{\eta_t}x_t + \frac{\alpha_t}{\eta_t}f_{G_\theta}(x_t, y_0, t), \kappa^2\frac{\eta_{t-1}}{\eta_t}\alpha_t\mathbf{I}\right) \tag{15}$$

  In the same way we define $p^*(x_{0:T}|y_0) \stackrel{\text{def}}{=} p^*(x_T|y_0) \prod_{t=1}^{T} p^*(x_{t-1}|x_t, y_0)$, where the transition probabilities are determined using f^*.
- $p^*(x_t|y_0) \stackrel{\text{def}}{=} \int p^*(x_{0:T}|y_0)dx_{0:t-1}dx_{t+1:T}$ and $p(x_t|y_0) \stackrel{\text{def}}{=} \int p(x_{0:T}|y_0)dx_{0:t-1}dx_{t+1:T}$ are marginal distributions.

Derivation of the VSD loss for ResShift (ResShift-VSD). Initially, the main objective of the VSD loss (Yin et al., 2024b; Wu et al., 2024a; Wang et al., 2023c) is:

$$\mathcal{L}_{\text{VSD}} = \mathbb{E}_{p(y_0)}\Big[\sum_{t=1}^{T} w_t \mathcal{D}_{\text{KL}}\Big(p(x_t|y_0)||p^*(x_t|y_0)\Big)\Big] \tag{16}$$

We can get another expression for this loss using the reparametrization based on Equation (38):

$$\mathcal{L}_{\text{VSD}} = \sum_{t=1}^{T} w_t \mathbb{E}_{p(y_0)}\Big[\mathcal{D}_{\text{KL}}\Big(p(x_t|y_0)||p^*(x_t|y_0)\Big)\Big] = \sum_{t=1}^{T} w_t \mathbb{E}_{p(y_0)p(x_t|y_0)} \log\frac{p(x_t|y_0)}{p^*(x_t|y_0)} =$$
$$\sum_{t=1}^{T} w_t \mathbb{E}_{p(y_0)} \mathop{\mathbb{E}}_{\substack{x_t=(1-\eta_t)\widehat{x}_0+\eta_t y_0+\kappa^2\eta_t\epsilon' \\ \widehat{x}_0=G_\theta(y_0,\epsilon) \\ \epsilon',\epsilon\sim\mathcal{N}(0;\mathbf{I})}} \log\frac{p(x_t|y_0)}{p^*(x_t|y_0)} \tag{17}$$

Initially, this loss is intractable because it requires computing probability densities, which are not available in practice. However, taking the gradient with chain rule facilitates its computation:

$$\nabla_\theta \mathcal{L}_{\text{VSD}} =$$
$$-\sum_{t=1}^{T} w_t \mathbb{E}_{p(y_0)} \mathop{\mathbb{E}}_{\substack{x_t=(1-\eta_t)\widehat{x}_0+\eta_t y_0+\kappa^2\eta_t\epsilon' \\ \widehat{x}_0=G_\theta(y_0,\epsilon) \\ \epsilon',\epsilon\sim\mathcal{N}(0;\mathbf{I})}} \left[(\nabla_{x_t} \log p^*(x_t|y_0) - \nabla_{x_t} \log p(x_t|y_0)) \frac{dx_t}{d\theta} \right] =$$
$$-\sum_{t=1}^{T} w_t \mathbb{E}_{p(y_0)} \mathop{\mathbb{E}}_{\substack{x_t=(1-\eta_t)\widehat{x}_0+\eta_t y_0+\kappa^2\eta_t\epsilon' \\ \widehat{x}_0=G_\theta(y_0,\epsilon) \\ \epsilon',\epsilon\sim\mathcal{N}(0;\mathbf{I})}} \left[(\nabla_{x_t} \log p^*(x_t|y_0) - \nabla_{x_t} \log p(x_t|y_0)) \frac{dx_t}{d\widehat{x}_0} \frac{d\widehat{x}_0}{d\theta} \right] =$$
$$-\sum_{t=1}^{T} w'_t \mathbb{E}_{p(y_0)} \mathop{\mathbb{E}}_{\substack{x_t=(1-\eta_t)\widehat{x}_0+\eta_t y_0+\kappa^2\eta_t\epsilon' \\ \widehat{x}_0=G_\theta(y_0,\epsilon) \\ \epsilon',\epsilon\sim\mathcal{N}(0;\mathbf{I})}} \left[(\nabla_{x_t} \log p^*(x_t|y_0) - \nabla_{x_t} \log p(x_t|y_0)) \frac{d\widehat{x}_0}{d\theta} \right], \quad (18)$$

where $w'_t \stackrel{\text{def}}{=} w_t \frac{dx_t}{d\widehat{x}_0} = w_t(1-\eta_t)$.

The expression $\nabla_{x_t} \log p(x_t|y_0)$ can be utilized as follows (Zheng et al., 2024):

$$\nabla_{x_t} \log p(x_t|y_0) = \frac{\nabla_{x_t} p(x_t|y_0)}{p(x_t|y_0)} = \frac{\nabla_{x_t} \int q(x_t|y_0,x_0) p(x_0|y_0) dx_0}{p(x_t|y_0)} =$$
$$\frac{\int p(x_0|y_0) \nabla_{x_t} q(x_t|y_0,x_0) dx_0}{p(x_t|y_0)} = \frac{\int p(x_0|y_0) q(x_t|y_0,x_0) \nabla_{x_t} \log q(x_t|y_0,x_0) dx_0}{p(x_t|y_0)} =$$
$$\int \frac{p(x_0|y_0) q(x_t|y_0,x_0)}{p(x_t|y_0)} \nabla_{x_t} \log q(x_t|y_0,x_0) dx_0 = \int p(x_0|x_t,y_0) \nabla_{x_t} \log q(x_t|y_0,x_0) dx_0$$
$$= \mathop{\mathbb{E}}_{p(x_0|x_t,y_0)} \Big[\nabla_{x_t} \log q(x_t|y_0,x_0) \Big] \quad (19)$$

Since $q(x_t|y_0,x_0) = \mathcal{N}(x_t|x_0+\eta_t e_0, \kappa^2\eta_t \mathbf{I})$ (see Equation (38)), we get:

$$\nabla_{x_t} \log p(x_t|y_0) = -\mathop{\mathbb{E}}_{p(x_0|x_t,t,y_0)} \Big[\frac{x_t - \eta_t y_0 - (1-\eta_t)x_0}{\kappa^2\eta_t} \Big], \quad (20)$$

which leads to:

$$\nabla_\theta \mathcal{L}_{\text{VSD}} = -\sum_{t=1}^{T} w''_t \mathbb{E}_{p(y_0)} \mathop{\mathbb{E}}_{\substack{x_t=(1-\eta_t)\widehat{x}_0+\eta_t y_0+\kappa^2\eta_t\epsilon' \\ \widehat{x}_0=G_\theta(y_0,\epsilon) \\ \epsilon',\epsilon\sim\mathcal{N}(0;\mathbf{I})}} \left[(f^*(x_t,y_0,t) - f_{G_\theta}(x_t,y_0,t)) \frac{d\widehat{x}_0}{d\theta} \right] \quad (21)$$

where $w''_t \stackrel{\text{def}}{=} w'_t \frac{1-\eta_t}{\kappa^2\eta_t}$. As a result, this loss can be implemented to match the gradients with $\nabla_\theta \mathcal{L}_{\text{VSD}}$ (see Algorithm 2). We call this model ResShift-VSD.

Reformulation of our $\mathcal{L}_\theta$ loss. We can express our RSD loss function as follows:

$$\mathcal{L}_\theta = \mathbb{E}_{p(y_0)} \Big[\mathcal{D}_{\text{KL}} \Big(p(x_{0:T}|y_0) \,\|\, p^*(x_{0:T}|y_0) \Big) \Big], \quad (22)$$

Recalling that the joint probability distribution can be factorized (see Equation (14)), the above loss can be decomposed as:

$$\mathcal{L}_\theta = \mathbb{E}_{p(y_0)} \Big[\mathcal{D}_{\text{KL}} \Big(p(x_{0:T}|y_0) \,\|\, p^*(x_{0:T}|y_0) \Big) \Big] =$$
$$\mathbb{E}_{p(y_0)} \Big[\underbrace{\mathcal{D}_{\text{KL}} \Big(p(x_T|y_0) \,\|\, p^*(x_T|y_0) \Big)}_{=0 \text{ since } p(x_T|y_0)=p^*(x_T|y_0) \text{ from Equation (38)}} \Big] +$$
$$\mathbb{E}_{p(y_0)} \Big[\sum_{t=1}^{T} \mathbb{E}_{p(x_t|y_0)} \mathcal{D}_{\text{KL}} \Big(p(x_{t-1}|x_t,y_0) \,\|\, p^*(x_{t-1}|x_t,y_0) \Big) \Big] \quad (23)$$

Using Equation (15), the KL divergence inside the expectation reduces to the KL divergence between Gaussian distributions, which can be computed in closed form. Consequently, we obtain the following:

$$\begin{aligned}\mathcal{L}_\theta &= \sum_{t=1}^{T} \mathbb{E}_{p(y_0)} \mathbb{E}_{p(x_t|y_0)} \mathcal{D}_{\mathrm{KL}} \Big(p(x_{t-1}|x_t, y_0) \,\|\, p^*(x_{t-1}|x_t, y_0) \Big) \\ &= \sum_{t=1}^{T} \mathbb{E}_{p(y_0)} \mathbb{E}_{p(x_t|y_0)} \underbrace{\frac{1}{2\kappa^2} \frac{\alpha_t}{\eta_t \eta_{t-1}}}_{\stackrel{\text{def}}{=} w_t} \| f_{G_\theta}(x_t, y_0, t) - f^*(x_t, y_0, t) \|_2^2 \\ &= \sum_{t=1}^{T} w_t \mathbb{E}_{p(y_0)} \mathbb{E}_{p(x_t|y_0)} \| f_{G_\theta}(x_t, y_0, t) - f^*(x_t, y_0, t) \|_2^2 \end{aligned} \tag{24}$$

Since the distribution $p(x_t|y_0)$ is generally intractable, we instead use the tractable distribution $q(x_t|\widehat{x}_0, y_0)$, which is known to satisfy $q(x_t|\widehat{x}_0, y_0) = p(x_t|y_0)$. Thus, we have:

$$\mathcal{L}_\theta = \sum_{t=1}^{T} w_t \mathbb{E}_{p(y_0)} \mathbb{E}_{q(x_t|\widehat{x}_0, y_0)} \| f_{G_\theta}(x_t, y_0, t) - f^*(x_t, y_0, t) \|_2^2 \tag{25}$$

Noting that the integrand is independent of $\widehat{x}_0$ and we can use $p_\theta(\widehat{x}_0, y_0)$ instead of $p(y_0)$, since $\int p_\theta(\widehat{x}_0|y_0) d\widehat{x}_0 = 1$, and therefore we obtain the following:

$$\mathcal{L}_\theta = \sum_{t=1}^{T} w_t \mathbb{E}_{q(x_t|\widehat{x}_0, y_0)\, p_\theta(\widehat{x}_0, y_0)} \| f_{G_\theta}(x_t, y_0, t) - f^*(x_t, y_0, t) \|_2^2 \tag{26}$$

Finally, recognizing that the joint distribution $p_\theta(\widehat{x}_0, y_0, x_t)$ is defined as

$$p_\theta(\widehat{x}_0, y_0, x_t) \stackrel{\text{def}}{=} q(x_t|\widehat{x}_0, y_0)\, p_\theta(\widehat{x}_0, y_0),$$

we arrive at the final form of the RSD loss:

$$\mathcal{L}_\theta = \sum_{t=1}^{T} w_t \mathbb{E}_{p_\theta(\widehat{x}_0, y_0, x_t)} \| f_{G_\theta}(x_t, y_0, t) - f^*(x_t, y_0, t) \|_2^2 \tag{27}$$

This derivation demonstrates that the loss function in Equation (22) reconstructs the initial objective presented in Equation (7).

Conceptual comparison of VSD and our RSD $\mathcal{L}_\theta$ losses. The key difference between VSD and $\mathcal{L}_\theta$ losses lies in how they match distributions. For a more clear intuitive explanation one can see formulations of losses with $\mathcal{D}_{\mathrm{KL}}$ for VSD (Equation (16)) and $\mathcal{L}_\theta$ (Equation (22)). The VSD loss aligns the marginal distributions at each timestep t between the teacher's and fake's distributions. In contrast, the $\mathcal{L}_\theta$ loss matches the joint distribution in all timesteps. This difference is illustrated in Figure 4, where the $\mathcal{L}_\theta$ loss enforces joint distribution alignment, while the VSD loss aligns the marginal distributions separately and then sums them.

The RSD loss is superior to the VSD loss for the SR problem because it aligns the joint distribution across all timesteps, ensuring a more holistic match between teacher and student models. Unlike VSD, which aligns marginal distributions at each timestep separately, RSD captures temporal dependencies more effectively. This joint alignment is particularly beneficial for SR tasks, where maintaining consistency and accuracy across all image details and features is crucial to high-quality resolution. The loss of RSD, which considers the entire distribution in multiple timesteps, leads to more precise and stable SR performance, as we validated in Section 4.2.

Computational analysis of VSD and $\mathcal{L}_\theta$ losses. As was shown in Proposition 3.1, our loss can be evaluated via:

$$\begin{aligned}\mathcal{L}_\theta = -\min_{\phi} \Big\{ \sum_{t=1}^{T} w_t \mathbb{E}_{p_\theta(\widehat{x}_0, x_t, y_0)} \Big[&\| f_\phi(x_t, y_0, t) \|_2^2 - \| f^*(x_t, y_0, t) \|_2^2 + \\ &2 \langle f^*(x_t, y_0, t) - f_\phi(x_t, y_0, t), \widehat{x}_0 \rangle \Big] \Big\}\end{aligned} \tag{28}$$

Using Equation (13) we can rewrite it and make reparameterization:

$$\mathcal{L}_\theta = -\sum_{t=1}^{T} w_t \mathbb{E}_{p_\theta(\widehat{x}_0, x_t, y_0)} \Big[\|f_{G_\theta}(x_t, y_0, t)\|_2^2 - \|f^*(x_t, y_0, t)\|_2^2 + 2\langle f^*(x_t, y_0, t) - f_{G_\theta}(x_t, y_0, t), \widehat{x}_0 \rangle \Big] =$$
$$-\sum_{t=1}^{T} w_t \mathop{\mathbb{E}}_{\substack{x_t=(1-\eta_t)\widehat{x}_0+\eta_t y_0+\kappa^2\eta_t\epsilon' \\ \widehat{x}_0=G_\theta(y_0,\epsilon) \\ \epsilon',\epsilon\sim\mathcal{N}(0;\mathbf{I})}} \Big[\|f_{G_\theta}(x_t, y_0, t)\|_2^2 - \|f^*(x_t, y_0, t)\|_2^2 + 2\langle f^*(x_t, y_0, t) - f_{G_\theta}(x_t, y_0, t), \widehat{x}_0 \rangle \Big] \tag{29}$$

To compare it with the VSD loss, we can take the gradient of $\mathcal{L}_\theta$ loss and get:

$$\frac{d\mathcal{L}_\theta}{d\theta} = -\sum_{t=1}^{T} w_t \mathop{\mathbb{E}}_{\substack{x_t=(1-\eta_t)\widehat{x}_0+\eta_t y_0+\kappa^2\eta_t\epsilon' \\ \widehat{x}_0=G_\theta(y_0,\epsilon) \\ \epsilon',\epsilon\sim\mathcal{N}(0;\mathbf{I})}} \Big[\frac{d\|f_{G_\theta}(x_t, y_0, t)\|_2^2}{d\theta} - \frac{d\|f^*(x_t, y_0, t)\|_2^2}{d\theta} + 2\langle \frac{df^*(x_t, y_0, t)}{d\theta} - \frac{df_{G_\theta}(x_t, y_0, t)}{d\theta}, \widehat{x}_0 \rangle + 2\langle f^*(x_t, y_0, t) - f_{G_\theta}(x_t, y_0, t), \frac{d\widehat{x}_0}{d\theta} \rangle \Big] =$$
$$-\sum_{t=1}^{T} w_t \mathop{\mathbb{E}}_{\substack{x_t=(1-\eta_t)\widehat{x}_0+\eta_t y_0+\kappa^2\eta_t\epsilon' \\ \widehat{x}_0=G_\theta(y_0,\epsilon) \\ \epsilon',\epsilon\sim\mathcal{N}(0;\mathbf{I})}} \Big[\frac{d\|f_{G_\theta}(x_t, y_0, t)\|_2^2}{d\theta} - \frac{d\|f^*(x_t, y_0, t)\|_2^2}{d\theta} + 2\langle \frac{df^*(x_t, y_0, t)}{d\theta} - \frac{df_{G_\theta}(x_t, y_0, t)}{d\theta}, \widehat{x}_0 \rangle \Big]$$
$$\underbrace{-\sum_{t=1}^{T} w_t \mathop{\mathbb{E}}_{\substack{x_t=(1-\eta_t)\widehat{x}_0+\eta_t y_0+\kappa^2\eta_t\epsilon' \\ \widehat{x}_0=G_\theta(y_0,\epsilon) \\ \epsilon',\epsilon\sim\mathcal{N}(0;\mathbf{I})}} \Big[2\langle f^*(x_t, y_0, t) - f_{G_\theta}(x_t, y_0, t), \frac{d\widehat{x}_0}{d\theta} \rangle \Big]}_{=2\cdot\nabla_\theta\mathcal{L}_{\text{VSD}} \text{ up to weighting term } w_t \text{ (see Equation(21))}} \tag{30}$$

Consequently, the gradients of our RSD $\mathcal{L}_\theta$ loss function encompass those of VSD loss, scaled by a constant factor of 2 and modulated by the time-dependent weighting term w_t. These scaling factors do not affect the optimal solution of the loss. However, $\mathcal{L}_\theta$ additionally incorporates gradient contributions from both the teacher and fake models. To reduce $\mathcal{L}_\theta$ to the standard VSD formulation, the application of a stop-gradient operator is required to suppress the influence of these auxiliary gradient terms. For a detailed implementation, refer to Algorithm 2.

A.2 Relation of RSD to SiD and FGM

The loss function $\mathcal{L}_\theta$ in Equation (8) can be reformulated as follows:

$$
\begin{aligned}
&\mathcal{L}_\theta = \max_\phi \Big\{ \sum_{t=1}^{T} w_t \mathbb{E}_{p_\theta(\widehat{x}_0, y_0, x_t)} \Big(\|f^*(x_t, y_0, t)\|_2^2 - \|f_\phi(x_t, y_0, t)\|_2^2 + \\
&2\langle f_\phi(x_t, y_0, t) - f^*(x_t, y_0, t), \widehat{x}_0 \rangle \Big) \Big\} \\
&= \max_\phi \Big\{ \sum_{t=1}^{T} w_t \mathbb{E}_{p_\theta(\widehat{x}_0, y_0, x_t)} \Big(\|f^*(x_t, y_0, t)\|_2^2 - \|f_\phi(x_t, y_0, t)\|_2^2 + \\
&2\langle f_\phi(x_t, y_0, t) - f^*(x_t, y_0, t), \widehat{x}_0 \rangle \pm 2\langle f^*(x_t, y_0, t), f_\phi(x_t, y_0, t) \rangle \pm \|f_\phi(x_t, y_0, t)\|_2^2 \Big) \Big\} \\
&= \max_\phi \Big\{ \sum_{t=1}^{T} w_t \mathbb{E}_{p_\theta(\widehat{x}_0, y_0, x_t)} \Big(\|f^*(x_t, y_0, t) - f_\phi(x_t, y_0, t)\|_2^2 + \\
&2\langle f^*(x_t, y_0, t) - f_\phi(x_t, y_0, t), f_\phi(x_t, y_0, t) \rangle + 2\langle f_\phi(x_t, y_0, t) - f^*(x_t, y_0, t), \widehat{x}_0 \rangle \Big) \Big\} \\
&= \max_\phi \Big\{ \sum_{t=1}^{T} w_t \mathbb{E}_{p_\theta(\widehat{x}_0, y_0, x_t)} \Big(\|f^*(x_t, y_0, t) - f_\phi(x_t, y_0, t)\|_2^2 + \\
&2\langle f^*(x_t, y_0, t) - f_\phi(x_t, y_0, t), f_\phi(x_t, y_0, t) - \widehat{x}_0 \rangle \Big) \Big\}
\end{aligned}
\tag{31}
$$

One can see that our objective can be reformulated in a manner similar to the formulations used in SiD (Zhou et al., 2024, Equation 23 with $\alpha = 0.5$) and FGM (Huang et al., 2024, Equations 4.11–4.12) with up to time weighting w_t. However, in both SiD (where $\alpha = 1.0, 1.2$ were used in the experiments) and FGM, the authors either omitted the quadratic term or assigned it a negative coefficient in the image experiments due to numerical instabilities. In contrast to these approaches, we retain the complete original loss formulation as prescribed by theory, without discarding or modifying any of its components.

Furthermore, it is important to emphasize that SiD and FGM were primarily developed for image generation tasks, whereas our proposed RSD framework is specifically tailored for image restoration, with a focus on reconstructing high-resolution images from their low-resolution counterparts. To this end, we adopt a dedicated ResShift architecture that integrates both VAE and U-Net components, along with a diffusion process specifically designed for the super-resolution task. Additionally, we incorporate supervised loss terms tailored to the super-resolution objective (see Section 3.5). These task-specific design choices are in contrast to SiD and FGM, which lack such adaptations for image restoration scenarios.

A.3 Relation of RSD to IBMD

In this section, we compare qualitatively and quantitatively the RSD and IBMD (Gushchin et al., 2025) methods for the Real-ISR problem. Our goal is to support the practical contribution of RSD superiority for this problem, which was claimed in Section 1.

Conceptual comparison. The loss function $\mathcal{L}_\theta$ in Equation (8) can be equivalently reformulated as follows:

$$\begin{aligned}
\mathcal{L}_\theta &= \max_\phi \Big\{ \sum_{t=1}^{T} w_t \mathbb{E}_{p_\theta(\widehat{x}_0, y_0, x_t)} \Big(\|f^*(x_t, y_0, t)\|_2^2 - \|f_\phi(x_t, y_0, t)\|_2^2 + \\
&2\langle f_\phi(x_t, y_0, t) - f^*(x_t, y_0, t), \widehat{x}_0 \rangle \Big) \Big\} \\
&= \max_\phi \Big\{ \sum_{t=1}^{T} w_t \mathbb{E}_{p_\theta(\widehat{x}_0, y_0, x_t)} \Big(\|f^*(x_t, y_0, t)\|_2^2 - \|f_\phi(x_t, y_0, t)\|_2^2 + \\
&2\langle f_\phi(x_t, y_0, t), \widehat{x}_0 \rangle - 2\langle f^*(x_t, y_0, t), \widehat{x}_0 \rangle \pm \|\widehat{x}_0\|_2^2 \Big) \Big\} \\
&= \max_\phi \Big\{ \sum_{t=1}^{T} w_t \mathbb{E}_{p_\theta(\widehat{x}_0, y_0, x_t)} \Big(\|f^*(x_t, y_0, t) - \widehat{x}_0\|_2^2 - \|f_\phi(x_t, y_0, t) - \widehat{x}_0\|_2^2 \Big) \Big\}
\end{aligned} \tag{32}$$

It should be noted that our RSD loss, denoted by $\mathcal{L}_\theta$, can be interpreted as a discrete variant of the inverse bridge matching distillation (IBMD) loss (Gushchin et al., 2025, Equation 10), originally proposed for conditional Bridge Matching models. From a theoretical perspective, one of our main contributions is the development of a discretized form of the IBMD-conditional loss, which can offer practical benefits for complex tasks such as the Real-ISR problem.

Although the IBMD framework has been applied to a broad range of problems, including image restoration, its experimental setup relied on relatively simplistic degradation processes, such as bicubic and pool. In contrast, we have tailored our objective specifically for image restoration by integrating it into the ResShift paradigm, incorporating additional supervised losses explicitly designed for real-world super-resolution (see Section 3.5), and utilizing a more challenging and realistic degradation model based on Real-ESRGAN. We also note that ResShift and RSD use VAE and a diffusion process in the latent space, while IBMD operates in the pixel space, which makes RSD more efficient and scalable for handling images of varying resolutions due to the reduced computational complexity and memory requirements in the latent domain. Another relevant difference between IBMD and ResShift implementations for the SR problem is the larger architecture of IBMD. IBMD for super-resolution uses the ADM architecture (Dhariwal & Nichol, 2021) following the I2SB (Liu et al., 2023b) with 552M parameters, while RSD follows the ResShift architecture with 174M parameters.

Quantitative comparison. Thus, in addition to our theoretical contribution, we extend the implementation of the IBMD loss to more severe and practically relevant degradation settings. These task-specific modifications differentiate our approach from the original IBMD formulation, which does not account for such adaptations in the context of real-world image restoration scenarios. To support this claim quantitatively and qualitatively, we conducted the following numerical experiments to show that both the teacher model of I2SB and the distilled student model of IBMD do not provide sufficient perceptual quality in Real-ISR problems compared to ResShift and RSD, respectively.

Step 1: training the I2SB teacher using Real-ESRGAN degradations. For a fair comparison with ResShift, we trained an I2SB model on ImageNet using Real-ESRGAN degradations following the training setup of ResShift and RSD detailed in Section 4.1. The model was trained using the same hyperparameters as the original I2SB model trained on bicubic degradations with 4000 iterations. We used the official I2SB implementation published in the respective GitHub repository, which is provided by the I2SB authors:

`https://github.com/NVlabs/I2SB`

Step 2: distillation of I2SB with IBMD. We used the official IBMD implementation published in the respective GitHub repository, which is provided by the IBMD authors:

`https://github.com/ngushchin/IBMD`

We adapt the provided implementation with the replacement of Real-ESRGAN degradations instead of original bicubic degradations and use the same hyperparameters, which were used for the training of IBMD model for bicubic degradations (first line in Table 7 of IBMD). We distill the trained I2SB

Table 6: Comparison on ImageNet-Test between I2SB (Liu et al., 2023b), ResShift (Yue et al., 2023), and their 1-step distillation versions, IBMD (Gushchin et al., 2025) and RSD, respectively. The best and second best results are highlighted in **bold** and underline.

Methods	Distillation model	NFE	PSNR↑	SSIM↑	LPIPS↓	CLIPIQA↑	MUSIQ↑
I2SB (Liu et al., 2023a)	No	15	24.80	0.663	0.302	0.444	49.584
I2SB (Liu et al., 2023a)	No	1	**25.52**	**0.690**	0.412	0.405	34.439
ResShift (Yue et al., 2023)	No	15	<u>25.01</u>	<u>0.677</u>	0.231	0.592	53.660
IBMD (Gushchin et al., 2025)	Yes	1	23.91	0.619	0.284	0.505	54.667
RSD (**Ours**, distill only)	Yes	1	23.97	0.643	<u>0.217</u>	<u>0.660</u>	<u>57.831</u>
RSD (**Ours**)	Yes	1	24.31	0.657	**0.193**	**0.681**	**58.947**

Table 7: Training and inference complexity between RSD and IBMD (Gushchin et al., 2025). All methods are tested with an LR image of size 64×64 for SR factor $\times 4$, and the inference is done on an NVIDIA A100 GPU. The best values are highlighted in **bold**.

Methods	RSD (**Ours**)	IBMD
Inference Step (NFE)	**1**	**1**
Inference Time (s)	**0.059**	0.077
# Total Param (M)	**174**	553
Maximum GPU memory (MB)	**539**	4676
Training time (hours / # GPU)	**5 / 4 A100**	23 / 8 A100

teacher with Real-ESRGAN degradations using IBMD method into a one-step student model with 1500 gradient updates for the student model. We found that this number of gradient updates is enough for the convergence of IBMD validation metrics on the ImageNet-Test dataset (Yue et al., 2023), which was used for the evaluation of ResShift (Yue et al., 2023, Table 3), SinSR (Wang et al., 2024b, Table 2), and CTMSR (You et al., 2025, Table 1).

For a fair comparison with ResShift and RSD, we evaluated the trained teacher I2SB with NFE = 15 and 1 and the trained IBMD student with NFE = 1, which follows the inference NFE of ResShift and RSD, respectively. We report on the results of their evaluation on the ImageNet-Test dataset, which follows the RSD, ResShift, and SinSR evaluation setup reported in Table 14, and compare them with ResShift, RSD with supervised losses (RSD (**Ours**)), and RSD with only distillation loss (RSD (**Ours**, distill only)) in Table 6. We also extend the complexity comparison in our Table 3 of RSD with IBMD by providing the training time of both methods in Table 7.

Comparison between teachers, I2SB and ResShift. ResShift achieves better results on the ImageNet dataset with complex Real-ESRGAN degradations compared to I2SB **in all evaluation metrics** (PSNR, SSIM, LPIPS, MUSIQ, CLIPIQA) with a great improvement in perceptual metrics (LPIPS, MUSIQ, CLIPIQA) using the same NFE = 15. Our results in Table 6 are consistent with the analysis for comparison between ResShift and I2SB on simpler bicubic degradations, which is given in Appendix B.2 of ResShift. The same conclusion is quantitatively validated in Table 5 and visually supported in Figure 8 of ResShift, respectively. The results of Table 5 in ResShift also show a significant improvement in terms of perceptual quality for ResShift compared to I2SB for bicubic degradations with the same NFE = 15. We explain these results by the specific design of ResShift, which applies the diffusion process in discrete time in the latent space of VAE and uses the non-uniform geometric noise schedule (Section 2 in ResShift).

Comparison between students, IBMD and RSD. For a fair comparison, we compare our RSD model without supervised losses and the IBMD model, because IBMD originally is a data-free distillation method (see contribution 3 in IBMD). The results show that RSD is better in **all evaluation metrics even without supervised losses** (PSNR, SSIM, LPIPS, MUSIQ, CLIPIQA) with a significant improvement in perceptual metrics (LPIPS, MUSIQ, CLIPIQA). The addition of supervised losses in RSD even more increases the margin between all evaluation metrics. In practice, we also found that the IBMD model requires a significant computational budget, which is in line with the complexity reported in Table 9 of IBMD. We trained the IBMD model on 8 A100 for 23 hours, which is > 4 times more than the training time of RSD. IBMD also has > 3 times bigger the number of parameters and > 8 times bigger the required GPU memory for inference.

Summary. For a quantitative comparison, the RSD model without supervised losses outperforms the IBMD model in all evaluation metrics. For a computational comparison, the RSD model has a much faster distillation training time, requires fewer parameters, GPU memory, and has a faster generation time during inference compared to IBMD. Thus, task-specific features of RSD used for Real-ISR problems are essential for high perceptual quality compared to the diffusion distillation method of IBMD, which is developed for general image-to-image translation problems. It supports our claim in practical contributions in Section 1. We also visually observed that HR predictions for both I2SB and its IBMD distillation models struggle with severe blur artifacts, which explains low perceptual metrics (LPIPS, CLIPIQA, MUSIQ) and support higher fidelity metrics of PSNR and SSIM for I2SB. Due to the limitations of the file size of the submission, we do not provide visual results for Table 6 since Figure 8 of ResShift already shows the superiority of ResShift compared to I2SB for the SR problem.

A.4 Generalization of RSD to other methods.

It should be noted that the proof of Proposition 3.1 (see Appendix K), as well as the formulation of our loss function, does not rely on a specific form of processes used in the ResShift model. The only difference from other approaches is how they sample the joint distribution $p_\theta(\widehat{x}_0, y_0, x_t)$ during the training procedure. Usually, $p_\theta(\widehat{x}_0, y_0, x_t)$ is written in the following way:

$$p_\theta(\widehat{x}_0, y_0, x_t) = q(x_t \mid \widehat{x}_0, y_0) p_\theta(\widehat{x}_0 \mid y_0) p(y_0), \tag{33}$$

which show that the only thing that is different for each method is the used distribution q. Thus, to adopt our approach to other processes, one only needs to change the distribution q. For example, to train I2SB or LDM models using the RSD formulation, one can use their discrete formulations for both models (Liu et al., 2023a, Equation 11) in I2SB or (Rombach et al., 2022, Equation 4) in LDM and plug them into $\mathcal{L}_\theta$.

B ALGORITHMS OF RSD, RESSHIFT-RSD AND USED NOTATION

The pseudocode for our RSD training algorithm is presented in Algorithm 1.

Algorithm 1: Residual Shifting Distillation (RSD).

Input:
Training dataset $p_{\text{data}}(x_0, y_0)$;
Pretrained ResShift Teacher model f^*; frozen encoder and decoder of VAE: Enc, Dec;
Number of fake ResShift (f_ϕ) training iterations K, f_ϕ^{encoder} - encoder part of fake ResShift model;

Output:
A trained generator G_θ;

func SampleEverything()
  Sample $(x_0, y_0) \sim p_{\text{data}}(x_0, y_0)$
  $z_y \leftarrow \text{Enc}(\text{upsample}(y_0))$; $z_0 \leftarrow \text{Enc}(x_0)$
  Sample $t_n \sim \mathcal{U}\{1, \dots, T\}$, $z_{t_n} \sim q(z_{t_n}|z_0, z_y)$, $\epsilon \sim \mathcal{N}(0, \mathbf{I})$ // Eq. (38)
  $\widehat{z}_0^{t_n} \leftarrow G_\theta(z_{t_n}, y_0, t_n, \epsilon)$
  Sample $t \sim \mathcal{U}\{1, \dots, T\}$, $z_t \sim q(z_t|\widehat{z}_0^{t_n}, z_y)$ // Eq. (38)
  return $(x_0, y_0, z_0, z_y, t_n, z_{t_n}, \widehat{z}_0^{t_n}, t, z_t)$

// Initialize generator from pretrained model
// Initalize fake ResShift from pretrained model and GAN discriminator head randomly
$G_\theta \leftarrow \text{copyWeightsAndUnfreeze}(f^*)$;
$f_\phi \leftarrow \text{copyWeightsAndUnfreezeAndAddNoiseChannels}(f^*)$ // See Appendix C
$\text{D}_\psi \leftarrow \text{randomInitOfDiscriminatorHead}()$

while *train* **do**
  // Train fake ResShift model
  for $k \leftarrow 1$ **to** K **do**
    $(x_0, y_0, z_0, z_y, t_n, z_{t_n}, \widehat{z}_0^{t_n}, t, z_t) \leftarrow \text{SampleEverything}()$ // Generate training data
    $\mathcal{L}_{\text{fake}} \leftarrow w_t \| f_\phi(z_t, y_0, t) - \widehat{z}_0^{t_n} \|_2^2$ // Eq. (5)
    $\mathcal{L}_{\text{GAN}} \leftarrow \text{calcGANLossD}(\text{D}_\psi(f_\phi^{\text{encoder}}(\widehat{z}_0^{t_n}, y_0, 0)), \text{D}_\psi(f_\phi^{\text{encoder}}(z_0, y_0, 0)))$ // Eq. (10)
    $\mathcal{L}_\phi^{\text{total}} \leftarrow \mathcal{L}_{\text{fake}} + \lambda_2 \mathcal{L}_{\text{GAN}}$ // Eq. (11)
    Update ϕ by using $\frac{\partial \mathcal{L}_\phi^{\text{total}}}{\partial \phi}$
    Update ψ by using $\frac{\partial \mathcal{L}_{\text{GAN}}}{\partial \psi}$
  end for
  // Train generator model
  $(x_0, y_0, z_0, z_y, t_n, z_{t_n}, \widehat{z}_0^{t_n}, t, z_t) \leftarrow \text{SampleEverything}()$ // Generate training data

  $\mathcal{L}_\theta \leftarrow \text{calcThetaLoss}(f^*(z_t, y_0, t), f_\phi(z_t, y_0, t), \widehat{z}_0^{t_n})$ // Compute $\mathcal{L}_\theta$ loss with Eq. (8)

  Sample $z_T \sim \mathcal{N}(z_T|z_y, \kappa^2\mathbf{I})$; $\widehat{z}_0 \leftarrow G_\theta(z_T, y_0, T, \epsilon)$ // Eq. (38)
  $\mathcal{L}_{\text{LPIPS}} \leftarrow \text{LPIPS}(x_0, \text{Dec}(\widehat{z}_0))$ // Compute $\mathcal{L}_{\text{LPIPS}}$ loss

  // Compute generator $\mathcal{L}_{\text{GAN}}$ loss
  $\mathcal{L}_{\text{GAN}} \leftarrow \text{calcGANLossG}(\text{D}_\psi(f_\phi^{\text{encoder}}(\widehat{z}_0^{t_n}, y_0, 0)))$ // Eq. (10)

  $\mathcal{L}_\theta^{\text{total}} \leftarrow \mathcal{L}_\theta + \lambda_1 \mathcal{L}_{\text{LPIPS}} + \lambda_2 \mathcal{L}_{\text{GAN}}$ // Eq. (11)
  Update θ by using $\frac{\partial \mathcal{L}_\theta^{\text{total}}}{\partial \theta}$
end while

The pseudocode for the baseline ResShift-VSD training algorithm is presented in Algorithm 2, while the foundational theoretical framework is detailed in Appendix A.1. To ensure a fair comparison with the distillation loss in OSEDiff (Wu et al., 2024a), specifically the VSD loss, under an identical experimental setup (i.e., ResShift), we adapted it to the ResShift framework using the same implementation details. In Table 8 we provide a detailed explanation of the notation used in Algorithms 1 and 2.

Algorithm 2: ResShift-VSD.

Input:
Training dataset $p_{\text{data}}(x_0, y_0)$;
Pretrained ResShift Teacher model f^*; frozen encoder and decoder of VAE: Enc, Dec;
Number of fake ResShift (f_ϕ) training iterations K;

Output:
A trained generator G_θ;

func SampleEverything()
  Sample $(x_0, y_0) \sim p_{\text{data}}(x_0, y_0)$;
  $z_y \leftarrow \text{Enc}(\text{upsample}(y_0))$
  Sample $z_T \sim \mathcal{N}(z_y, \kappa^2 \eta_T \mathbf{I})$ // Eq. (38)
  $\widehat{z}_0 \leftarrow G_\theta(z_T, y_0, T)$
  Sample $t \sim \mathcal{U}\{1, \ldots, T\}$, $z_t \sim q(z_t|\widehat{z}_0, z_y)$ // Eq. (38)
  return $(y_0, t, z_t, \widehat{z}_0)$

// Initialize generator from pretrained model
// Initialize fake ResShift from pretrained model
$G_\theta \leftarrow \text{copyWeightsAndUnfreeze}(f^*)$;
$f_\phi \leftarrow \text{copyWeightsAndUnfreeze}(f^*)$;

while *train* **do**
  // Train fake ResShift model
  for $k \leftarrow 1$ **to** K **do**
    $(y_0, t, z_t, \widehat{z}_0) \leftarrow \text{SampleEverything}()$ // Generate training data
    $\mathcal{L}_{\text{fake}} \leftarrow w_t \| f_\phi(z_t, y_0, t) - \widehat{z}_0 \|_2^2$ // Eq. (5)
    Update ϕ by using $\frac{\partial \mathcal{L}_{\text{fake}}}{\partial \phi}$
  end for

  // Train generator model
  $(y_0, t, z_t, \widehat{z}_0) \leftarrow \text{SampleEverything}()$ // Generate training data
  $\mathcal{L}_\theta \leftarrow \text{calcThetaLoss}(\text{stopgrad}(\, f^*(z_t, y_0, t)\,), \text{stopgrad}(\, f_\phi(z_t, y_0, t)\,), \widehat{z}_0)$ // Eq. (8)
  Update θ by using $\frac{\partial \mathcal{L}_\theta}{\partial \theta}$
end while

Table 8: Notation used in our paper. Pixel-space refers to the image domain, while latent-space refers to the internal representation domain.

Symbol	Description	Space
x_0	Original high-resolution image	Pixel-space
$\hat{x}_0$	Reconstructed high-resolution image from $\hat{z}_0$	Pixel-space
y_0	Low-resolution input image	Pixel-space
z_0	Latent representation of x_0	Latent-space
z_y	Latent representation of y_0	Latent-space
z_{t_n}	Noised latent sampled from z_0	Latent-space
z_T	Noised latent sampled from $\mathcal{N}(z_T \vert z_y, \kappa^2 I)$	Latent-space
$\hat{z}_0$	Denoised latent output of generator $G_\theta(z_T, y_0, T, \epsilon)$	Latent-space
z_t	Noised latent sampled from $q(z_t \vert \hat{z}_0^{t_n}, z_y)$	Latent-space
$\hat{z}_0^{t_n}$	Generator output from $G_\theta(z_{t_n}, y_0, t_n, \epsilon)$	Latent-space
$f^*(z_t, y_0, t)$	Frozen teacher network output	Latent-space
$f_\phi(z_t, y_0, t)$	Student network output (trained)	Latent-space
ϵ	Noise variable sampled from $\mathcal{N}(0, I)$	Latent-space

C EXPERIMENTAL DETAILS

Noise condition. By default, fake ResShift and generator models are initialized with teacher weights. Furthermore, for noise conditioning, as described in §3.2, we implement an additional convolutional channel to expand the generator's first convolutional layer to accept noise as an additional input. The noise is concatenated with the encoded low-resolution image and is processed by a separate zero-initialized convolutional layer.

Training hyperparameters. We use the same hyperparameters as SinSR for training, including batch size, EMA rate, and optimizer type. To achieve smoother convergence, we replace the learning rate scheduler with a constant learning rate of 5×10^{-5}, which corresponds to the base learning rate of SinSR. Additionally, we adjust the AdamW (Loshchilov & Hutter, 2019) optimizer's β parameters to $[0.9, 0.95]$ to further stabilize training. To ensure controlled adaptation between the generator and the fake ResShift models, we update the generator's weights once for every $K = 5$ updates of the fake model, following the strategy of DMD2 (Yin et al., 2024a). The influence of the hyperparameter K on the training stability of RSD and its results is validated in Section 4.3. Furthermore, we adopt the loss normalization technique proposed in SiD (Zhou et al., 2024) to improve the stability of the training. In the final loss function (Equation 11), we set $\lambda_1 = 2$ and $\lambda_2 = 3 \cdot 10^{-3}$ following OSEDiff (Wu et al., 2024a) and DMD2, respectively.

Training time. The complete RSD training process, performed on 4 NVIDIA A100 GPUs, takes approximately 5 hours. During this time, the student model undergoes around 3000 gradient update iterations, while the fake model completes 15000 iterations. In practice, we found that SinSR (Wang et al., 2024b) requires around 60 hours on a single NVIDIA A100 GPU for 30000 iterations (2.57 days in Table 7 of SinSR (Wang et al., 2024b)) and SinSR converges roughly 3 times slower than RSD. We explain this difference by **simulation-free property** of RSD, which SinSR does not have. We recall that SinSR is a knowledge distillation method, which runs a full teacher ResShift model for all $T = 15$ steps during training according to Equations 5 and 6 in SinSR (Wang et al., 2024b):

$$x_{t-1} = k_t f^*(x_t, y_0, t) + m_t x_t + j_t y_0, \quad t \in \{T, T-1, \ldots, 2, 1\}, \tag{34}$$

$$F(x_T, y_0) = x_0, \quad x_T = y_0 + \kappa\sqrt{\eta_T}\epsilon, \quad \epsilon \sim \mathcal{N}(0, \mathbf{I}), \tag{35}$$

$$\mathcal{L}_{distill,SinSR} = L_{MSE}(f_\theta(x_T, y_0, T), F(x_T, y_0)), \tag{36}$$

where $f_\theta(x_T, y_0, T)$ is the student network in SinSR, which directly predicts the HR image in only one step, $F(x_T, y_0)$ represents the deterministic sampling with the ResShift teacher model using Equation (34), and $f^*(x_t, y_0, t)$ is the teacher model in ResShift. During training, RSD does not require full teacher simulation as SinSR in Equation (34). However, in the RSD training, additional $K = 5$ updates for the fake model are required, while SinSR does not have any fake model. Thus, RSD achieves an acceleration of around $\times 3$ for training compared to SinSR.

Codebase. Our method is implemented based on the original SinSR repository (Wang et al., 2024b), which serves as the primary source of code for our experiments. We build our method on this framework to implement our training Algorithm 1, which is given in Appendix B.

Teacher checkpoint. Following SinSR repository (Wang et al., 2024b), we also distill the same ResShift checkpoint `resshift_realsrx4_s15_v1.pth`, which was trained with 300k iterations.

Datasets and baselines. Table 9 lists details on the datasets used for training and testing, including their sources and download links. Table 10 provides associated licenses for used datasets. Table 11 lists the models used for training and quality comparison and links to access them.

Evaluation of metrics for SR models. For calculating SR metrics, we use the PyTorch Toolbox for Image Quality Assessment and `pyiqa` package (Chen & Mo, 2022). We also used the image quality assessment script provided in the OSEDiff GitHub repository.

Table 9: The used datasets and their sources

Name	URL	Citation
RealSR-V3	GitHub Link	(Cai et al., 2019)
RealSet65	GitHub Link	(Yue et al., 2023)
DRealSR	GitHub Link	(Wei et al., 2020)
ImageNet	Website Link	(Deng et al., 2009)
ImageNet-Test	Google Drive Link	(Yue et al., 2023)
DIV2K-Val-512	Hugging Face Link	(Agustsson & Timofte, 2017; Wang et al., 2024a)
DRealSR-512	Hugging Face Link	(Wang et al., 2024a; Wei et al., 2020)
RealSR-512	Hugging Face Link	(Wang et al., 2024a; Cai et al., 2019)
RealLR200	Google Drive Link	(Wu et al., 2024b)
RealLQ250	Google Drive Link	(Ai et al., 2024)

Table 10: The used datasets and their licenses

Name	License
RealSR-V3	NTU S-Lab License 1.0
DRealSR	Unknown
ImageNet	Custom (research, non-commercial)
ImageNet-Test	NTU S-Lab License
DIV2K-Val-512	NTU S-Lab License
DRealSR-512	NTU S-Lab License
RealSR-512	NTU S-Lab License
RealLR200	Apache 2.0 License
RealLQ250	Apache 2.0 License

Table 11: Baselines used for comparison. In each case, we used original code from GitHub repositories and model weights.

Name	URL	Citation	License
Real-ESRGAN	GitHub Link	(Wang et al., 2021)	BSD 3-Clause License
BSRGAN	GitHub Link	(Zhang et al., 2021)	Apache-2.0 license
SwinIR	GitHub Link	(Liang et al., 2021)	Apache-2.0 license
ResShift	GitHub Link	(Yue et al., 2023)	NTU S-Lab License 1.0
SinSR	GitHub Link	(Wang et al., 2024b)	CC BY-NC-SA 4.0
SUPIR	GitHub Link	(Yu et al., 2024)	SUPIR Software License
OSEDiff	GitHub Link	(Wu et al., 2024a)	Apache License 2.0
AdcSR	GitHub Link	(Chen et al., 2025)	Apache License 2.0
PiSA-SR	GitHub Link	(Sun et al., 2025)	Apache License 2.0
TSD-SR	GitHub Link	(Dong et al., 2025)	Apache License 2.0
CTMSR	GitHub Link	(You et al., 2025)	MIT License
CCSR	GitHub Link	(Sun et al., 2024)	Apache License 2.0
InvSR	GitHub Link	(Yue et al., 2025)	NTU S-Lab License 1.0

D ADDITIONAL QUANTITATIVE RESULTS

We present an additional set of quantitative results, including more baselines and evaluations on full-size DRealSR (Wei et al., 2020), RealLR200 (Wu et al., 2024b), RealLQ250 (Ai et al., 2024), and ImageNet-Test (Yue et al., 2023), which were not included in the main text due to space limitations:

- Table 12 provides results on full-size images from the DRealSR dataset (Wei et al., 2020).
- Table 13 provides non-reference results on full-size images from the RealLR200 (Wu et al., 2024b) and RealLQ250 (Ai et al., 2024) datasets.
- Table 14 provides results for the ImageNet-Test dataset (Yue et al., 2023).
- Table 15 presents an extension version of Table 1 on RealSR (Cai et al., 2019) and RealSet65 (Yue et al., 2023) datasets with additional baselines.
- Table 16 presents an extension version of Table 2 on crops from DIV2K (Agustsson & Timofte, 2017), RealSR, and DRealSR used in StableSR (Wang et al., 2024a) with additional baselines.

Table 12. We evaluated the following models on real-world DRealSR (Wei et al., 2020) for Table 12 and followed their official implementations listed in Table 11:

1. **Diffusion-based SR models**. We ran pre-trained models of ResShift (Yue et al., 2023), SinSR (Wang et al., 2024b), OSEDiff (Wu et al., 2024a), and SUPIR (Yu et al., 2024) as representative members of diffusion-based SR models. We used the following checkpoints from the respective official repositories listed in Table 11: `resshift_realsrx4_s15_v1.pth`, `SinSR_v2.pth`, `osediff.pkl` and `SUPIR-v0Q.ckpt`. Due to the high resolution of the DRealSR images and the high demands for GPU memory for the SUPIR model, we ran it with tiled VAE using the flag `--use_tile_vae`.
2. **State-of-the-art diffusion-based one-step SR models**. In addition to ResShift, SinSR, OSEDiff, and SUPIR models, we also ran pre-trained recent state-of-the-art one-step diffusion SR models, including TSD-SR (Dong et al., 2025), PiSA-SR (Sun et al., 2025), CTMSR (You et al., 2025), CCSR (Sun et al., 2024), and InvSR (Yue et al., 2025). We used the following checkpoints from the respective repositories listed in Table 11: 1) TSD-SR - LoRA weights from the folder `checkpoint/tsdsr-mse`, embedding weights from the folder `dataset/default`, and the teacher SD3-medium model from the Hugging Face Link; 2) PiSA-SR - `pisa_sr.pkl`; 3) CTMSR - `CTMSR.pth`; 4) InvSR - `noise_predictor_sd_turbo_v5_diftune.pth`; 5) CCSR - to follow the CCSR GitHub repository, we used ControlNet weights from the Google Drive Link, VAE weights from the Google Drive Link, and pre-trained ControlNet weights from the Google Drive Link, and Dino models from the Google Drive Link, respectively.
3. **GAN-based SR models**. We ran pre-trained GAN-based SR models of Real-ESRGAN (Wang et al., 2021) and BSRGAN (Zhang et al., 2021) with the checkpoint names `RealESRGAN_x4plus.pth` and `BSRGAN.pth`, which are provided in the respective GitHub repositories listed in Table 11.
4. **Transformer-based SR models**. We ran pre-trained SwinIR model (Liang et al., 2021) with the checkpoint name `003_realSR_BSRGAN_DFOWMFC_s64w8_SwinIR-L_x4_GAN.pth` as the representative model from transformer-based SR models using the respective GitHub repository listed in Table 11.

We compute the same set of metrics as in Table 2 - PSNR, SSIM, LPIPS, CLIPIQA, MUSIQ, DISTS, NIQE, and MANIQA-PIPAL.

Table 13. We evaluated RSD and the following diffusion models on real-world benchmarks, namely RealLR200 (Wu et al., 2024b) and RealLQ250 (Ai et al., 2024), using no-reference perceptual metrics (CLIPIQA, MUSIQ, NIQE, MANIQA), which follows the evaluation protocol of SeeSR (Wu et al., 2024a, Table 2) and DreamClear (Ai et al., 2024, Table 1):

1. **Diffusion-based SR models without T2I models**. We evaluated methods which were trained on the ImageNet data, namely ResShift, SinSR, CTMSR, and RSD.

2. **T2I-based diffusion SR models**. We evaluated SUPIR, OSEDiff, AdcSR, PiSA-SR, TSD-SR, InvSR, and CCSR. For AdcSR (Chen et al., 2025), we used the weights from the checkpoint `net_params_200.pkl` from the respective GitHub repository.

Table 14. We report quantitative results of the baselines used in the ResShift and SinSR papers, and additional T2I-based SR models on the synthetic ImageNet-Test dataset (Yue et al., 2023), which follows the evaluation setup of ResShift (Yue et al., 2023, Table 3) and SinSR (Wang et al., 2024b, Table 2), and CTMSR (You et al., 2025, Table 1):

1. **Diffusion-based SR models**. We borrow the results of Table 2 from SinSR for LDM-15 and LDM-30 (Rombach et al., 2022) and SinSR (Wang et al., 2024b). We borrow the results of Table 3 from ResShift (Yue et al., 2023) for ResShift.
2. **GAN-based SR models**. We borrow the results of Table 2 from SinSR for ESRGAN (Wang et al., 2019), RealSR-JPEG (Ji et al., 2020), Real-ESRGAN (Wang et al., 2021), BSRGAN (Zhang et al., 2021).
3. **DASR and SwinIR**. We also borrow the results of Table 2 from SinSR for DASR (Liang et al., 2022b) and SwinIR (Liang et al., 2021).
4. **State-of-the-art diffusion-based one-step SR models**. In addition to TSD-SR, PiSA-SR, CTMSR, and AdcSR, we also evaluated InvSR and CCSR using the same pre-trained models as for Table 12.

We report the same set of metrics that was used in ResShift (Yue et al., 2023, Table 3) and SinSR (Wang et al., 2024b, Table 2): PSNR, SSIM, LPIPS, CLIPIQA, and MUSIQ.

Table 15. We report an extended version of Table 1 with additional baselines used in ResShift and SinSR papers:

1. **GAN-based SR models**. We evaluated Real-ESRGAN (Wang et al., 2021) and BSRGAN (Zhang et al., 2021) on RealSR and RealSet65.
2. **SwinIR**. We also evaluated SwinIR on RealSR and RealSet65.
3. **State-of-the-art diffusion-based one-step SR models**. In addition to TSD-SR, PiSA-SR, CTMSR, and AdcSR, we also evaluated InvSR and CCSR using the same pre-trained models as for Table 12.

Table 16. We report an extended version of Table 2 with additional baselines used in the OSEDiff paper:

1. **Diffusion-based SR models**. We borrow the results of Table 1 from OSEDiff for StableSR (Wang et al., 2024a), DiffBIR (Lin et al., 2025), SeeSR (Wu et al., 2024b), PASD (Yang et al., 2025), ResShift (Yue et al., 2023), and SinSR (Wang et al., 2024b).
2. **GAN-based SR models**. We borrow the results of Table 1 from OSEDiff for Real-ESRGAN (Wang et al., 2021), BSRGAN (Zhang et al., 2021), LDL (Liang et al., 2022a) and FeMASR (Chen et al., 2022).
3. **State-of-the-art diffusion-based one-step SR models**. In addition to TSD-SR, PiSA-SR, CTMSR, and AdcSR, we also evaluated InvSR and CCSR using the same pre-trained models as for Table 12.

These results demonstrate that our RSD model achieves performance comparable to the state-of-the-art diffusion SR models across a broad range of metrics and methods under the requirements of a restricted computational budget. We discuss a comparison between RSD and recent one-step diffusion SR models, namely CTMSR, TSD-SR, PiSA-SR, AdcSR, InvSR, and CCSR, in detail in Appendix E.

Table 12: Quantitative results of models on full size images from DRealSR (Wei et al., 2020). The best and second best results are highlighted in **bold** and underline.

Methods	Model class	NFE	PSNR↑	SSIM↑	LPIPS↓	CLIPIQA↑	MUSIQ↑	DISTS↓	NIQE↓	MANIQA↑
BSRGAN (Zhang et al., 2021)	GANs	1	28.34	0.8206	0.2929	0.5704	35.500	0.1636	4.6811	0.4682
Real-ESRGAN (Wang et al., 2021)		1	27.91	0.8249	0.2818	0.5180	35.255	0.1464	4.7142	0.4756
SwinIR (Liang et al., 2021)	Transformer	1	28.31	**0.8272**	**0.2741**	0.5072	35.826	**0.1387**	4.6665	0.4617
SUPIR (Yu et al., 2024)	Diffusion model, used T2I prior	50	25.73	0.7224	0.3906	0.5862	36.089	0.1944	4.4685	0.5720
OSEDiff (Wu et al., 2024a)		1	26.67	0.7922	0.3123	0.7264	37.761	0.1617	4.1768	0.5883
PiSA-SR (Sun et al., 2025)		1	27.43	0.8119	0.2844	0.6878	35.060	0.1537	4.4783	0.5615
TSD-SR (Dong et al., 2025)		1	26.53	0.7637	0.3084	**0.7517**	37.395	0.1567	**3.6624**	0.5549
InvSR (Yue et al., 2025)		1	26.06	0.7455	0.3578	0.7485	33.878	0.1838	3.7279	**0.5928**
CCSR (Sun et al., 2024)		1	27.71	0.8022	0.3208	0.7104	35.716	0.1816	4.3081	0.5720
ResShift (Yue et al., 2023)	Diffusion model, no T2I prior	15	**28.76**	0.7863	0.4310	0.5838	32.042	0.2314	6.6335	0.4297
CTMSR (You et al., 2025)		1	28.28	0.8017	0.3355	0.6821	33.206	0.1946	4.7795	0.4702
SinSR (Wang et al., 2024b)		1	27.32	0.7233	0.4452	0.7223	32.800	0.2368	5.5748	0.4757
RSD (**Ours**)		1	27.66	0.7864	0.3105	0.7398	**38.340**	0.1868	4.6098	0.5314

Table 13: Quantitative results of diffusion models on RealLR200 (Wu et al., 2024b) and RealLQ250 (Ai et al., 2024) datasets. The best and second best results are highlighted in **bold** and underline.

Methods	T2I prior	NFE	Datasets							
			RealLR200				*RealLQ250*			
			CLIPIQA↑	MUSIQ↑	NIQE↓	MANIQA↑	CLIPIQA↑	MUSIQ↑	NIQE↓	MANIQA↑
SUPIR (Yu et al., 2024)	yes, $>$ 450M params	50	0.6188	64.79	4.1862	0.6120	0.5746	65.72	**3.6607**	0.5969
OSEDiff (Wu et al., 2024a)		1	0.6728	69.45	4.0506	0.6153	0.6724	69.56	3.9682	0.5889
AdcSR (Chen et al., 2025)		1	0.7047	70.35	3.8792	0.6174	0.6889	69.98	3.7181	0.5944
PiSA-SR (Sun et al., 2025)		1	0.7039	70.90	3.9594	0.6419	0.7054	71.25	3.9162	**0.6190**
TSD-SR (Dong et al., 2025)		1	**0.7335**	**72.06**	**3.8352**	0.6248	**0.7368**	**73.22**	3.6996	0.6037
InvSR (Yue et al., 2025)		1	0.6774	68.15	4.0378	**0.6461**	0.6499	64.77	4.6505	0.5810
CCSR (Sun et al., 2024)		1	0.6937	70.49	4.3108	0.6319	0.6850	70.80	4.4760	0.6021
ResShift (Yue et al., 2023)	no, $<$ 180M params	15	0.6368	61.80	5.7016	0.5436	0.6348	61.99	5.7622	0.5364
SinSR (Wang et al., 2024b)		1	0.7089	64.90	5.3329	0.5561	0.7142	65.29	5.4630	0.5294
CTMSR (You et al., 2025)		1	0.6754	67.63	4.2943	0.5426	0.6701	68.07	4.5831	0.5130
RSD (**Ours**)		1	0.7151	68.66	4.7074	0.5949	0.7252	69.63	4.5531	0.5826

Table 14: Quantitative results of models on ImageNet-Test (Yue et al., 2023). The best and second best results are highlighted in **bold** and underline.

Methods	Model class	NFE	PSNR↑	SSIM↑	LPIPS↓	CLIPIQA↑	MUSIQ↑
ESRGAN (Wang et al., 2019)	GANs	1	20.67	0.448	0.485	0.451	43.615
Real-ESRGAN (Wang et al., 2021)		1	24.04	0.665	0.254	0.523	52.538
RealSR-JPEG (Ji et al., 2020)		1	23.11	0.591	0.326	0.537	46.981
BSRGAN (Zhang et al., 2021)		1	24.42	0.659	0.259	0.581	54.697
SwinIR (Liang et al., 2021)	Transformer	1	23.99	0.667	0.238	0.564	53.790
DASR (Liang et al., 2022b)	Mixture of experts	1	24.75	0.675	0.250	0.536	48.337
LDM (Rombach et al., 2022)	Diffusion model, used T2I prior	30	24.49	0.651	0.248	0.572	50.895
LDM (Rombach et al., 2022)		15	24.89	0.670	0.269	0.512	46.419
SUPIR (Yu et al., 2024)		50	22.56	0.574	0.302	**0.786**	60.487
OSEDiff (Wu et al., 2024a)		1	23.02	0.619	0.253	0.677	60.755
AdcSR (Chen et al., 2025)		1	22.99	0.615	0.252	0.711	63.218
PiSA-SR (Sun et al., 2025)		1	24.29	0.670	0.213	0.629	62.137
TSD-SR (Dong et al., 2025)		1	23.58	0.645	0.197	0.673	**65.299**
InvSR (Yue et al., 2025)		1	21.31	0.604	0.293	0.641	54.870
CCSR (Sun et al., 2024)		1	24.79	**0.677**	0.238	0.602	61.789
ResShift (Yue et al., 2023)	Diffusion model, no T2I prior	15	**25.01**	**0.677**	0.231	0.592	53.660
CTMSR (You et al., 2025)		1	24.73	0.666	0.197	0.691	60.142
SinSR (distill only) (Wang et al., 2024b)		1	24.69	0.664	0.222	0.607	53.316
SinSR (Wang et al., 2024b)		1	24.56	0.657	0.221	0.611	53.357
ResShift-VSD (Appendix A)		1	23.69	0.624	0.230	0.665	58.630
RSD (**Ours**, distill only)		1	23.97	0.643	0.217	0.660	57.831
RSD (**Ours**)		1	24.31	0.657	**0.193**	0.681	58.947

Table 15: Extended quantitative results of models on two real-world datasets, RealSR (Cai et al., 2019) and RealSet65 (Yue et al., 2023). The best and second best results are highlighted in **bold** and underline.

Methods	Model class	NFE	Datasets						
			RealSR					*RealSet65*	
			PSNR↑	SSIM↑	LPIPS↓	CLIPIQA↑	MUSIQ↑	CLIPIQA↑	MUSIQ↑
BSRGAN (Zhang et al., 2021)	GANs	1	**26.51**	0.775	0.269	0.5439	63.586	0.6163	65.582
Real-ESRGAN (Wang et al., 2021)		1	25.85	0.773	0.273	0.4898	59.678	0.5995	63.220
SwinIR (Liang et al., 2021)	Transformer	1	26.43	**0.786**	**0.251**	0.4654	59.636	0.5782	63.822
SUPIR (Yu et al., 2024)	Diffusion model, used T2I prior	50	24.38	0.698	0.331	0.5449	63.676	0.6133	66.460
OSEDiff (Wu et al., 2024a)		1	25.25	0.737	0.299	0.6772	67.602	0.6836	68.853
AdcSR (Chen et al., 2025)		1	25.63	0.735	0.300	0.7033	67.550	0.7044	69.185
PiSA-SR (Sun et al., 2025)		1	25.59	0.750	**0.271**	0.6678	67.993	0.7062	70.208
TSD-SR (Dong et al., 2025)		1	24.88	0.723	0.281	0.7336	**69.871**	0.7263	**70.958**
InvSR (Yue et al., 2025)		1	24.73	0.731	0.275	0.6798	66.403	0.6990	67.770
CCSR (Sun et al., 2024)		1	25.99	0.752	0.287	0.6656	67.991	0.7150	70.731
ResShift (Yue et al., 2023)	Diffusion model, no T2I prior	15	26.49	0.754	0.360	0.5958	59.873	0.6537	61.330
CTMSR (You et al., 2025)		1	26.18	**0.765**	0.294	0.6449	64.782	0.6871	67.032
SinSR (distill only) (Wang et al., 2024b)		1	26.14	0.732	0.357	0.6119	57.118	0.6822	61.267
SinSR (Wang et al., 2024b)		1	25.83	0.717	0.365	0.6887	61.582	0.7150	62.169
ResShift-VSD (Appendix A)		1	23.96	0.616	0.466	0.7479	63.298	**0.7606**	66.701
RSD (**Ours**, distill only)		1	24.92	0.696	0.355	**0.7518**	66.430	0.7534	68.383
RSD (**Ours**)		1	25.91	0.754	0.273	0.7060	65.860	0.7267	69.172

Table 16: Extended quantitative results of models on crops from StableSR (Wang et al., 2024a). The best and second best results are highlighted in **bold** and underline.

Datasets	Methods	Model class	NFE	PSNR↑	SSIM↑	LPIPS↓	DISTS↓	NIQE↓	MUSIQ↑	MANIQA↑	CLIPIQA↑	FID↓
DIV2K-Val	BSRGAN (Zhang et al., 2021)	GANs	1	24.58	0.6269	0.3351	0.2275	4.7518	61.20	0.5071	0.5247	44.23
	Real-ESRGAN (Wang et al., 2021)		1	24.29	**0.6371**	0.3112	0.2141	4.6786	61.06	0.5501	0.5277	37.64
	LDL (Liang et al., 2022a)		1	23.83	0.6344	0.3256	0.2227	4.8554	60.04	0.5350	0.5180	42.29
	FeMASR (Chen et al., 2022)		1	23.06	0.5887	0.3126	0.2057	4.7410	60.83	0.5074	0.5997	35.87
	StableSR (Wang et al., 2024a)	Diffusion model, used T2I prior	200	23.26	0.5726	0.3113	0.2048	4.7581	65.92	0.6192	0.6771	**24.44**
	DiffBIR (Lin et al., 2025)		50	23.64	0.5647	0.3524	0.2128	4.7042	65.81	0.6210	0.6704	30.72
	SeeSR (Wu et al., 2024b)		50	23.68	0.6043	0.3194	0.1968	4.8102	68.67	0.6240	0.6936	25.90
	PASD (Yang et al., 2025)		20	23.14	0.5505	0.3571	0.2207	4.3617	68.95	**0.6483**	0.6788	29.20
	SUPIR (Yu et al., 2024)		50	22.13	0.5280	0.3923	0.2314	5.6758	63.82	0.5933	0.7147	31.46
	OSEDiff (Wu et al., 2024a)		1	23.72	0.6108	0.2941	0.1976	4.7097	67.97	0.6148	0.6683	26.32
	AdcSR (Chen et al., 2025)		1	23.74	0.6017	0.2853	0.1899	4.3579	68.00	0.6073	0.6764	25.52
	PiSA-SR (Sun et al., 2025)		1	23.87	0.6058	0.2823	0.1934	4.5565	69.68	0.6375	0.6928	25.09
	TSD-SR (Dong et al., 2025)		1	23.02	0.5808	**0.2673**	**0.1821**	**4.3244**	**71.69**	0.6192	**0.7416**	29.16
	InvSR (Yue et al., 2025)		1	23.10	0.5985	0.3045	0.1985	4.7056	68.43	0.6385	0.7117	28.45
	CCSR (Sun et al., 2024)		1	24.30	0.6283	0.2979	0.2020	5.3367	69.52	0.6145	0.6752	30.86
	ResShift (Yue et al., 2023)	Diffusion model, no T2I prior	15	24.65	0.6181	0.3349	0.2213	6.8212	61.09	0.5454	0.6071	36.11
	SinSR (Wang et al., 2024b)		1	24.41	0.6018	0.3240	0.2066	6.0159	62.82	0.5386	0.6471	35.57
	CTMSR (You et al., 2025)		1	**24.88**	0.6265	0.3026	0.2040	5.1146	65.62	0.5165	0.6601	34.15
	RSD (**Ours**)		1	23.91	0.6042	0.2857	0.1940	5.1987	68.05	0.5937	0.6967	34.84
DRealSR	BSRGAN (Zhang et al., 2021)	GANs	1	**28.75**	0.8031	0.2883	0.2142	6.5192	57.14	0.4878	0.4915	155.63
	Real-ESRGAN (Wang et al., 2021)		1	28.64	0.8053	0.2847	**0.2089**	6.6928	54.18	0.4907	0.4422	147.62
	LDL (Liang et al., 2022a)		1	28.21	**0.8126**	**0.2815**	0.2132	7.1298	53.85	0.4914	0.4310	155.53
	FeMASR (Chen et al., 2022)		1	26.90	0.7572	0.3169	0.2235	5.9073	53.74	0.4420	0.5464	157.78
	StableSR (Wang et al., 2024a)	Diffusion model, used T2I prior	200	28.03	0.7536	0.3284	0.2269	6.5239	58.51	0.5601	0.6356	148.98
	DiffBIR (Lin et al., 2025)		50	26.71	0.6571	0.4557	0.2748	6.3124	61.07	0.5930	0.6395	166.79
	SeeSR (Wu et al., 2024b)		50	28.17	0.7691	0.3189	0.2315	6.3967	64.93	0.6042	0.6804	147.39
	PASD (Yang et al., 2025)		20	27.36	0.7073	0.3760	0.2531	**5.5474**	64.87	0.6169	0.6808	156.13
	SUPIR (Yu et al., 2024)		50	24.93	0.6360	0.4263	0.2823	7.4336	59.39	0.5537	0.6799	164.86
	OSEDiff (Wu et al., 2024a)		1	27.92	0.7835	0.2968	0.2165	6.4902	64.65	0.5899	0.6963	135.30
	AdcSR (Chen et al., 2025)		1	28.10	0.7726	0.3046	0.2200	6.4467	66.27	0.5916	0.7049	134.05
	PiSA-SR (Sun et al., 2025)		1	28.32	0.7804	0.2960	0.2169	6.1766	66.11	0.6161	0.6968	**130.61**
	TSD-SR (Dong et al., 2025)		1	27.77	0.7559	0.2967	0.2136	5.9131	**66.62**	0.5874	**0.7343**	134.98
	InvSR (Yue et al., 2025)		1	25.79	0.7176	0.3471	0.2381	5.8627	64.92	**0.6212**	0.7185	166.51
	CCSR (Sun et al., 2024)		1	28.24	0.7818	0.3201	0.2327	6.7901	66.28	0.6056	0.6632	157.23
	ResShift (Yue et al., 2023)	Diffusion model, no T2I prior	15	28.46	0.7673	0.4006	0.2656	8.1249	50.60	0.4586	0.5342	172.26
	SinSR (Wang et al., 2024b)		1	28.36	0.7515	0.3665	0.2485	6.9907	55.33	0.4884	0.6383	170.57
	CTMSR (You et al., 2025)		1	28.65	0.7834	0.3238	0.2358	6.1828	59.78	0.4861	0.6497	163.63
	RSD (**Ours**)		1	27.40	0.7559	0.3042	0.2343	6.2577	62.03	0.5625	0.7019	167.47
RealSR	BSRGAN (Zhang et al., 2021)	GANs	1	**26.39**	**0.7654**	**0.2670**	0.2121	5.6567	63.21	0.5399	0.5001	141.28
	Real-ESRGAN (Wang et al., 2021)		1	25.69	0.7616	0.2727	0.2063	5.8295	60.18	0.5487	0.4449	135.18
	LDL (Liang et al., 2022a)		1	25.28	0.7567	0.2766	0.2121	6.0024	60.82	0.5485	0.4477	142.71
	FeMASR (Chen et al., 2022)		1	25.07	0.7358	0.2942	0.2288	5.7885	58.95	0.4865	0.5270	141.05
	StableSR (Wang et al., 2024a)	Diffusion model, used T2I prior	200	24.70	0.7085	0.3018	0.2288	5.9122	65.78	0.6221	0.6178	128.51
	DiffBIR (Lin et al., 2025)		50	24.75	0.6567	0.3636	0.2312	5.5346	64.98	0.6246	0.6463	128.99
	SeeSR (Wu et al., 2024b)		50	25.18	0.7216	0.3009	0.2223	5.4081	69.77	0.6442	0.6612	125.55
	PASD (Yang et al., 2025)		20	25.21	0.6798	0.3380	0.2260	5.4137	68.75	0.6487	0.6620	124.29
	SUPIR (Yu et al., 2024)		50	23.61	0.6606	0.3589	0.2492	5.8877	63.21	0.5895	0.6709	128.35
	OSEDiff (Wu et al., 2024a)		1	25.15	0.7341	0.2921	0.2128	5.6476	69.09	0.6326	0.6693	123.49
	AdcSR (Chen et al., 2025)		1	25.47	0.7301	0.2885	0.2128	5.3477	69.90	0.6353	0.6730	118.41
	PiSA-SR (Sun et al., 2025)		1	25.50	0.7418	0.2672	**0.2044**	5.5046	70.15	0.6551	0.6696	124.09
	TSD-SR (Dong et al., 2025)		1	24.81	0.7172	0.2743	0.2105	**5.1266**	**71.18**	0.6346	**0.7160**	**114.45**
	InvSR (Yue et al., 2025)		1	24.30	0.7145	0.2775	0.2060	5.7168	67.31	**0.6572**	0.6734	129.52
	CCSR (Sun et al., 2024)		1	25.92	0.7485	0.2799	0.2122	5.7324	69.18	0.6398	0.6336	122.98
	ResShift (Yue et al., 2023)	Diffusion model, no T2I prior	15	26.31	0.7421	0.3421	0.2498	7.2365	58.43	0.5285	0.5442	141.71
	SinSR (Wang et al., 2024b)		1	26.28	0.7347	0.3188	0.2353	6.2872	60.80	0.5385	0.6122	135.93
	CTMSR (You et al., 2025)		1	25.98	0.7546	0.2897	0.2208	5.5546	64.26	0.5270	0.6318	135.35
	RSD (**Ours**)		1	25.61	0.7420	0.2675	0.2205	5.7500	66.02	0.5930	0.6793	138.23

E PERFORMANCE-EFFICIENCY TRADE-OFF FOR RSD AND RECENT STATE-OF-THE-ART ONE-STEP DIFFUSION SR METHODS

In this section, we discuss the comparison between RSD and very recent SOTA one-step diffusion SR methods - CTMSR (You et al., 2025) and T2I-based SR models, including PiSA-SR (Sun et al., 2025), TSD-SR (Dong et al., 2025), AdcSR (Chen et al., 2025), InvSR (Yue et al., 2025) and CCSR (Sun et al., 2024). We support the comparison with visual results of these models in Figure 5 for the RealLR200 dataset (Wu et al., 2024b) and Figure 6 for the RealLQ250 dataset (Ai et al., 2024), respectively.

E.1 COMPARISON WITH CTMSR

CTMSR method. CTMSR proposed a distillation-free method for one-step diffusion SR, which is based on consistency training (Song et al., 2023; Song & Dhariwal, 2024). Their training scheme is split into two stages.

Stage 1. In the first stage, they formulate the ResShift forward stochastic diffusion process in Equation (1) as the deterministic trajectory of PF-ODE (Song et al., 2021); see Equations 8 and 9 in the CTMSR paper. They trained the respective consistency model with 500k iterations using the proposed PF-ODE trajectories and the consistency loss $\mathcal{L}_{\text{CT}}$ according to Equation 10 in the CTMSR paper.

Stage 2. After the first stage, CTMSR additionally optimizes the model with the proposed Distribution Trajectory Matching objective. Its idea is to minimize the Distribution Trajectory Distance ($\mathcal{L}_{\text{DTD}}$ in Equations 15 and 16 in the CTMSR paper) between the end points of the real PF-ODE trajectory, which starts from the real HR images, and the fake PF-ODE trajectory, which starts from the predicted fake HR images; see Equations 11, 12, 13, 14 in the CTMSR paper. Computation of the gradient $\nabla_\theta \mathcal{L}_{\text{DTD}}$ with respect to the original CTMSR parameters θ requires calculating the U-Net Jacobian term. Inspired by SDS (Poole et al., 2023) and VSD (Wang et al., 2023c), CTMSR omits this U-Net Jacobian term. The authors optimized the CTMSR model using the gradients $\nabla_\theta \mathcal{L}_{\text{CT}} + \nabla_\theta \mathcal{L}_{\text{DTD}}$ with additional 2k iterations.

CTMSR uses the same training scheme on the ImageNet dataset with Real-ESRGAN degradations, which is detailed in Section 4.1, as ResShift, SinSR and RSD. Thus, CTMSR can be fairly comparable with these models.

Perceptual-fidelity comparison. According to the quantitative results in Tables 1, 2, 12, and 13, RSD has a stable improvement over CTMSR for **all real-world datasets (RealSR, RealSet65, RealSR and DRealSR** 512×512 **crops, DRealSR, RealLR200, RealLQ250)** in **most perceptual metrics (LPIPS, DISTS, CLIPIQA, MUSIQ, MANIQA)**. We observe the most notable gaps between the perceptual quality of CTMSR and RSD on the following datasets:

1. RealSR and DRealSR 512×512 crops in Table 2 - improvement in MANIQA in 0.0660 and 0.0764, respectively, and in CLIPIQA in 0.0475 and 0.0522, respectively.
2. Full-size DRealSR in Table 12 - improvement in MUSIQ in 5.134 and MANIQA in 0.0612, respectively.
3. RealLR200 and RealLQ250 in Table 13 - improvement in MANIQA in 0.0523 and 0.0696, respectively, and in CLIPIQA in 0.0397 and 0.0551, respectively.

These results highlight the strong competitive perceptual performance of RSD among one-step diffusion SR models using the similar UNet architecture with Swin Transformer blocks (Liu et al., 2021) - ResShift, SinSR and CTMSR. However, CTMSR sometimes has better NIQE values and also achieves slightly better CLIPIQA and MUSIQ on the synthetic ImageNet-Test dataset from Table 14. We note that NIQE (Mittal et al., 2013) has been shown to have a worse correlation with human preference compared to recent IQA measures, including MUSIQ, MANIQA and CLIPIQA, as evident in (Wang et al., 2023b, Tables 1 and 5), (Ke et al., 2021, Table 1), (Yang et al., 2022, Table 3). CTMSR also achieves better fidelity measures (PSNR and SSIM) compared to RSD, which are close to the results of SinSR. Unfortunately, this results in the blur problem of CTMSR, as we discuss below.

Qualitative comparison. We provide a visual comparison of RSD with CTMSR, as well as with SinSR, in Figure 5 for the RealLR200 dataset (Wu et al., 2024b) and Figure 6 for the RealLQ250 dataset (Ai et al., 2024), respectively. In Section 4.2, we observed in Figure 3 for RealSet65 (Yue et al., 2023) that CTMSR have blurry artifacts; see the roof of the house in Figure 3. We also observe this result on other images from RealSet65 (Yue et al., 2023), see bear in Figure 7. Figure 5 shows that RSD has more rich textures than CTMSR for man (top image) and trees (middle image). For the image of the bird (bottom image), RSD is the only diffusion model without T2I prior, which provides some details of its eye. Similarly, in Figure 6 we observe blur in the CTMSR images for the rose (top image), the deer (middle image), and the monkey character (bottom image). We hypothesize that the blur effect of CTMSR is inherited from its consistency training framework, which is based on deterministic sampling from ODE.

Complexity comparison. The CTMSR can be fairly compared to the RSD in computational complexity due to the similar architecture following ResShift. For inference complexity, we evaluated the pre-trained CTMSR model using its official implementation listed in Table 11 on the same setup as RSD in Table 3. According to Table 3, CTMSR has a similar number of parameters as ResShift, SinSR, and RSD (172 millions for CTMSR and 174 millions for RSD) and a similar inference time per LR image with resolution 64×64. However, we also found that CTMSR requires > 1.5 GPU memory during inference compared to RSD. As the distillation-free method, CTMSR states that ResShift and its distilled version, SinSR, are limited in two points:

1. **Considerable training costs**. Training SinSR requires the training of the teacher ResShift model and the student SinSR model, while CTMSR is able to train one-step diffusion SR model without an additional distillation stage.
2. **Limitations of the teacher model**. The performance of the student model is limited with the performance of the teacher model.

In Appendices J and G, we agree with the second statement. To verify the first statement, we trained CTMSR with 500k iterations for the first stage and additional 2k iterations for the second stage using their official training code on recommended GPUs (4 NVIDIA A100 GPUs). Following the pre-trained ResShift model, which we used for the distillation with RSD and was used for the distillation with SinSR, we also trained the ResShift model with 300k iterations using its official training code on the same 4 A100 GPUs to compare the CTMSR training time and the total training time of ResShift and RSD. The results are given in Table 17. Surprisingly, we found that the total training time for ResShift and its distillation with our RSD requires **less training time** than the training time for the distillation-free CTMSR method using the same resources. The training efficiency of the RSD model is supported by its simulation-free property, which is detailed in Appendix C. Compared to the training of the original teacher ResShift model, its distillation with our RSD method requires only the $\approx 15\%$ training time of ResShift, which leads to faster convergence than the distillation-free CTMSR even if we count the training time of ResShift. As noted in Appendix F, the training time of our RSD can be further halved using $K = 1$ without sacrificing quality. These results highlight the strong computational efficiency of RSD compared to CTMSR in both training and inference.

Table 17: Training and inference complexity for RSD, ResShift (Yue et al., 2023) and CTMSR (You et al., 2025). All models are trained on the same 4 NVIDIA A100 GPUs using the respective official training code and tested with an LR image of size 64×64 for SR factor $\times 4$. The inference is done on an NVIDIA A100 GPU. The best values are highligted in **bold**.

Methods	ResShift	RSD (**Ours**)	RSD with ResShift training	CTMSR
Inference Step (NFE)	15	**1**	**1**	**1**
Inference Time (s)	0.643	**0.059**	**0.059**	**0.059**
# Total Param (M)	**174**	**174**	**174**	**172**
Maximum GPU memory (MB)	1167	**539**	**539**	904
Training time (hours)	36	5	41	58

E.2 Comparison with PiSA-SR, TSD-SR, AdcSR, InvSR, and CCSR

PiSA-SR (Sun et al., 2025), TSD-SR (Dong et al., 2025), AdcSR (Chen et al., 2025), InvSR (Yue et al., 2025), and CCSR (Sun et al., 2024) are recent SOTA T2I-based SR models, which attempt to resolve the limitations of the OSEDiff model in different aspects.

Adjustable perception-distortion trade-off and slow training convergence. OSEDiff does not provide perception-distortion control without re-training, while the training requires 24 hours on 4 NVIDIA A100 GPUs according to Section 4.1 in OSEDiff paper. PiSA-SR proposed a decoupled training approach to train pixel and semantic level LoRA modules (Hu et al., 2022), which allows to adjust the perception-distortion trade-off by different pixel-semantic guidance scales (Ho & Salimans, 2021) during inference without the need of re-training. PiSA-SR uses ℓ_2 loss for the training of the LoRA module of pixel-level regression and CSD loss (Ho & Salimans, 2021) combined with the LPIPS loss for the training of the LoRA module of semantic level. The CSD loss is computed using the pre-trained Stable Diffusion 2.1-base model and does not require an additional fake model used in OSEDiff, leading to faster training (Ma et al., 2025) according to Figure 9 in the PiSA-SR paper.

Limitations of the VSD objective. As shown in the TSD-SR paper, the VSD objective used in OSEDiff has two limitations. The first limitation is that the guidance of the teacher is unreliable in scenarios where the initial SR outputs are suboptimal, as visualized in Figure 3 of TSD-SR. To solve this problem, TSD-SR proposed Target Score Matching, which aligns the predictions made by the teacher model on both synthetic and HR latents. The second limitation is that the matching of the score functions predicted by the teacher model and the LoRA model is inconsistent across different timesteps, which is shown in Figure 5 of TSD-SR. To address this issue, TSD-SR proposed the Distribution-Aware Sampling Module, which accumulates optimization gradients for earlier timestep samples in a single iteration, enabling the backpropagation of more gradients focused on detail optimization. TSD-SR initialized all training models from the Stable Diffusion 3 model (Esser et al., 2024).

Large computational costs of T2I-based SR models. As observed in AdcSR, the complexity of OSEDiff in terms of parameter number and inference time can still be too high for real deployments, especially on resource-limited edge devices. To reduce the complexity of OSEDiff while maintaining its high perceptual quality, AdcSR proposed an adversarial diffusion compression framework to OSEDiff. The idea of the framework is to train a smaller network after removing unnecessary OSEDiff modules and pruning the remaining modules. The training of AdcSR consists of two stages: 1) pretraining channel-pruned VAE decoder; 2) use of knowledge distillation for OSEDiff with adversarial loss to train a smaller student model.

Extension to multistep models. The OSEDiff approach is developed only for the one-step diffusion model, which limits its generation capacity and flexibility for varying perception-distortion requirements. InvSR and CCSR proposed different approaches to enable multistep diffusion models without retraining. InvSR introduces a trainable noise prediction network and reformulates the SR problem as diffusion inversion (Chihaoui et al., 2024). The noise predictor is trained to estimate the noise maps for multiple pre-selected steps via time embedding. To enable arbitrary-step inversion for the inference, InvSR uses the noise map prediction for the initialization the reverse sampling process, where the starting timestep can be freely chosen during inference, resulting in perception-distortion trade-off. CCSR achieves multistep diffusion modeling with another idea. Inspired by the StableSR (Wang et al., 2024a) perception-distortion analysis depending on the diffusion reverse time step in Figure 2 of the CCSR, it proposed to disentangle the SR process into structure generation and detail enhancement by GAN and DM, respectively.

Quantitative comparison. In Tables 12, 13, 14, 15, 16, we observe that our RSD combines the high fidelity of relatively small models (ResShift, SinSR, CTMSR) and the good perceptual quality of T2I-based SR models (TSD-SR, PiSA-SR, InvSR, CCSR, AdcSR). TSD-SR, PiSA-SR, InvSR, AdcSR and CCSR further develop T2I-based SR models to improve perceptual and fidelity quality compared to OSEDiff. Compared to these methods, RSD achieves mostly better fidelity consistency with HR images, which is evident by PSNR and SSIM metrics, with yet competitive perceptual metrics (LPIPS, CLIPIQA, MUSIQ).

Qualitative comparison. We provide a visual comparison of one-step T2I-based SR models with RSD in Figure 5 for the RealLR200 dataset (Wu et al., 2024b) and Figure 6 for the RealLQ250 dataset (Ai et al., 2024), respectively. Among these models, the model with the smallest number of parameters, AdcSR, has sharper textures and a better level of detail on most images. However, as the distillation model for OSEDiff, AdcSR can hallucinate for the same images, where OSEDiff hallucinates, see the bear in Figure 7 with an unnatural blue nose for OSEDiff and unnatural fur for AdcSR. Although other SOTA one-step T2I-based SR models, such as PiSA-SR and TSD-SR, also

generally have better perceptual quality than RSD, we observe for the rose in Figure 6 that failure cases with blurry effects or unrelated hallucination details occur even for them.

Complexity comparison. Despite the good perceptual performance of the TSD-SR, PiSA-SR, AdcSR, CCSR, and InvSR models, these T2I-based models require more computational costs compared to the other one-step T2I-based SR model, OSEDiff, and much more computational costs compared to RSD. In Table 3, we highlight that the T2I-based one-step SR models of PiSA-SR, AdcSR, and TSD-SR require much more GPU memory for inference and a much longer training time compared to RSD. This analysis supports our claim that RSD aims to compromise between fidelity, perceptual quality, and computational efficiency.

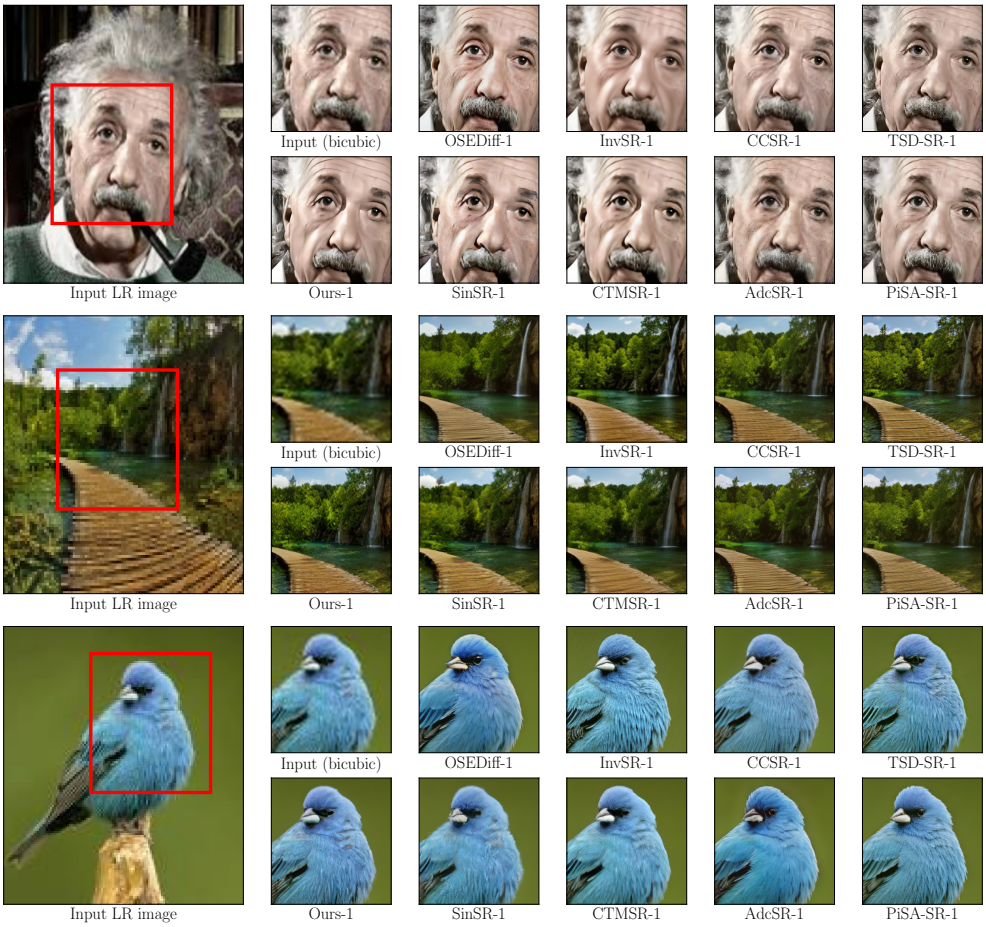

Figure 5: Visual results of recent one-step diffusion SR models (RSD, SinSR, CTMSR, OSEDiff, AdcSR, CCSR, InvSR, PiSA-SR, TSD-SR) on full-size images from RealLR200 (Wu et al., 2024b). Please zoom in for a better view.

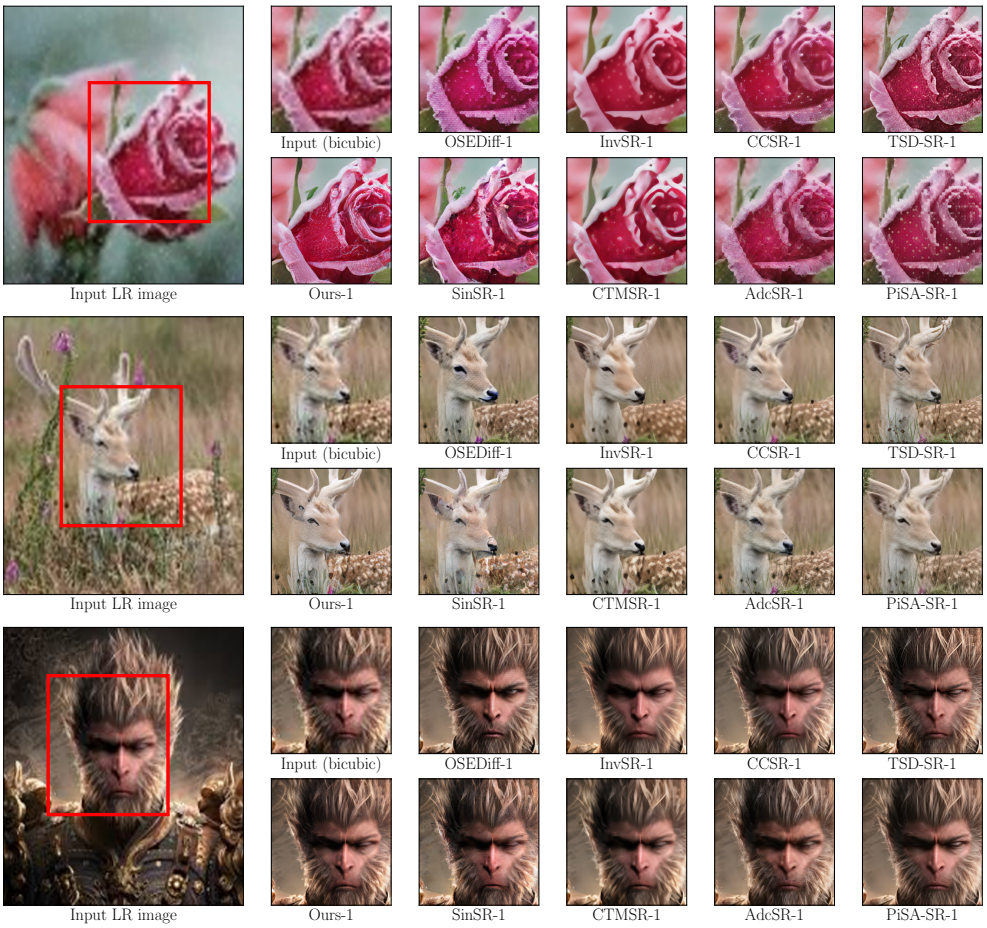

Figure 6: Visual results of recent one-step diffusion SR models (RSD, SinSR, CTMSR, OSEDiff, AdcSR, CCSR, InvSR, PiSA-SR, TSD-SR) on full-size images from RealLQ250 (Ai et al., 2024). Please zoom in for a better view.

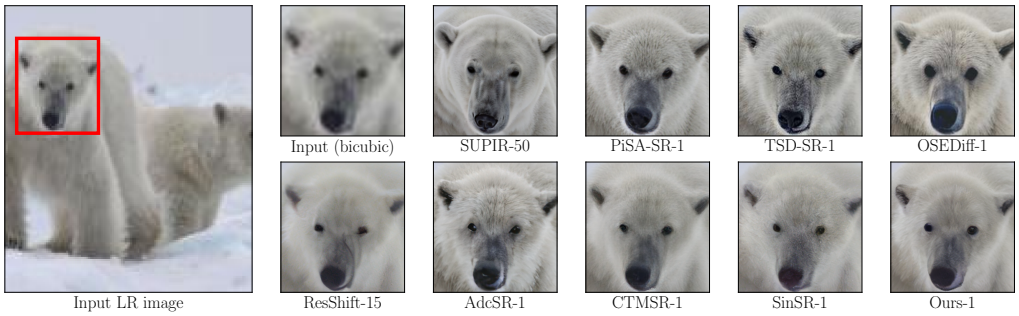

Figure 7: Additional comparison on RealSet65 (Yue et al., 2023) for diffusion SR models. Bottom images: ResShift, AdcSR, CTMSR, SinSR, and the proposed RSD. Top images: bicubic LR, SUPIR, PiSA-SR, TSD-SR, and OSEDiff. Please zoom in $\times 5$ times for a better view.

F ADDITIONAL ABLATION STUDIES

Ablation on the hyperparameter K. To assess the sensitivity of RSD to the hyperparameter K in Algorithm 1, the number of fake ResShift updates per student update, we performed experiments with the final RSD configuration, which is reported in Tables 1 and 2, with additional supervised losses for $K \in \{1, 3, 5, 10\}$. We evaluated the trained models on both the full-size RealSR dataset (Cai et al., 2019) (Table 18, as in Section 4.3) and the ImageNet-Test dataset (Yue et al., 2023) (Table 19, following Table 14). For both datasets all choices of K yield very similar performance: $K = 1$ slightly improves or matches the metrics of $K = 5$ while roughly halving the training time due to fewer fake-model updates. These results indicate that, in the presence of additional ground-truth losses, RSD is largely insensitive to the exact choice of K in this range, so K can be used to optimize computation at the cost of only minor performance changes. We used $K = 5$ to follow the DMD2 strategy for the number of updates of the fake model per student update (Yin et al., 2024a); see Figure 9 in Appendix C of DMD2 for the analysis of the impact of K on the training stability for image generation problems. Our results show that RSD training with $K = 1$ and supervised losses can also be beneficial for Real-ISR problems while not breaking the good performance of $K = 5$.

To isolate the effect of K on optimization stability, we further repeated the ablation in a *distill only* setup ((**Ours**, distill only) in Tables 1 and 14) without supervised losses. Figure 8 shows the convergence of PSNR and CLIPIQA on the ImageNet-Test dataset for $K \in \{1, 3, 5, 10\}$ in this case. For $K = 1$, the training dynamics become highly unstable, with large oscillations and clearly degraded final metrics, whereas configurations with $K \geq 3$ converge smoothly to similar quality levels. This suggests that supervised losses play a stabilizing role when using small K, and that $K = 5$ remains a robust choice in more challenging or purely distillation-based settings, while $K = 1$ is a viable and more efficient alternative in the supervised Real-ISR configuration used in the main experiments. This behavior was also reported in Figure 9 of DMD2.

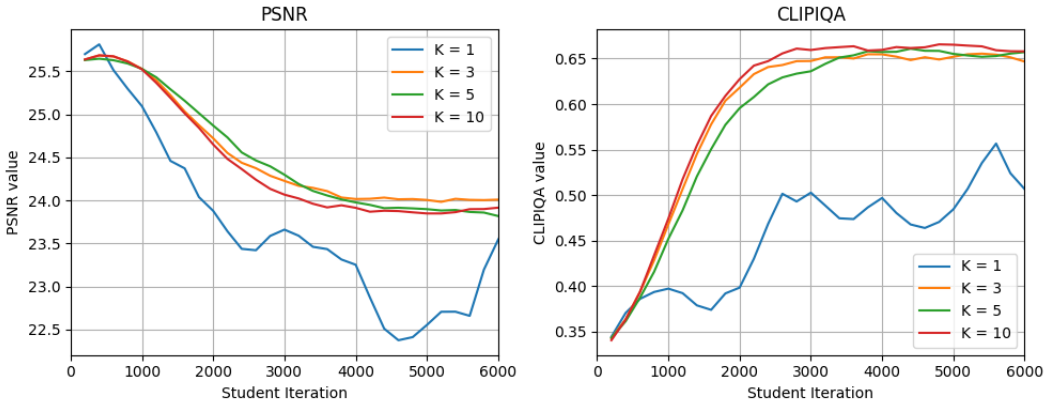

Figure 8: Convergence of PSNR and CLIPIQA on the ImageNet-Test dataset for $K \in \{1, 3, 5, 10\}$ when training *distill only* RSD. For $K = 1$, the optimization becomes unstable and fails to reach the quality of configurations with $K \geq 3$.

Table 18: Ablation on the hyperparameter K on the RealSR validation set. All runs use the final RSD configuration with supervised losses.

K	PSNR↑	SSIM↑	LPIPS↓	CLIPIQA↑	MUSIQ↑
1	25.99	0.756	0.2713	0.7159	66.247
3	25.86	0.752	0.2701	0.7093	66.140
5	25.91	0.754	0.2726	0.7060	65.860
10	26.27	0.749	0.2732	0.7135	65.233

Table 19: Ablation on the hyperparameter K on the ImageNet-Test dataset. All runs use the final RSD configuration with supervised losses.

K	PSNR↑	SSIM↑	LPIPS↓	CLIPIQA↑	MUSIQ↑
1	24.28	0.657	0.196	0.697	59.499
3	24.11	0.644	0.191	0.675	59.535
5	24.31	0.657	0.193	0.681	58.947
10	24.01	0.639	0.193	0.671	59.110

Ablation on supervised losses. We support the quantitative results of Table 5 on the RealSR dataset (Cai et al., 2019) with visual results in Figure 9. Without any supervised losses, RSD produces images with excessively sharp features, which are not related to the reference image; see the bottom image of Figure 9. As shown in Table 5, the LPIPS loss improves the correspondence to the reference image in terms of reference-based metrics (PSNR and LPIPS), but also spoils no-reference metrics (CLIPIQA and MUSIQ). This is visualized as smoother skin in the top image of Figure 9. Incorporating the GAN loss leads to the opposite effect and increases the number of details, such as skin textures. Adding both LPIPS and GAN losses allows us to balance between the number of excessive details and blurriness. For example, in the top image of Figure 9, both supervised losses improve the realism of the female eye.

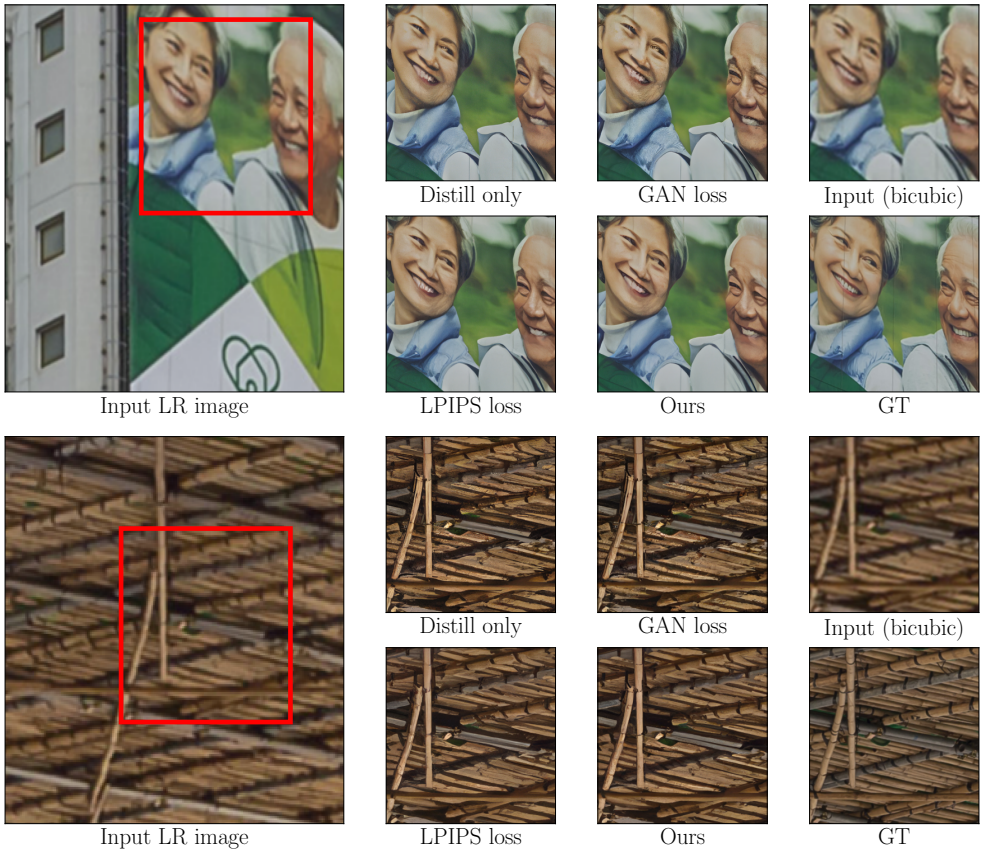

Figure 9: Effect of incorporating supervised losses on RealSR (Cai et al., 2019). Please zoom in for a better view.

G RESULTS OF RSD TRAINED ON BIGGER RESOLUTION

To compare the performance of the RSD, SinSR, and ResShift models for training on high resolution images, we followed the training setup of OSEDiff, which was trained on 512×512 HR images randomly cropped from LSDIR (Li et al., 2023) with LR images generated via the Real-ESRGAN degradations with the $\times 4$ SR factor. Since the original ResShift model was trained only on 256×256 HR images, we first trained the ResShift model on 512×512 HR random crops from LSDIR (Li et al., 2023) for 300k iterations using the source training ResShift code and then distilled it with the RSD and SinSR methods. For a fair comparison, we used the same hyperparameters for RSD and SinSR, which were used for their training on 256×256 HR images in Table 1, Table 14, Table 2.

We evaluated trained ResShift, SinSR and RSD models on full-size images from RealSR (Cai et al., 2019) (left part of Table 1) and provided quantitative results in Table 20, where we also provide results of Real-ESRGAN, BSRGAN, SUPIR and OSEDiff from Table 15. We provide visual results of those models in Figure 10.

Comparison with SinSR. We observe that the RSD achieves better perceptual results, especially in CLIPIQA and MUSIQ, with competitive PSNR and SSIM compared to SinSR. Although ResShift and SinSR have better fidelity metrics, the gap between the visual quality of these models compared with the RSD can be observed in image details, which are sharper for RSD (compare the jackets in the top of Figure 10, and trees in the middle of Figure 10).

Comparison with OSEDiff. Compared to OSEDiff, RSD trained on the same images from the LSDIR dataset (Li et al., 2023) using HR crops of the same resolution 512×512 achieves better reference metrics (PSNR, SSIM, LPIPS), but worse no-reference metrics (CLIPIQA, MUSIQ). This is evident in Figure 10, where both OSEDiff and SUPIR models provide not relevant to the LR image details (see non-existing inscriptions in the bottom of Figure 10). We highlight that since we did not finetune hyperparameters of the teacher ResShift model, the quality of RSD is limited by the quality of the ResShift model. The main goal of this study is to show that **RSD achieves better perceptual results compared with SinSR even if trained on images with higher resolutions**. Improving the perceptual image quality of the RSD when trained on images of higher resolutions to make it closer to the visual quality of T2I-based SR models is a promising future work.

The performance of the RSD model closely mirrors that of its teacher model. Notably, the RSD model trained at a resolution of 256×256 demonstrates better performance on no-reference image quality metrics, such as CLIPIQA and MUSIQ (see Table 1). In contrast, the RSD model trained at 512×512 resolution achieves better results on reference-based metrics, including PSNR, SSIM, and LPIPS (see Table 20). We hypothesize that the observed decline in no-reference metrics, alongside the improvement in reference-based metrics at higher resolutions, is primarily attributed to the behavior of the teacher model, ResShift. Specifically, the ResShift model trained on 256×256 images yields higher scores on no-reference perceptual quality metrics, whereas the model trained on 512×512 images performs better on reference-based metrics. The RSD model exhibits the same pattern, which explains the observed trade-off between the two types of evaluation metrics across resolutions.

Table 20: Results on full-size images from RealSR (Cai et al., 2019). ResShift, SinSR and RSD were trained on 512×512 HR random crops from LSDIR (Li et al., 2023). The best and second best results are highlighted in **bold** and underline.

Methods	NFE	PSNR↑	SSIM↑	LPIPS↓	CLIPIQA↑	MUSIQ↑
Real-ESRGAN (Wang et al., 2021)	1	25.85	0.773	0.273	0.4898	59.678
BSRGAN (Zhang et al., 2021)	1	26.51	0.775	0.269	0.5439	63.586
SUPIR (Yu et al., 2024)	50	24.38	0.698	0.331	0.5449	63.679
OSEDiff (Wu et al., 2024a)	1	25.25	0.737	0.299	**0.6772**	**67.602**
ResShift (Yue et al., 2023)	15	**27.53**	**0.790**	0.277	0.4988	58.034
SinSR (Wang et al., 2024b)	1	<u>27.27</u>	<u>0.780</u>	<u>0.268</u>	0.5503	59.478
RSD (**Ours**)	1	26.89	0.773	**0.260**	<u>0.6103</u>	<u>64.987</u>

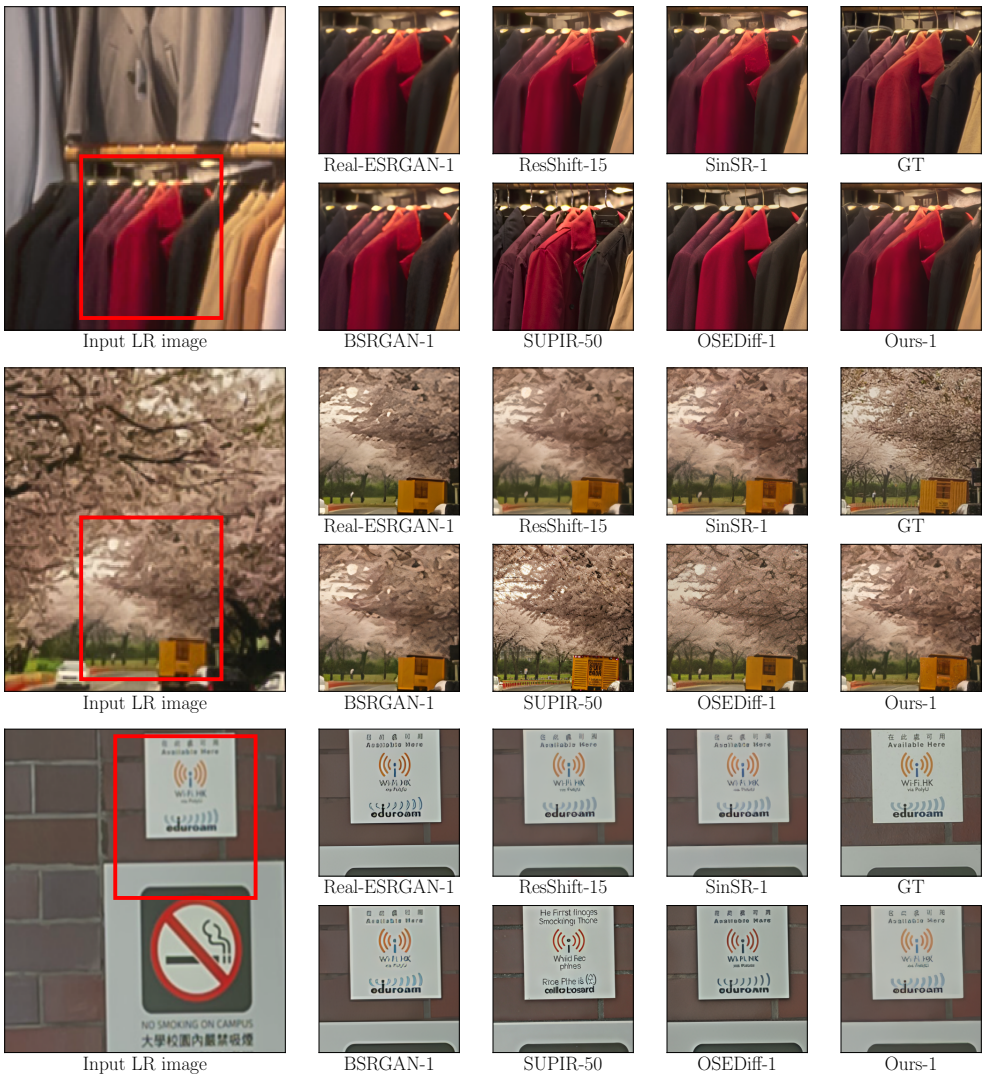

Figure 10: Visual results of RSD, ResShift, and SinSR models trained on 512×512 HR images from LSDIR dataset (Li et al., 2023) and other baselines (Real-ESRGAN, BSRGAN, SUPIR, OSEDiff) on full-size images from RealSR (Yue et al., 2023). Please zoom in for a better view.

H COMPARISON WITH ADDSR

It may be seem that our primary distillation loss $\mathcal{L}_\theta$ (7) is similar to the SDS loss adopted in ADD (Sauer et al., 2025) $\mathcal{L}_{distill}$ and AddSR (Xie et al., 2024) (Appendix A, (Sauer et al., 2025) and $\mathcal{L}_{ta-dis}$, Equation 1, (Xie et al., 2024)). However, we show that this similarity is only on the surface.

Conceptual difference in objective functions. In our work, we propose the RSD loss (22), and it is fundamentally different from SDS in both its formulation and practical implications. RSD introduces an auxiliary model to more accurately estimate the score function of the model distribution. This allows for a tighter and lower-variance approximation of the true KL gradient. Moreover, instead of treating each timestep independently as in SDS and VSD (i.e., using marginal KL divergences over x_t), our RSD loss is formulated over **the entire trajectory** $x_{0:T}$, leading to a more holistic distillation of the teacher's reverse process.

To facilitate a clear comparison, we summarize the key differences between the loss objectives used in SDS and our proposed RSD in Table 21. We denote by p^* the reverse process of the teacher ResShift model and by p the reverse process of ResShift trained on generator data.

Table 21: Comparison of distillation objectives between SDS (Poole et al., 2023), ADD (Sauer et al., 2025), AddSR (Xie et al., 2024) and RSD

Methods	Objective Function
SDS (Poole et al., 2023), ADD (Xie et al., 2024), AddSR (Xie et al., 2024)	$\mathbb{E}_{p(y_0)}\left[\sum_{t=1}^{T} w_t \mathcal{D}_{\mathrm{KL}}\Big(p(x_t\|y_0)\|p^*(x_t\|y_0)\Big)\right]$
RSD (**Ours**, distill-only)	$\mathbb{E}_{p(y_0)}\left[\mathcal{D}_{\mathrm{KL}}\Big(p(x_{0:T}\|y_0)\,\|\,p^*(x_{0:T}\|y_0)\Big)\right]$

Practical difference. In addition to theoretical differences between RSD and ADD objectives discussed above, we list practical differences between implementations of RSD and AddSR for real-world SR.

1. Objective implementation. The implementation of objective in Eq. 1 in AddSR (Xie et al., 2024) is different from RSD objective in Eq. (11) in many aspects:

1. **RSD does not have any hyperparameters in the distillation loss**. The distillation loss of AddSR, $\mathcal{L}_{ta-dis}$ (Equation 1, (Xie et al., 2024)), requires a weighting function $d(s,t)$ (Equation 3, (Xie et al., 2024)), which is defined by two hyperparameters, μ and ν. The choice μ and ν is based solely on empirical analysis of performance results, as shown in Table 7 and Table 8 of AddSR. In contrast, RSD loss in Eq. (8) relies only on weights w_t, which are used for the training of the ResShift model (Eq. 8 in (Yue et al., 2023)). These weights are derived from the theory of DDPM (Ho et al., 2020) and in practice are omitted by ResShift and RSD following the conclusion of DDPM (see Appendix I).
2. **Different supervised losses**. The adversarial loss of AddSR, $\mathcal{L}_{ta-dis}$, follows the hinge loss used in ADD (Sauer et al., 2025). We follow the adversarial loss of DMD2 (Yin et al., 2024a) and use the standard non-saturating loss. We also use LPIPS loss following OSEDiff (Wu et al., 2024a), while AddSR omits it.
3. **Fake model**. Contrary to AddSR, the objective of RSD involves a trainable fake model.

Architecture. The major architectural differences are as follows:

1. **RSD does not have any networks related to text-to-image models**. The architecture of generator and fake model in RSD is a UNet model (Ronneberger et al., 2015) following ResShift. We avoid ControlNet (Zhang et al., 2023) and other models used in AddSR.
2. **The sizes of the AddSR and RSD architectures differ by 1 order of magnitude**. In total, the architecture of AddSR requires 2.28B parameters, while RSD requires 174M parameters.

Empirical results. We show the comparison between results of 1-step AddSR and RSD in Table 22. It shows that RSD outperforms AddSR in most fidelity and perceptual metrics while having $\times 10$ much fewer parameters.

Table 22: Quantitative results of AddSR and RSD models on crops 512×512 from StableSR (Wang et al., 2024a). The best results are highlighted in **bold**.

Datasets	Methods	PSNR↑	SSIM↑	LPIPS↓	DISTS↓	NIQE↓	MUSIQ↑	MANIQA↑	CLIPIQA↑
DIV2K-Val	AddSR (Xie et al., 2024)	23.26	0.5902	0.3623	0.2123	**4.7610**	63.39	0.5657	0.5734
	RSD (**Ours**)	**23.91**	**0.6042**	**0.2857**	**0.1940**	5.1987	**68.05**	**0.5937**	**0.6967**
DrealSR	AddSR (Xie et al., 2024)	**27.77**	**0.7722**	0.3196	**0.2242**	6.9321	60.85	0.5490	0.6188
	RSD (**Ours**)	27.40	0.7559	**0.3042**	0.2343	**6.2577**	**62.03**	**0.5625**	**0.7019**
RealSR	AddSR (Xie et al., 2024)	24.79	0.7077	0.3091	**0.2191**	**5.5440**	**66.18**	**0.6098**	0.5722
	RSD (**Ours**)	**25.61**	**0.7420**	**0.2675**	0.2205	5.7500	66.02	0.5930	**0.6793**

I Details of ResShift

As a part of the diffusion model class, ResShift can be described by specifying the forward (degradation) process, the parametrization of the reverse (restoration) process, and the objective for training the reverse process.

Forward process. Consider a pair of (LR, HR) images $(y_0, x_0) \sim p_{\text{data}}(y_0, x_0)$. For a residual $e_0 = y_0 - x_0$, ResShift proposes to transit from x_0 to y_0 with the Markov chain $\{x_t\}_{t=1}^T$ of length T through the following Gaussian transition distribution:

$$q(x_t|x_{t-1}, y_0) = \mathcal{N}(x_t|x_{t-1} + \alpha_t e_0, \kappa^2 \alpha_t \mathbf{I}), \tag{37}$$

where:

- $\alpha_t = \eta_t - \eta_{t-1}$ for $t > 1$ and $\alpha_1 = \eta_1$ are defined by the shifting sequence $\{\eta_t\}_{t=1}^T$, $\mathbf{I}$ denotes the identity matrix.
- κ is a hyper-parameter controlling the noise variance and the shifting sequence $\{\eta_t\}_{t=1}^T$ monotonically increases with the timestep t.

The transition distribution (1) leads to analytically tractable marginal distribution of $q(x_t|x_0, y_0)$ at any timestep t:

$$q(x_t|x_0, y_0) = \mathcal{N}(x_t|x_0 + \eta_t e_0, \kappa^2 \eta_t \mathbf{I}), t \in [1, T], \tag{38}$$

The shifting sequence satisfies $\eta_1 \approx 0$ and $\eta_T \approx 1$, which guarantee the convergence of marginal distributions of x_1 and x_T to approximate distributions of the HR image and the LR image respectively. Notably, the posterior distribution $q(x_{t-1}|x_t, x_0, y_0)$ for the transition distribution (1) is tractable and can be derived using the Bayes's rule:

$$q(x_{t-1}|x_t, x_0, y_0) = \mathcal{N}\left(x_{t-1} \middle| \frac{\eta_{t-1}}{\eta_t} x_t + \frac{\alpha_t}{\eta_t} x_0, \kappa^2 \frac{\eta_{t-1}}{\eta_t} \alpha_t \mathbf{I}\right). \tag{39}$$

Reverse process. ResShift suggests the construction of the reverse process to estimate the posterior distribution $p(x_0|y_0)$ in the following parametrized form:

$$p_\theta(x_0|y_0) = \int p(x_T|y_0) \prod_{t=1}^T p_\theta(x_{t-1}|x_t, y_0) dx_{1:T} \tag{40}$$

Here $p(x_T|y_0) \approx \mathcal{N}(x_T|y_0, \kappa^2 I)$ and $p_\theta(x_{t-1}|x_t, y_0)$ is the inverse transition kernel from x_{t-1} to x_t with learnable parameters θ. Following DDPM (Ho et al., 2020), ResShift parametrizes this transition kernel with the Gaussian:

$$p_\theta(x_{t-1}|x_t, y_0) = \mathcal{N}(x_{t-1}|\mu_\theta(x_t, y_0, t), \Sigma_\theta(x_t, y_0, t)) \tag{41}$$

Objective. To derive the minimization objective for parameters θ, ResShift applies the variational bound estimation on negative log-likelihood for the $p_\theta(x_0|y_0)$, as in DDPM:

$$\min_\theta \mathbb{E}_{(x_0, y_0)} \sum_{t=1}^T \mathbb{E}_{x_t \sim q(x_t|x_0, y_0)} \left[\mathcal{D}_{KL}(q(x_{t-1}|x_t, x_0, y_0)||p_\theta(x_{t-1}|x_t, y_0))\right] \tag{42}$$

Inspired by the tractable formula for the posterior $q(x_{t-1}|x_t, x_0, y_0)$ in (39), ResShift sets the variance parameter $\Sigma_\theta(x_t, y_0, t)$ to be independent of x_t and y_0 and reparametrized the parameter $\mu_\theta(x_t, y_0, t)$ as follows:

$$\Sigma_\theta(x_t, y_0, t) = \kappa^2 \frac{\eta_{t-1}}{\eta_t} \alpha_t \mathbf{I} \tag{43}$$

$$\mu_\theta(x_t, y_0, t) = \frac{\eta_{t-1}}{\eta_t} x_t + \frac{\alpha_t}{\eta_t} f_\theta(x_t, y_0, t), \tag{44}$$

where f_θ is a deep neural network with parameter θ, aiming to predict x_0. Given the Gaussian form of the distributions $q(x_{t-1}|x_t, x_0, y_0)$ (39) and $p_\theta(x_{t-1}|x_t, y_0)$ (41), the objective (42) simplifies as follows:

$$\min_\theta \left[\sum_{t=1}^{T} w_t \mathbb{E}_{(x_0, y_0, x_t)} \| f_\theta(x_t, y_0, t) - x_0 \|^2 \right], \tag{45}$$

where $w_t = \frac{\alpha_t}{2\kappa^2 \eta_t \eta_{t-1}}$. Empirically, the omitting the weight w_t leads to a noticeable improvement in performance, which aligns with the conclusion in DDPM.

J LIMITATIONS AND FAILURE CASES

We present failure cases for image restoration for RSD and baselines. Our method may produce images with errors, since the teacher model is imperfect. However, we stress that T2I-based SR models with rich priors also have such problems. Specifically, in Figure 11 (top), we observe that the teacher model produces an indistinguishable image from the simple bicubic upsampling image. A similar result occurs with OSEDiff, while all other methods, including ours, SinSR, SUPIR, and GAN-based models, produce images with visible artifacts. The other typical failure case of diffusion-based methods with T2I prior, such as ResShift, SinSR, and RSD, includes images with rich background details, which are hard to predict given insufficient contextual information on the LR image. As we show in Figure 11 (bottom), hallucination properties of T2I-based methods, SUPIR and OSEDiff, provide a realistic continuation of the road and cars with greater and richer details compared to results of ResShift, SinSR, and RSD. In Figure 12, we show failure cases of the considered SR methods on the real-world RealSR benchmark (Cai et al., 2019) with available ground truth images. All methods struggle when running on images with many small details, such as computer details and bush patterns. The hallucinations of diffusion-based methods do not coincide with the original HR image in small detail. Figure 13 demonstrates several failure cases for real-world SR methods on synthetic low-resolution crops of StableSR (Wang et al., 2024a), which were obtained from DIV2K dataset (Agustsson & Timofte, 2017) using Real-ESRGAN degradations (Wang et al., 2021). Due to the lack of context diffusion-based methods, ResShift, SinSR, and RSD failed to reconstruct details of the squirrel's body and forest, as well as T2I-based SUPIR and OSEDiff methods with richer prior. Their predictions have significant visual differences with ground truth HR images.

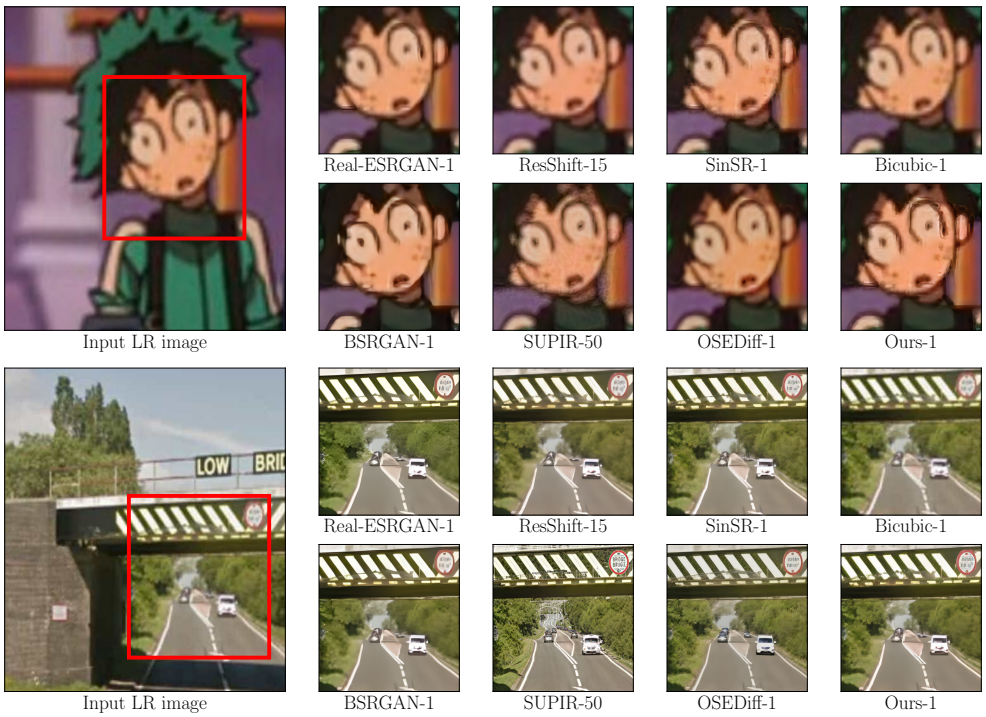

Figure 11: Failure cases on images from RealSet65 (Yue et al., 2023). Please zoom in for a better view.

Figure 12: Failure cases on images from RealSR (Yue et al., 2023). Please zoom in for a better view.

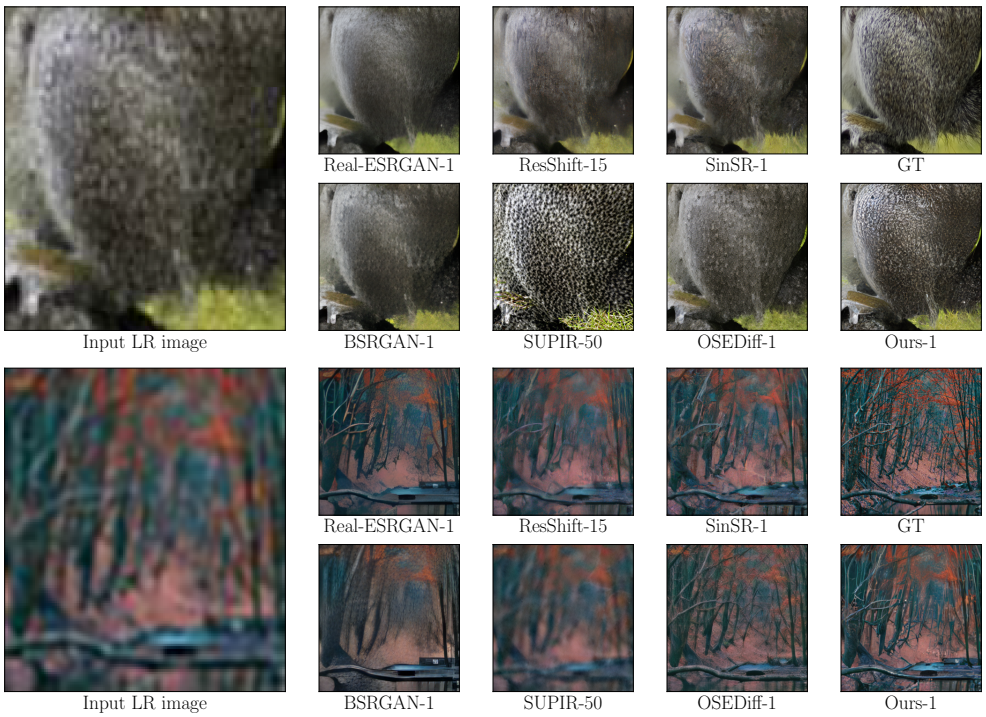

Figure 13: Failure cases on synthetic images from DIV2K crops (Agustsson & Timofte, 2017; Wang et al., 2024a). Please zoom in for a better view.

K PROOFS

Proof of Proposition 3.1. **First stage.** We first prove that using objective $\mathcal{L}_{\text{fake}}$ (see Eq. (8)) is equivalent to training a fake model f_ϕ with objective (5). We recall the $\mathcal{L}_{\text{fake}}$ minimization objective:

$$\arg\min_{\phi} \mathcal{L}_{\text{fake}}, \tag{46}$$

where

$$\mathcal{L}_{\text{fake}} = \Big(\sum_{t=1}^{T} w_t \mathbb{E}_{p_\theta(\widehat{x}_0, y_0, x_t)} \Big\{ \|f_\phi(x_t, y_0, t)\|_2^2 - 2\langle f_\phi(x_t, y_0, t) + \underbrace{f^*(x_t, y_0, t)}_{\text{Does not depend on } \phi}, \widehat{x}_0 \rangle \Big\} \Big) \tag{47}$$

Then we prove:

$$\arg\min_{\phi} \underbrace{\Big(\sum_{t=1}^{T} w_t \mathbb{E}_{p_\theta(\widehat{x}_0, y_0, x_t)} \|f_\phi(x_t, y_0, t) - \widehat{x}_0\|_2^2 \Big)}_{\text{Training a fake model } f_\phi \text{ with objective (5)}} =$$

$$\arg\min_{\phi} \Big(\sum_{t=1}^{T} w_t \mathbb{E}_{p_\theta(\widehat{x}_0, y_0, x_t)} \Big\{ \|f_\phi(x_t, y_0, t)\|_2^2 - 2\langle f_\phi(x_t, y_0, t), \widehat{x}_0 \rangle \Big\} + \underbrace{\sum_{t=1}^{T} w_t \mathbb{E}_{p_\theta(\widehat{x}_0, y_0, x_t)} \|\widehat{x}_0\|_2^2}_{\text{Does not depend on } \phi} \Big) =$$

$$\arg\min_{\phi} \Big(\sum_{t=1}^{T} w_t \mathbb{E}_{p_\theta(\widehat{x}_0, y_0, x_t)} \Big\{ \|f_\phi(x_t, y_0, t)\|_2^2 - 2\langle f_\phi(x_t, y_0, t), \widehat{x}_0 \rangle \Big\} \Big) =$$

$$\arg\min_{\phi} \Big(\sum_{t=1}^{T} w_t \mathbb{E}_{p_\theta(\widehat{x}_0, y_0, x_t)} \Big\{ \|f_\phi(x_t, y_0, t)\|_2^2 - 2\langle f_\phi(x_t, y_0, t), \widehat{x}_0 \rangle \Big\} - \underbrace{\sum_{t=1}^{T} w_t \mathbb{E}_{p_\theta(\widehat{x}_0, y_0, x_t)} \Big\{ 2\langle f^*(x_t, y_0, t), x_0 \rangle \Big\}}_{\text{Does not depend on } \phi} \Big) =$$

$$\arg\min_{\phi} \Big(\sum_{t=1}^{T} w_t \mathbb{E}_{p_\theta(\widehat{x}_0, y_0, x_t)} \Big\{ \|f_\phi(x_t, y_0, t)\|_2^2 - 2\langle f_\phi(x_t, y_0, t) + \underbrace{f^*(x_t, y_0, t)}_{\text{Does not depend on } \phi}, \widehat{x}_0 \rangle \Big\} \Big) =$$

$$\arg\min_{\phi} \mathcal{L}_{\text{fake}}. \tag{48}$$

Second stage. Now we prove that:

$$\underbrace{\sum_{t=1}^{T} w_t \mathbb{E}_{p_\theta(\widehat{x}_0, y_0, x_t)} \|f_{G_\theta}(x_t, y_0, t) - f^*(x_t, y_0, t)\|_2^2}_{\mathcal{L}_\theta} =$$

$$-\min_{\phi} \Big\{ \sum_{t=1}^{T} w_t \mathbb{E}_{p_\theta(\widehat{x}_0, y_0, x_t)} \Big(\|f_\phi(x_t, y_0, t)\|_2^2 - \|f^*(x_t, y_0, t)\|_2^2 + 2\langle f^*(x_t, y_0, t) - f_\phi(x_t, y_0, t), \widehat{x}_0 \rangle \Big) \Big\} \tag{49}$$

Note, that since ResShift objective (45) is an MSE, the solution f_{G_θ} for the data produced by generator G_θ is given by the conditional expectation as:

$$f_{G_\theta}(x_t, y_0, t) = \mathbb{E}_{p_\theta(\widehat{x}_0 | y_0, x_t)}[\widehat{x}_0]. \tag{50}$$

We start from the right part of (49) and transform it back to the left part:

$$
\begin{aligned}
&-\min_{\phi}\Big\{\sum_{t=1}^{T} w_t \mathbb{E}_{p_\theta(\widehat{x}_0,y_0,x_t)}\Big(-\|f^*(x_t,y_0,t)\|_2^2+\|f_\phi(x_t,y_0,t)\|_2^2+\\
&\qquad 2\langle f^*(x_t,y_0,t)-f_\phi(x_t,y_0,t),\widehat{x}_0\rangle\Big)\Big\}=\\
&\sum_{t=1}^{T} w_t \mathbb{E}_{p_\theta(\widehat{x}_0,y_0,x_t)}\Big\{\|f^*(x_t,y_0,t)\|_2^2-2\langle f^*(x_t,y_0,t),\widehat{x}_0\rangle\Big\}-\\
&\min_{\phi}\Big\{\sum_{t=1}^{T} w_t \mathbb{E}_{p_\theta(\widehat{x}_0,y_0,x_t)}\Big(\|f_\phi(x_t,y_0,t)\|_2^2-2\langle f_\phi(x_t,y_0,t),\widehat{x}_0\rangle\Big)\Big\}=\\
&\sum_{t=1}^{T} w_t \mathbb{E}_{p_\theta(y_0,x_t)}\Big(\|f^*(x_t,y_0,t)\|_2^2-2\langle f^*(x_t,y_0,t),\underbrace{\mathbb{E}_{p_\theta(\widehat{x}_0|y_0,x_t)}\widehat{x}_0}_{f_{G_\theta}(x_t,y_0,t)}\rangle\Big)-\\
&\min_{\phi}\Big\{\sum_{t=1}^{T} w_t \mathbb{E}_{p_\theta(\widehat{x}_0,y_0,x_t)}\Big(\|f_\phi(x_t,y_0,t)\|_2^2-2\langle f_\phi(x_t,y_0,t),\widehat{x}_0\rangle\Big)\Big\}=\\
&\sum_{t=1}^{T} w_t \mathbb{E}_{p_\theta(y_0,x_t)}\Big(\|f^*(x_t,y_0,t)\|_2^2-2\langle f^*(x_t,y_0,t),f_{G_\theta(x_t,y_0,t)}\rangle\Big)-\\
&\sum_{t=1}^{T} w_t \mathbb{E}_{p_\theta(y_0,x_t)}\Big(\|f_{G_\theta}(x_t,y_0,t)\|_2^2-2\underbrace{\langle f_{G_\theta}(x_t,y_0,t),f_{G_\theta(x_t,y_0,t)}\rangle}_{\|f_{G_\theta}\|_2^2}\Big)=\\
&\sum_{t=1}^{T} w_t \mathbb{E}_{p_\theta(y_0,x_t)}\Big(\|f^*(x_t,y_0,t)\|_2^2-2\langle f^*(x_t,y_0,t),f_{G_\theta(x_t,y_0,t)}\rangle+\|f_{G_\theta}(x_t,y_0,t)\|_2^2\Big)=\\
&\qquad\sum_{t=1}^{T} w_t \mathbb{E}_{p_\theta(y_0,x_t)}\underbrace{\|f_{G_\theta}(x_t,y_0,t)-f^*(x_t,y_0,t)\|_2^2}_{\text{Does not depend on }\widehat{x}_0\text{ so we can add }\widehat{x}_0\text{ in expectation.}}=\\
&\qquad\qquad\sum_{t=1}^{T} w_t \mathbb{E}_{p_\theta(\widehat{x}_0,y_0,x_t)}\|f_{G_\theta}(x_t,y_0,t)-f^*(x_t,y_0,t)\|_2^2.
\end{aligned}
$$

□

Discussion. We explain the intractability of the gradient for $\mathcal{L}_\theta$ in Equation (7) as follows. The gradient of $\mathcal{L}_\theta$ (7) over parameters θ of G_θ is given by the chain rule:

$$
\frac{d\mathcal{L}_\theta}{d\theta}=\underbrace{\frac{\partial\mathcal{L}}{\partial\theta}}_{\text{direct}}+\frac{\partial\mathcal{L}}{\partial f_{G_\theta}}\cdot\underbrace{\frac{\partial f_{G_\theta}}{\partial\theta}}_{\text{implicit}} \tag{51}
$$

$\frac{d\mathcal{L}_\theta}{d\theta}$ contains an implicit term, which requires a differentiation through the full ResShift training loop and is computationally infeasible (because one needs to backpropagate through all the gradient updates used to train f_{G_θ}):

$$
\frac{\partial f_{G_\theta}}{\partial\theta}=\frac{\partial}{\partial\theta}\underbrace{\Big[\arg\min_{\phi}[\mathcal{L}(\phi,\theta)]\Big]}_{\text{Training on the Generator outputs}} \tag{52}
$$

In contrast, our Proposition 3.1 and Equation (8) resolve this by deriving the mathematically equivalent form of Equation (7), which does not require directly differentiating through the "re-training" step f_{G_θ} i.e., it does not contain terms with argmin operations.

L MORE VISUAL RESULTS

This section provides an additional qualitative visual comparisons between RSD and other baselines on two real-world full-size and two synthetic benchmarks with available ground truth data.

1. Full-size benchmark RealSR (Cai et al., 2019). The results are shown in Figure 14.
2. Full-size benchmark DRealSR (Wei et al., 2020). The results are shown in Figure 15.
3. Synthetic benchmark ImageNet-Test (Deng et al., 2009; Yue et al., 2023). The results are shown in Figure 16.
4. Synthetic benchmark DIV2K (Agustsson & Timofte, 2017; Wang et al., 2024a). The results are shown in Figure 17.

The baseline methods include multistep diffusion-based SR methods (ResShift (Yue et al., 2023), SUPIR (Yu et al., 2024)), 1-step diffusion-based SR methods (SinSR (Wang et al., 2024b), OSEDiff (Wu et al., 2024a)), and GAN-based SR methods (Real-ESRGAN (Wang et al., 2021) and BSRGAN (Zhang et al., 2021)).

Figure 14: Visual comparison on real-world samples from RealSR (Cai et al., 2019). Please zoom in for a better view.

M STATEMENT ON LLM USAGE AND IMPACT

The authors used the large language model (LLM) only to improve the writing and grammar of the text. All the results from the LLM were checked by the authors.

Our proposed distillation method of the diffusion-based image SR model, RSD, presents potential positive and negative societal impacts. On the positive side, the practical effect of the techniques developed to improve the quality and efficiency of the real-world SR model ranges from improving medical imaging for diagnostic purposes and assisting in disaster response to improving remote sensing and autonomous driving performance. However, there are concerns regarding the generation of fake content. Our model is generative and can generate deepfakes for disinformation. We note that

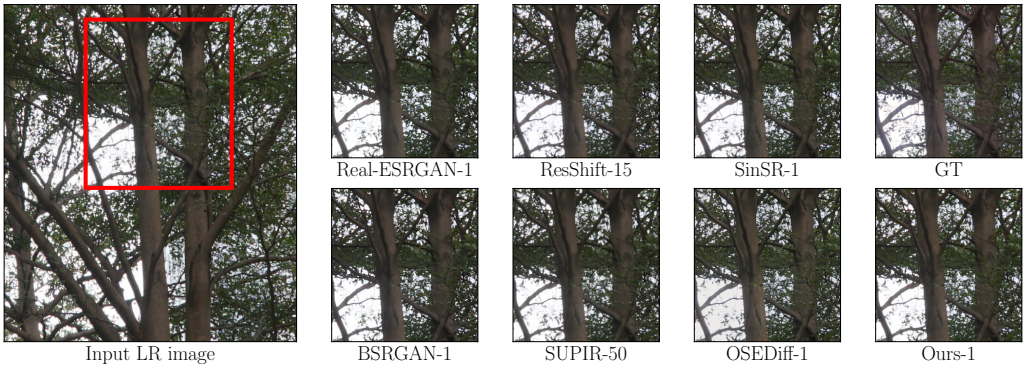

Figure 15: Visual comparison on real-world samples from DRealSR (Wei et al., 2020). Please zoom in for a better view.

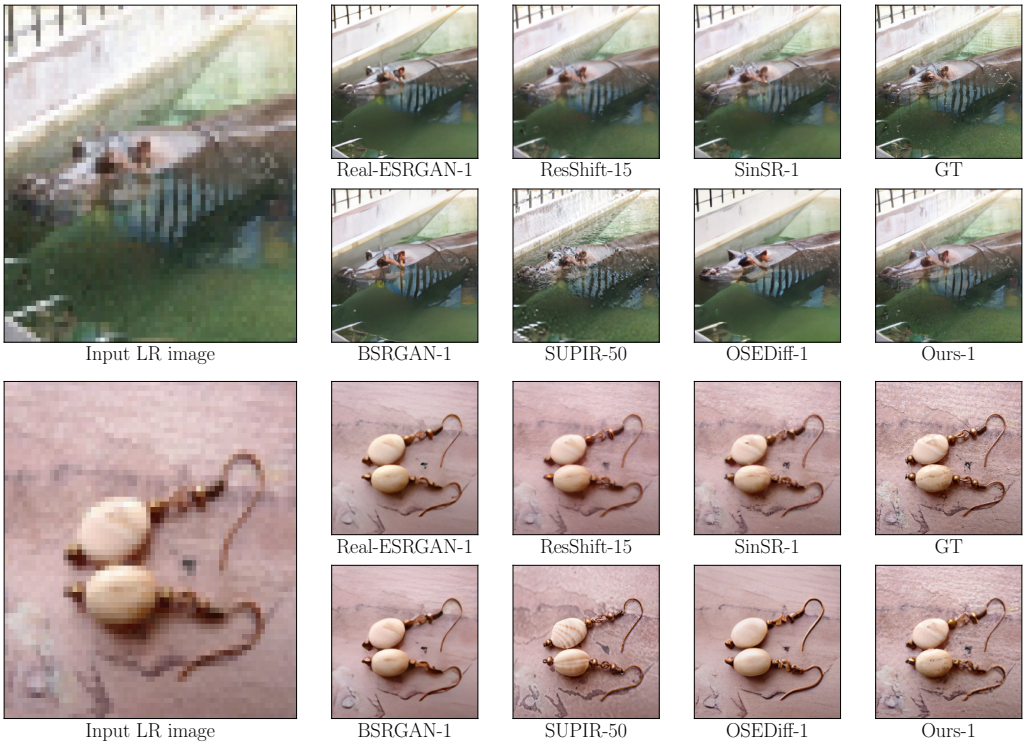

Figure 16: Visual comparison on synthetic samples from ImageNet-Test (Deng et al., 2009; Yue et al., 2023). Please zoom in for a better view.

our model was trained using only one dataset, ImageNet (Deng et al., 2009), which is known to be standard in diffusion SR research (Yue et al., 2023; Wang et al., 2024b; You et al., 2025; Gushchin et al., 2025). Thus, we do not expect any high risk of misuse of the trained model as long as the training data do not contain unsafe images.

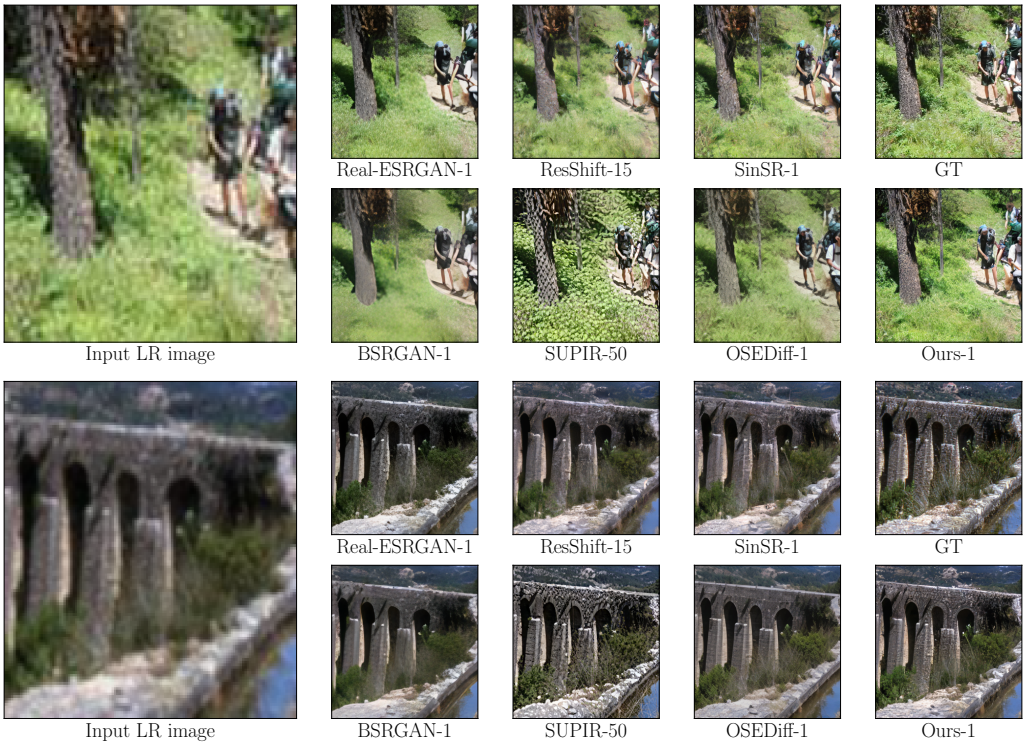

Figure 17: Visual comparison on synthetic samples from DIV2K crops (Agustsson & Timofte, 2017; Wang et al., 2024a). Please zoom in for a better view.